INVESTIGATION OF ELECTRONIC PROPERTIES OF DETECTOR GRADE CADMIUM ZINC TELLURIDE CRYSTALS AND DEVELOPMENT OF ELECTRODES FOR X-RAY AND GAMMA RAY APPLICATIONS

A THESIS SUBMITTED TO
THE GRADUATE SCHOOL OF NATURAL AND APPLIED SCIENCES
OF
MIDDLE EAST TECHNICAL UNIVERSITY

BY

DENİZ BENDER

IN PARTIAL FULFILLMENT OF THE REQUIREMENTS
FOR
THE DEGREE OF MASTER OF SCIENCE
IN
PHYSICS

JANUARY 2019

Approval of the thesis:

INVESTIGATION OF ELECTRONIC PROPERTIES OF DETECTOR GRADE CADMIUM ZINC TELLURIDE CRYSTALS AND DEVELOPMENT OF ELECTRODES FOR X-RAY AND GAMMA RAY APPLICATIONS

submitted by **DENİZ BENDER** in partial fulfillment of the requirements for the degree of **Master of Science in Physics Department, Middle East Technical University** by,

Prof. Dr. Halil Kalıpçılar
Dean, Graduate School of **Natural and Applied Sciences** _____

Prof. Dr. Altuğ Özpineci
Head of Department, **Physics** _____

Prof. Dr. Raşit Turan
Supervisor, **Physics, METU** _____

Prof. Dr. Mehmet Parlak
Co-Supervisor, **Physics, METU** _____

Examining Committee Members:

Prof. Dr. Hakan Altan
Physics Dept., METU _____

Prof. Dr. Raşit Turan
Physics Dept., METU _____

Prof. Dr. Nevzat Güneri Gençer
Electrical and Electronics Engineering Dept., METU _____

Prof. Dr. Emrah Kalemci
Fac. of Engineering and Natural Sciences, Sabancı University _____

Dr. İrfan Kuvvetli
Astrophysics Dept., Technical University of Denmark _____

Date: 11.01.2019

I hereby declare that all information in this document has been obtained and presented in accordance with academic rules and ethical conduct. I also declare that, as required by these rules and conduct, I have fully cited and referenced all material and results that are not original to this work.

Name, Surname: Deniz Bender

Signature:

ABSTRACT

INVESTIGATION OF ELECTRONIC PROPERTIES OF DETECTOR GRADE CADMIUM ZINC TELLURIDE CRYSTALS AND DEVELOPMENT OF ELECTRODES FOR X-RAY AND GAMMA RAY APPLICATIONS

Bender, Deniz
Master of Science, Physics
Supervisor: Prof. Dr. Raşit Turan
Co-Supervisor: Prof. Dr. Mehmet Parlak

January 2019, 99 pages

In the last three decades, we have witnessed extensive research activities on Cadmium Zinc Telluride (CdZnTe or CZT) crystals to be used as a part of radiation detector systems in different application areas including astrophysics, medical science and security devices. The accompanied developments such as increased ability to control the bulk growth of CZT crystals, advances in microelectronics and improvements in data-acquisition methods have all paved the way for flexible configurations of multiple pixel modules consisted of CZT detectors. Being a II-VI compound semiconductor, CZT appears to be suitable for room temperature operation with a high spectroscopic resolution. The intrinsic properties CZT crystal such as wide bandgap, high resistivity and high atomic number make it very useful in these applications. Although the resistivity of CdZnTe crystal is relatively high ($\rho > 10^8$ Ω cm), cracks formed during lapping/polishing processes or surface contamination make surface resistivity lower, leading to surface leakage current problems. To be able to use CZT crystals in X-ray and gamma-ray applications, leakage current should be minimized. In this thesis study, CZT detectors from different ingots produced at METU Crystal Growth Laboratory (GCL), including one with Indium doped and also from a commercial crystal, were produced and current-voltage (I-V) characterizations were completed with various electrode

designs. Main focus was to investigate the current-voltage behavior of metal-semiconductor interface formed on the detector crystals. In addition to I-V measurements, the crystal grown and prepared for detector application was characterized by different methods such as X-Ray Diffraction (XRD), Atomic Force Microscopy (AFM) and Scanning Electron Microscopy (SEM).

Keywords: Cadmium Zinc Telluride, X-ray Detectors, Gamma Ray Detectors, Current Voltage (IV) Measurements

ÖZ

DEDEKTÖR MERTEBESİNDEKİ KADMİYUM ÇİNKO TELLÜR KRİSTALLERİNİN ELEKTRONİK ÖZELLİKLERİNİN ARAŞTIRILMASI VE X-IŞINI İLE GAMMA IŞINI UYGULAMALARI İÇİN ELEKTROT GELİŞTİRİLMESİ

Bender, Deniz
Yüksek Lisans, Fizik
Tez Danışmanı: Prof. Dr. Raşit Turan
Ortak Tez Danışmanı: Prof. Dr. Mehmet Parlak

Ocak 2019, 99 sayfa

Son otuz yılda, sağlık, astrofizik ve güvenlik gibi alanlarda radyasyon dedektörü sistemlerinin bir parçası olarak kullanılmak üzere, Kadmiyum Çinko Tellür kristalleri konusunda yoğun ve artan bir araştırma etkinliğine tanık olundu. Bu çabalara eşlik eden gelişmelerin arasında Kadmiyum Çinko Tellür kristallerinin hacimsel büyütülmelerindeki yetkinliğin artması, mikro-elektronik uygulamalarındaki ilerlemeler ve veri toplama yöntemlerindeki gelişmeler sayılabilir ve tüm bunlar Kadmiyum Çinko Tellür kristallerinin çoklu piksel yapıları halinde dedektör olarak esnek bir şekilde yapılandırılmalarını mümkün kılmıştır. Kadmiyum Çinko Tellür kristallerinin esasen sahip olduğu yüksek bant aralığı, yüksek direnç, yüksek atom numarası ve hareket-yaşam süresi çarpımının da yüksek oluşu, II-VI grubu bileşiklerinden bir yarı iletken olan bu malzemeye oda sıcaklığında kullanılabilir olma özelliği ve yüksek çözünürlük vermektedir. Her ne kadar Kadmiyum Çinko Tellür kristallerinin direnci göreceli olarak yüksek olsa da ($\rho > 10^8$ Ω cm), düzleme ve parlatma işlemlerinde oluşan çatlaklar yüzey direncini düşürmektedir ve bu durum yüzeyde akım kaçağı sorununa yol açmaktadır. Bu kristallerin radyasyon dedektörü olarak kullanılabilmeleri için bu akım kaçaklarının azaltılması gerekir. Bu tez çalışmasında, ODTÜ Kristal Büyütme Laboratuvarında üretilmiş ve aralarında indiyum eklenmiş külçeler de olan büyütmelerden ve ticari

bir kristalden örnekler üretilmiştir. Bu örneklerin akım-voltaj karakterizasyonları, farklı elektrot yapıları ile tamamlanmıştır. Çalışmanın ana odağı, dedektör kristallerinde oluşturulan metal-yarı iletken malzemenin akım-voltaj davranışlarını araştırmaktır. Akım-voltaj ölçümlerine ek olarak, üretim safhasının her aşamasında X-Işınım Kırılımı (XRD), Atomik Kuvvet Mikroskobu (AFM) ve Taramalı Elektron Mikroskobu (SEM) karakterizasyonları yapılmıştır.

Anahtar Kelimeler: Kadmiyum Çinko Tellür, X-Işınımı Dedektörü, Gamma Işınımı Dedektörü, Akım-Voltaj Ölçümleri

To my family…

ACKNOWLEDGEMENTS

By accepting me to the METU Crystal Growth Laboratory, Prof. Dr. Raşit Turan gave me the chance to step into the area of solid-state physics and opened a fresh and gleaming window of science in front of me. Moreover, the guidance and motivation he provided for me was invaluable. For these reasons, he has my upmost gratitude.

My co-advisor Prof. Dr. Mehmet Parlak was always helpful and supportive. Whether a scientific question or a problem of equipment, his theoretical and practical solutions were always there to help me. Therefore, I am thankful to him.

My group members, Ayşe Merve Ünalan, Özden Başar Balbaşı and Mustafa Ünal, all having an optimistic approach, either to me and to life in general, have turned even the most stressful times into a simple colorful challenge for me. But Mustafa Ünal, with his genuine solutions to the scientific problems we encountered and his jokeful threats about firing me from the CGL group has motivated me a lot. Nonetheless, I am thankful to all three of them for their friendship and scientific contributions to my thesis. Specifically, Ayşe Merve Ünalan contributed to the graphs by introducing me a proper scientific graphing tool. Özden Başar Balbaşı has helped me in doing some of the critical current-voltage measurements. Mustafa Ünal has played a key role in the SEM and AFM measurements we have done. He also contributed to the fabrication process of the samples.

Two of my friends from the physics department, Şahin Kürekci and Tuğba Andaç, deserve my appreciation. They have the power to be honest whatever the circumstances and have the ability to give their devotion and solidarity to me without any expectation. These are the things that I found priceless in their friendship.

Last but not least, my deceased father, who did everything in his power, for his children to become educated and trustworthy men, and my mother who did the same and is still doing... Their encouragement and support through all my life was a fortune in this world that I am most grateful.

TABLE OF CONTENTS

LIST OF TABLES

TABLES

LIST OF FIGURES

FIGURES

LIST OF ABBREVIATIONS

AFM – Atomic Force Microscopy

CGL – Crystal Growth Laboratory

CZT – Cadmium Zinc Telluride

EDS – Energy Dispersive X-Ray Spectroscopy

MEMS – Micro-Electro-Mechanical Systems Research and Application Center

METU – Middle East Technical University

MSM – Metal Semiconductor Metal

SEM – Scanning Electron Microscopy

SIMS – Secondary Ion Mass Spectroscopy

THM – Travelling Heater Method

UV – Ultra Violet

VGF – Vertical Gradient Freeze

XPS – X-ray photoelectron spectroscopy

XRD – X-ray Diffraction

CHAPTER 1

INTRODUCTION

1.1 Prologue

Since the discovery of X-rays by Wilhelm Roentgen in 1895 and discovery of radioactivity by Henri Becquerel in 1896, detection of radiation from radioactive sources have become more and more crucial for human endeavors, whether industrial, commercial or scientific.

Radiation detection as a type of advanced technology has innumerable application areas. To give an account of the broad range that this technology can be used, one can enlist the following domains or sectors like national security devices (radioactive material detectors at borders or airports), medical utilization (medical diagnostics and treatment devices), commercial uses (test and measurement techniques in manufacturing, especially in food industry), environmental remediation and safety efforts, and space instrumentation [1]–[3].

The practical use of semiconductors as radiation detectors goes back to the first half of 1960s. At that time these initial versions were called “crystal counters”. In time, they have gain more proper names like “semiconductor diode detectors” and more recently they are to be called as “solid-state detectors” [4]. In the realm of this thesis they will be usually called as CdZnTe detector crystal or simply as CdZnTe crystal interchangeably.

For the last thirty years, there has been a growing interest and numerous studies on the utilization of CdTe and CdZnTe compound semiconductors as radiation detectors. Among others, these two compounds have stepped forward as the most promising materials to detect radiation with high detection efficiency, good energy resolution and operability at room temperature [5].

As will be discussed in following chapters in detail, at certain energy levels (up to 1 MeV), the primary mechanism that X-rays and gamma rays interact with matter is

photoelectric absorption with an atomic number dependency of Z^{4-5}. CdZnTe having atomic numbers of 48, 30, 52, respectively, offers a very high mass attenuation coefficient and related with that, outstanding detection efficiency. Furthermore, the wide bandgap that CdZnTe possesses, gives rise to the high resistivity and helps to lowering leakage current, which allows the detector to work at room temperature while maintaining high spectral resolution [6].

1.2 Thesis Motivation

For the last five years METU Crystal Growth Laboratory has accomplished initial steps in the full production cycle of detector crystal fabrication. Starting from the construction process, several studies have been conducted about the bulk growth characterizations and temperature modellings [7], [8]. Moreover, studies on defects specific to the CdZnTe bulk crystals and surface characterizations were also completed [9], [10]. Although research activities on these subjects are still continuing, a critical phase has emerged as the next step toward the fabrication of a complete radiation detector made from CdZnTe crystals. In this phase, an investigation on the electrical properties such as resistivity, surface leakage current and metal contact formation is needed. This M.Sc. study is focused on these aspects that are crucial for detector applications. Two major topics have been studied in this study: first one is the production of CdZnTe crystals with proper contacts enabling current-voltage measurements. For this end, the ability to etch the crystal surfaces and deposit metal contacts on them was imperative. Second one is to take current-voltage (I-V) measurements and extract resistivity from these measurements and interpret them in connection with structural-chemical properties of the crystal.

For CdZnTe crystals, there are numerous studies in literature about the metal contact deposition methods such as thermal evaporation and sputtering [11]–[15]. But in this thesis study, because of its advantages mentioned in Chapter 3, electroless deposition was chosen as the method of contact deposition. As a result, during the thesis study all the metal contact depositions were made with the electroless method and any comparison with other deposition methods has been reserved for a future study.

1.3 Thesis Overview

After the introduction, the thesis starts with an explanatory chapter that gives the theoretical foundations of the two areas establishing this study. Namely, radiation detector physics and CdZnTe crystals and their properties. These subjects were described and explained in Chapter 2. In particular, this chapter consists of the basic theory of radiation, its interaction with matter, and the fundamental features of semiconductor radiation detectors. Moreover, one can familiarize with the properties of CdZnTe material, how it is grown and its distinctive properties as a radiation detector material.

Chapter 3 deals with the various fabrication and characterization methods that were employed. Fabrication methods such as cutting mechanism, lapping/polishing processes, chemical etching procedures and passivation practices are explained. In addition, characterization methods like photolithography and electroless gold deposition schemes are given.

Finally, Chapter 4 establishes the core of this thesis study and presents the achievements and challenges that have been experienced during the research. It begins with a structural analysis of the CZT samples that were produced and utilized. X-ray Diffraction (XRD) results will be presented at the beginning of the chapter. Then, some results of surface characterization techniques such as Scanning Electron Microscopy (SEM) and Atomic Force Microscopy (AFM) will be presented. Compositional investigations made with Electron Dispersive X-ray Spectroscopy (EDS) and Secondary Ion Mass Spectroscopy (SIMS) will also be reported. Lastly, current-voltage characteristics (I-V) of the produced detector crystals will be discussed as the backbone of the present thesis study.

At the end, in Chapter 5, which is a brief conclusion chapter, summarizes all the work done and contemplates about what should be done next.

CHAPTER 2

THEORETICAL BACKGROUND

A brief introduction concerning the following questions will be presented in this chapter. What is radiation? How radiation interacts with matter? What are the simple working principles of a semiconductor radiation detector? In addition, information about the growth of CdZnTe crystals is given with their material, optical, electronic properties and crystal structure.

2.1 Radiation: Basic Theory

Radiation can be considered as a form of energy that sometimes behaves as an electromagnetic wave and sometimes as a particle. Depending on the source and energy of the radiation, it can be in the form of a gamma ray, X-ray or other forms of waves such as microwave, radio wave, ultraviolet and infrared light. When the source of the interaction undergoes a transformation through a nuclear reaction, it may also radiate in the form of particles like alpha particles or beta particles, or even protons. Nowadays, all these types of radiation, whether having wave nature or particle nature, can be observed in accelerator experiments when protons were produced and collided with each other, in nuclear reactors where radioactive decay of atomic nuclei is used to produce electrical energy or even in our laboratories where x-rays and gamma rays can be produced for test and measurement purposes.

The primary aim of this study is to develop a semiconductor radiation detector crystal with a proper current-voltage behavior that eventually can spot and if possible distinguish X-rays and gamma rays. Hence it is convenient to give the typical energy ranges of both. In this respect, X-rays typically are in the range of 1 keV and 100 keV, while gamma rays usually situated at higher energy levels from 100 keV to 10 MeV [16]. For radiation physics, 1 electron volt ($1eV = 1.602 \times 10^{-19}$ J) is the standard measurement unit of radiation energy and it should be noted that

1eV is the kinetic energy gained by an electron when it is subject to acceleration at 1 volts of potential difference [17].

For the sake of generalization and the purpose of this study, radiation may be divided into two main categories: Ionizing radiation which includes familiar particles like beta particles (electrons and positrons), alpha particles, protons, X-ray and gamma rays and non-ionizing radiation which includes radio frequency radiation, microwaves and laser light [18].

But it should be kept in mind that categorizing radiation can also be done with a different approach. Instead of ionizing/non-ionizing distinction, one can justifiably use hazardous/non-hazardous radiation as a method of categorizing or it can be simply divided into two as wave radiation and particle radiation. Another important thing to consider is that these categorizations can make sense only if one understands them as a statistically meaningful quantity. For instance, accepting electrons as ionizing particles does not mean that one electron always ionizes atoms whenever it interacts with them. All one can say is that when a large quantity of electrons interacts with a large quantity of atoms, the definitive end result of this interaction would be the ionization of the atoms [19].

2.1.1 Ionizing Radiation

As the name suggests, this type of radiation ionizes atoms as it passes through the matter. There should be enough energy to separate bounded electrons from their orbits and when this happens atoms remain charged. The following pages give a brief account of the different variants of ionizing radiation.

First radiation type that should be mentioned is alpha particles. These particles are actually identical to the nuclei of helium (^{4}He) atoms. Having two protons and two neutrons, they are the most massive particles described here. Usually they are produced with alpha decay of heavy and unstable nuclei. The decay process is given in Equation 2.1 [20] where X and Y are the initial and final nuclear products.

$$ {}^{A}_{Z}X \rightarrow {}^{A-4}_{Z-2}Y + {}^{4}_{2}\alpha \qquad (2.1) $$

Most of the alpha particles have energies changing between 3 MeV to 7 MeV and they are considered as the most destructive type of ionizing radiation though they can be stopped with a sheet of paper [20].

The second radiation type to mention is beta particles. They are high energy particles with a twofold existence, electrons and positrons. In terms of mass, they are much less massive than alpha particles but they have more ionizing capability. Decay mechanisms that generate electrons and positrons are also twofold. Nuclei that have too many neutrons become unstable. By electron emission through beta minus (β^-) decay, electrons are produced. On the other hand, nuclei with too many protons undergoes positron emission through beta plus (β^+) decay to produce positrons. The defining schemes are given below in Equation 2.2 and Equation 2.3 [20] for both electrons and positrons respectively, where ν_e is the neutrino and $\bar{\nu}_e$ is the anti-neutrino:

$$n \rightarrow p + e^- + \bar{\nu}_e \tag{2.2}$$

$$p \rightarrow n + e^+ + \nu_e \tag{2.3}$$

and the general beta decay process can be expressed schematically as in Equation 2.4 [20]:

$$^{A}_{Z}X \rightarrow {}^{A}_{Z+1}Y + \beta^- + \bar{\nu} \tag{2.4}$$

where X and Y are initial and final nuclear products and $\bar{\nu}$ is anti-neutrino again.

Another type of particle is protons. It can be said that these particles are the crown jewels of today's accelerator physics. They are elementary particles with a positive elementary charge e^+ and with neutrons they constitute nucleons.

All these radiation types defined up to this point are charged and those given below are uncharged. Except neutrons, the following ionizing radiation types, X-rays and gamma rays, constitute the fulcrum of this sub-section.

Neutrons. These are neutral particles and when they are free they form neutron radiation as a type of ionizing radiation. They are usually caused by nuclear reactions like nuclear fusion or nuclear fission.

Second uncharged type of radiation are X-rays. The energy levels that X-ray photons possess are sufficient for them to ionize the atoms they interact with. They lie between gamma rays and ultraviolet light in the electromagnetic spectrum and usually named as soft X-rays when they have energies between 100 eV and 10 keV and as hard X-rays when they have energies between 10 keV and 100 keV. Three main interaction types occur when X-rays pass through a bulk of matter, photoelectric absorption, Compton scattering and Rayleigh scattering, which will be explained in the following section. The energy of the X-rays usually determines the type of interaction. While photoelectric absorption dominates soft X-rays, Compton scattering becomes the dominant interaction type for hard X-rays.

X-rays are generated by several transition processes. In the ground state of an atom, electrons are placed in their orbits so that the atom is in the lowest energy. When this state is disrupted by some excitation process the orbital electrons reconfigure themselves into higher orbits which are usually empty. But the nature of the atoms forces them to be in the lowest energy level possible. As a result, the vacant holes are filled with electrons from higher energy levels. In this returning process energy is and the so called “characteristic X-rays” are emitted. For instance, if an electron returns from the L shell to the lower K shell, it emits a K_α photon. If it returns from M shell to K shell, then a K_β photon is emitted which will have larger energy than the previous K_α since it covers a larger binding energy between the shells K and M. Figure 1.a depicts the creation of characteristic X-rays and Figure 1.b shows the intensity of the x-rays as a function of energy [21].

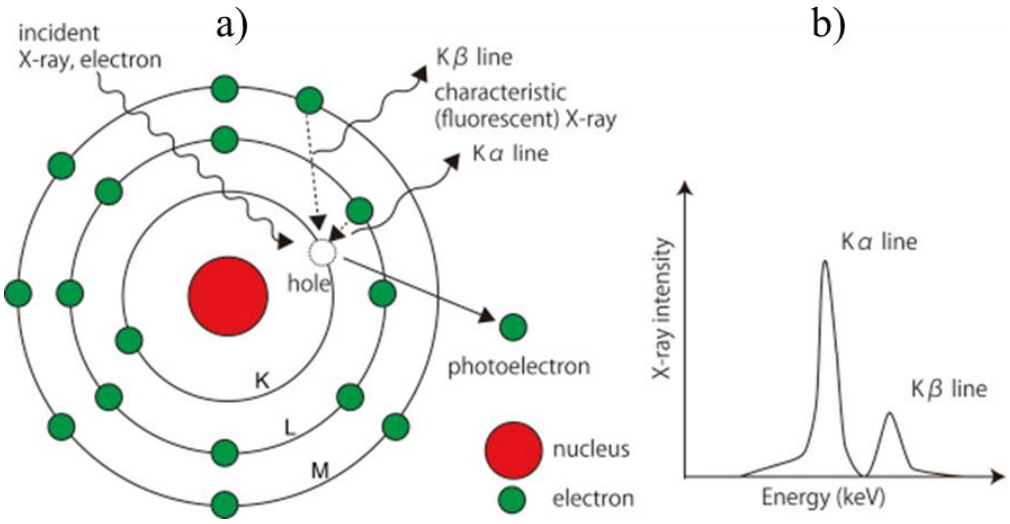

Figure 1. a) Creation mechanism of characteristic X-rays, b) Intensity of X-rays as a function of energy.

When an electron moves from an unbound or free state to the K shell and fills a vacancy there then the maximum energy photon in K-series will be generated. K-series photons are more essential than the other series since they have greater energies. One important thing to mention here is the fact that there is a correlation between the energies of a series and the atomic number of elements. Energy increases with increasing atomic number. X-ray energies for sodium with atomic number Z=11 can reach 1 keV for instance. On the other hand, energies of 100 keV can be reached in radium which has an atomic number of Z=88 [4].

Last type of uncharged radiation are gamma rays. These rays have a strong tendency to penetrate matter hence they have the highest photon energy among the radiation types discussed here. Although there is a region in the electromagnetic spectrum where gamma rays and X-rays may overlap and the distinction is not clear, traditionally gamma rays are considered as having energies greater than 100 keV and may rise up to the orders of several mega electron volts (MeV) in terms of energy. In general, there are celestial sources of gamma rays like supernova explosions, neutron stars, pulsars and black holes. But there are also less dramatic and earthlier events that can be considered as a gamma ray source like a decay of radioactive element or a fission process occurring in nuclear reactor. Some common

gamma ray sources and their decay schemes can be found in literature [4]. Among them, the most common ones are Co^{57} and Cs^{137} for investigating the spectroscopic properties of CdZnTe crystals. In this respect, the 122 keV gamma rays from Co^{57} and 662 keV gamma rays from Cs^{137} are the most widely used energy levels. But in this study, they are not utilized since the spectroscopic properties is a subject of a broader research.

The high detection efficiency of CZT crystals is important to detect highly energetic gamma rays. The atomic numbers that the three elements possess give an advantage to CdZnTe material in terms of stopping power. Since the relatively high electron numbers increase the interaction probability of gamma rays. Figure 2 shows the absorption efficiency of CdZnTe crystals depending on the thickness of the detector crystal. As can be seen from the figure, the absorption efficiency of a 15 mm thick detector crystal can stop the 122 keV photons with 100% efficiency. When it comes to 662 keV photons, absorption efficiency is 45%, which is still a good efficiency value for practical applications [22].

Gamma rays can be detected by interactions such as photoelectric absorption, Compton scattering and pair production, which will be explained in the next section.

2.1.2 Non-Ionizing Radiation

This type of energy cannot reach the required levels needed to separate a bound electron from its orbit and cannot ionize atoms. Therefore, they carry no significance for the realm of this thesis. In the electromagnetic spectrum they cover the region from extremely low frequencies to radio waves and up to ultraviolet light region.

2.2 How Radiation Interacts with Matter

There exist several mechanisms that energetic photons can interact with matter. In this section they will be explained and graded according to the importance they carry in terms of detector physics and radiation measurements. Photoelectric absorption, pair production and Compton scattering can be immediately pointed out.

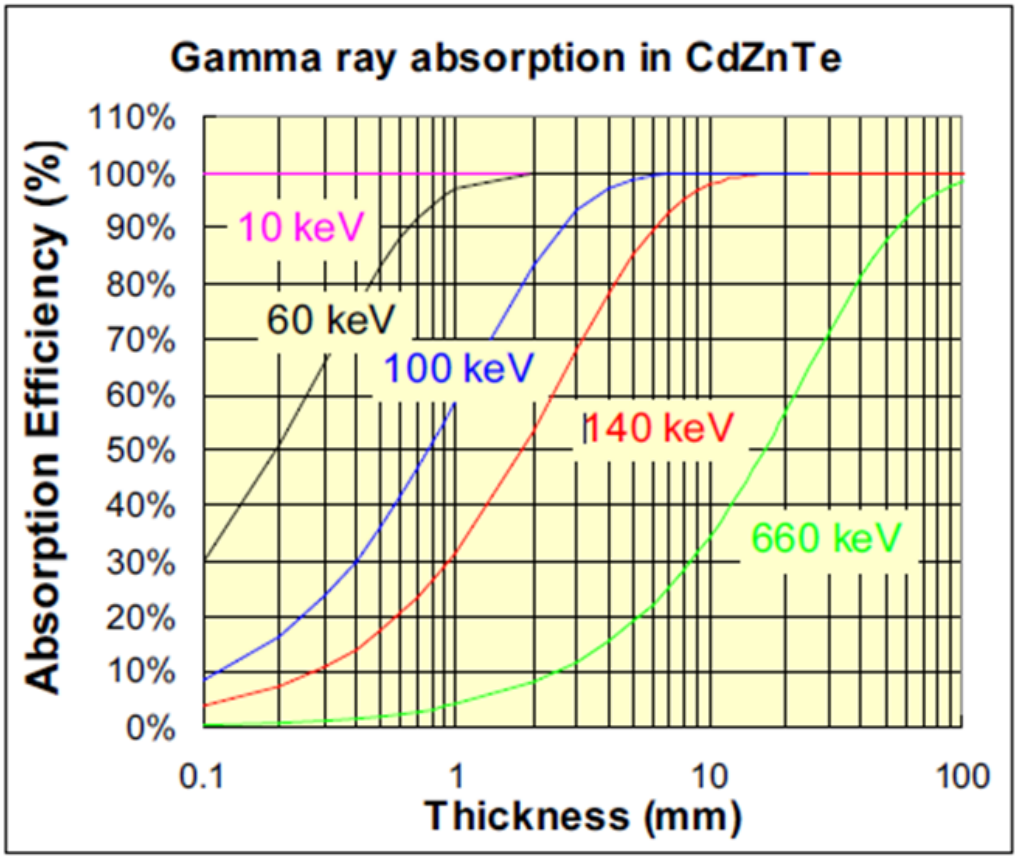

Figure 2. Absorption efficiency versus detector thickness for gamma rays [22].

Regardless of the type of interactions, there are some fundamental mechanisms involving in radiation versus detector encounters and they have a critical role in proper functioning and design of any type of radiation detector. For practical concerns, the nature of the interaction should involve a transfer of energy from the incident photon to the electrons or nuclei of the atoms forming the detector material. If an interaction occurs without any transfer of energy, then the radiation may pass through the detector without leaving any trace to be searched for. Such a case will not be different from a situation in which no interaction has ever occurred.

Stopping distance is another fundamental mechanism usually named as “range”. An alpha particle, being heavily charged, interacts with the absorber atom’s orbital electrons through coulomb forces. In some rare occasions they may also interact with the nuclei itself. In a single interaction, only a small amount of particle energy

is transferred (about 1/500 of the particle energy per nucleon) [4]. Hence for a penetrating charged particle to be slowed down and to be stopped, multiple interactions will have to occur. Since this process of losing energy is a gradual one, the charged particle direction will not deflect radically from its initial direction and therefore one can define a precise "range" for the specific particle in a given absorber material.

Another important concept is the linear stopping power denoted with *S*, which can be defined as the rate of change in the energy that is lost as the path length changes [4] and given in Equation 2.5.

$$S = -\frac{dE}{dx} \tag{2.5}$$

The value on the right side of the Equation 2.5 is also known as "specific energy loss", and it is defined by a formula known as "Bethe formula" [4], given in Equation 2.6. It simply conveys the message that, for a given charged particle, the linear stopping power increases as the velocity of the particle decreases and/or as the charge of the particle increases:

$$-\frac{dE}{dx} = \frac{4\pi e^4 z^2}{m_0 v^2} NB \tag{2.6}$$

where, *v* and *z* are the velocity and charge of the initial particle respectively, *N* is the number density of the absorbing atoms, m_0 is the rest mass of the electron and *e* is the charge of it [4]. *B* can be defined as in Equation 2.7:

$$B \equiv Z\left[ln\frac{2m_0 v^2}{I} - ln\left(1 - \frac{v^2}{c^2}\right) - \frac{v^2}{c^2} \right] \tag{2.7}$$

where, Z is the atomic number of the absorbing atom and I is an experimentally determined number which defines the average excitation and ionization potential of the absorber element [4]. It should be noted that for non-relativistic particles only the first term in B is important. Besides the number density (N), atomic number (Z) also plays a role in determining the linear stopping power. There are some variations of the Bethe formula like the one accommodated for fast electrons which are not included in the scope of this text. More can be found in the subsection 2.2.4 which is about the attenuation of gamma rays.

Without having charge, energetic photons like X-rays or gamma rays interact with matter differently than charged particles which was briefly revealed. When it comes to X-rays and gamma rays, only three types of interaction matter and these are explained in the following pages. In all these three encounters, a partial transfer or a complete transfer of energy can occur. This transfer of energy appears suddenly and results with abrupt modifications. At the end, the interaction causes a change in the detector material that can be quantified and measured. This change may correspond to a shift in temperature, a variation in current or even a chemical or nuclear transformation inside the detector.

2.2.1 Photoelectric Absorption

Photoelectric absorption, graphically shown in Figure 3, is the process of total disappearance of the incoming photon, which is realized when photon interacts with the atom as a whole. Due to the conservation laws of energy and momentum, in place of the photon, a photoelectron will emerge from one of the bound shells of the absorbing atom. A free electron cannot trigger such a huge transformation and for gamma rays with sufficient energy this bound shell is usually the tightest one, that is the K shell of the atom. The mathematical statement expressing this interaction is given in Equation 2.8:

$$E_{e-} = h\nu - E_b \tag{2.8}$$

where, E_{e-} is the energy of the photoelectron after the interaction happens, $h\nu$ is the incoming photon energy before the interaction (which may also be termed as E_p) and E_b is the binding energy of the photoelectron in its initial shell [4].

Besides the newly created photoelectron, another result of the interaction is an ionized atom of the absorber in which there is a bound shell with a vacancy. This vacant shell will be filled by its surrounding electrons, either by capturing a free electron or by modification of electrons from the other shells of the atom. When this happens, it also generates one or more characteristic X-rays and in some rare occasions even Auger electrons may be emitted instead of characteristic X-rays. When an outer shell electron fills an inner shell, the energy originated from this transition may separate another electron at outer shells of the same atom. This process sometimes takes the role of carrying excitation energy of the atom and is called as "Auger effect". Auger electrons usually carry low energies and therefore they can only travel very short distances inside the material.

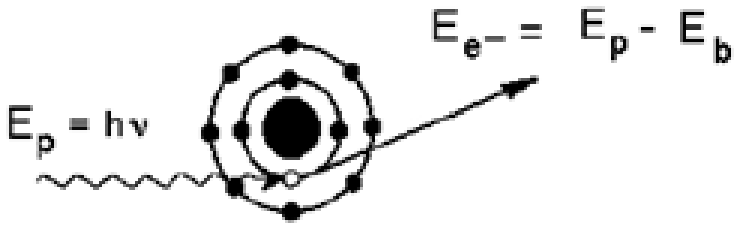

Figure 3. Photoelectric absorption [18].

The complexity of the photoelectric absorption process can be clarified with an example. When incident photons with energies above 30 keV go through xenon (Xe) atoms the following happens: 86% of the photons interact with the K shell of the xenon atom and 87.5% of them emit K shell characteristic X-rays. The rest of the 12.5% emit Auger electrons. Remaining 14% of the incident photons interact with L or M shell electrons and will also result with characteristic X-rays and Auger electrons with less energies [23].

For relatively low energies of gamma or X-rays (up to several hundred keV), the dominant type of interaction is photoelectric absorption process. This process intensifies further with the increasing atomic number Z of the absorbing material. Although it is not possible to give a definitive statement about the probability of photoelectric absorption per atom (τ), including all the energy ranges of interacting photons and all levels of atomic numbers, an approximation can be given to define the picture as in Equation 2.9 [24]:

$$\tau \cong constant \times \frac{Z^n}{E_\gamma^{3.5}} \tag{2.9}$$

where, n in the exponent of Z corresponds to a region between 4 and 5 for the gamma ray energy domain that we are interested. Equation 2.9 illuminates the importance of high Z number and the reasoning behind CdZnTe as an advantageous detector material with relatively high atomic number elements (Z_{Cd} = 48, Z_{Zn} = 30, Z_{Te} = 52). Since the probability of photoelectric absorption (τ) increases with high Z, according the relation given in Equation 2.9. The simple fact that high atomic number elements have more electrons is the main cause of this result.

2.2.2 Compton Scattering

Compton scattering is another type of interaction which is very important both for the purpose of understanding gamma ray interactions (X-ray interactions also) and for the domain of this work. The energies involved in this mechanism are in the range that corresponds to typical radioisotope sources. In Compton scattering, the photon interacts with an electron and scatters with an angle θ, while transferring some part of its energy to the newly emerging "recoil electron". Figure 4 sketches the interaction clearly and simply with before and after phases.

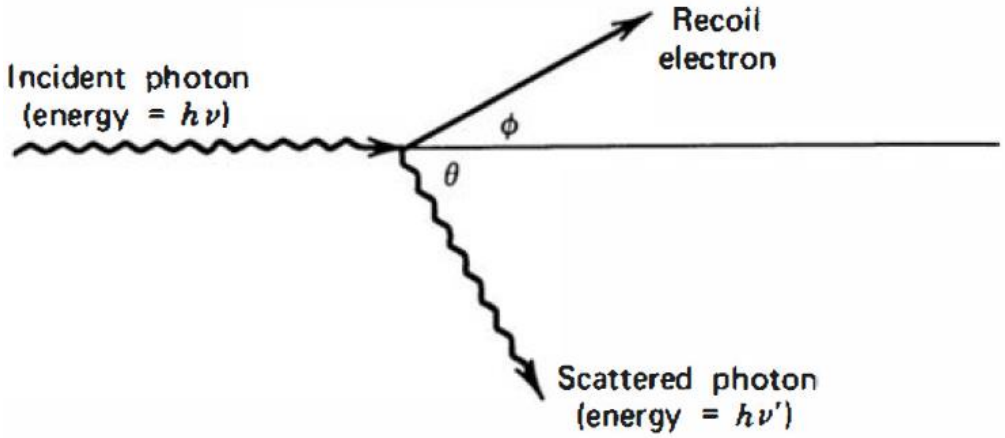

Figure 4. Compton Scattering [4].

The event described in Figure 4 can be turned into a mathematical expression that explains the energy distribution in Compton scattering, with the help of energy and momentum conservation principles, Equation 2.10 can be written [4].

$$h\nu' = \frac{h\nu}{1+(h\nu/m_0c^2)(1-\cos\theta)} \tag{2.10}$$

where, the energy of the scattered gamma ray is $h\nu'$ and it is given in terms of scattering angle θ and the energy of the incoming gamma ray $h\nu$. The rest mass energy of the electron is 0.511 MeV and is depicted as m_0c^2. From these values the kinetic energy of the recoiling electron can easily be calculated as in Equation 2.11 [18].

$$E_{e-} = h\nu - h\nu' = h\nu\left(\frac{(h\nu/m_0c^2)(1-\cos\theta)}{1+(h\nu/m_0c^2)(1-\cos\theta)}\right) \tag{2.11}$$

According to the values that scattering angle θ can take (from $\theta = 0$ to $\theta = \pi$), two extreme situations can be defined:

1. Where scattering angle θ takes values close to zero or equal to it. In this case, Equation 2.10 suggests that the values of hv' and hv are equal to each other since cos θ is one when $\theta = 0$ and right side of the denominator after the plus sign becomes zero. Equation 2.11 on the other hand tells us that recoil electron energy E_{e-} becomes zero. In this extreme case, the scattering gamma ray conserves the incident photon energy to a large extent.
2. Where scattering angle θ takes the value π or values around it and this causes a head-on collision in which the incident gamma ray may backscatter while the recoil electron emerges with an opposite direction of the incident photon. Here, a maximum of the incident photon energy can be transferred to the recoil electron in one interaction. Then Equation 2.10 and Equation 2.11 will produce the following results depicted in Equation 2.12 and Equation 2.13.

$$hv'_{(\theta=\pi)} = \frac{hv}{1 + 2hv/m_0c^2} \tag{2.12}$$

$$E_{e-(\theta=\pi)} = hv\left(\frac{2hv/m_0c^2}{1 + 2hv/m_0c^2}\right) \tag{2.13}$$

Actually, all scattering angles are possible in a detector. Besides these two extreme values defined above, a continuum of energies is probable for the recoil electron.

As in the case of photoelectric absorption, atomic number of the elements constituting the detector material is crucial in the probability of Compton scattering per atom, since the number of electrons as scattering targets increases with the number of *Z*. This is also valid for pair production.

2.2.3 Pair Production

The rest mass energy of an electron is 0.511 MeV as mentioned before. Twice of this value (1.022 MeV) is an exotic level of energy for the particle physicists since it conveys the possibility of pair production. Simply put, the gamma ray photon disappears in the coulomb field of the nucleus and two other particles will emerge as an electron-positron pair. This mechanism predominates the gamma ray interactions with relatively high energies, between 5 to 10 MeV or sometimes above. Since only 1.022 MeV of energy is required, excess energy from the interaction is redistributed to the electron and positron in the form of kinetic energy. This fact is stated in Equation 2.14 where hv is again the incident photon energy.

$$E_{e-} + E_{e+} = hv - 2m_0c^2 \tag{2.14}$$

Positron tends to annihilate because it is not as stable as electron and produces what is called as "annihilation photons". These secondary products have the potential to affect the response of gamma ray detectors [4]. Unfortunately, it is not possible to write a single formula expressing the probability of pair production per nucleus. However, it can be said that, with increasing energies the probability also increases. This can be seen most evidently in Figure 5, where three leading interaction types of gamma rays are depicted relative to each other with energy and atomic number are considered. The two solid lines in Figure 5 are representing the energy levels where interactions have equal chance of happening.

2.2.4 Attenuation of the Gamma Rays

An important concept to mention is the linear attenuation coefficient μ. It can be defined as the probability per unit path length given by the sum of these probabilities for each interaction shown in Figure 5. It is given in Equation 2.15 [4].

$$\mu = \tau\,(\,Photoelectric\,) + \sigma\,(\,Compton\,) + \kappa\,(Pair) \tag{2.15}$$

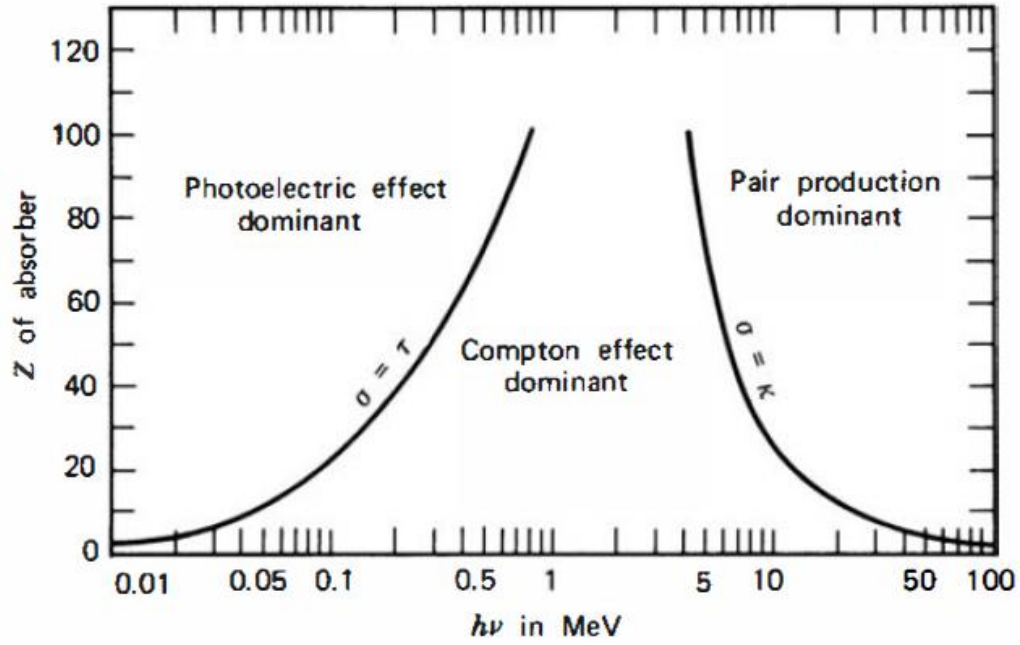

Figure 5. Three leading interaction types of gamma rays [24].

With the help of μ, one can find the transmitted photons, that is their intensities I, as opposed to the incoming photon intensity I_0.

$$\frac{I}{I_0} = e^{-\mu t} \tag{2.16}$$

Here, μ should not be mixed with charge mobility of electrons or holes and t is the material mass thickness with units of [g • cm^{-2}]. In addition, the material density ρ can be included into the concept of linear attenuation coefficient and with its help the mass attenuation coefficient can be found. This changes Equation 2.15 and Equation 2.16 respectively into Equation 2.17 and Equation 2.18 [4].

$$\frac{\mu}{\rho} = \rho\,(\,\tau + \sigma + \kappa\,) \tag{2.17}$$

$$\frac{I}{I_0} = e^{-\frac{\mu}{\rho}t} \tag{2.18}$$

Figure 6 illuminates the picture where the contribution of mass attenuation coefficients was depicted for CdZnTe material. The green dashed line for photoelectric absorption includes some discontinuities caused by enhanced interaction probabilities at certain energies. Different electron shells of the elements in CdZnTe are responsible for them. For instance, the K shell of tellurium has the highest energy edge.

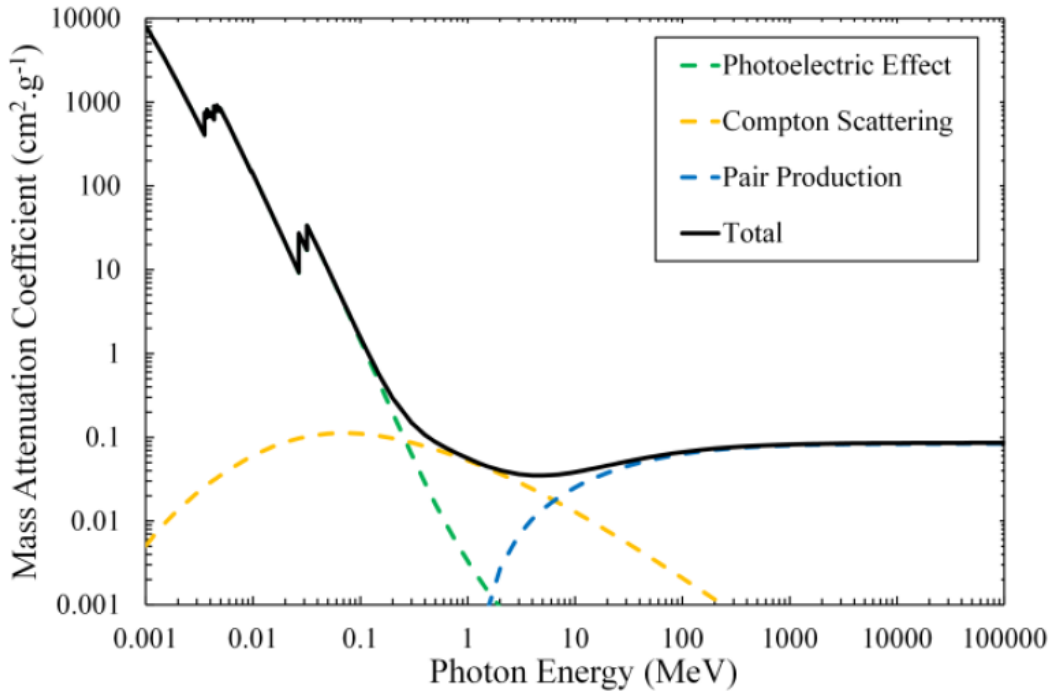

Figure 6. The contribution of mass attenuation coefficients in CdZnTe according to three main interaction types [6].

For analyzing the behavior of gamma rays inside the detector, a complementary tool to the linear attenuation coefficient is the mean free path length λ. It is the average distance that is travelled by gamma ray photons before they interact inside the

detector material. Mathematically, it is the reciprocal of linear attenuation coefficient and shown in Equation 2.19.

$$\lambda = \frac{1}{\mu} \tag{2.19}$$

For typical gamma ray energies, the mean free path may change from a few millimeters to several centimeters inside the absorber material.

To sum the relation between the atomic number Z and the probabilities of each main interactions, it can be said that for photoelectric absorption Z is proportional with Z^n where n is between 4 and 5. For Compton scattering it is only Z and for pair production it is proportional with Z^2 [16].

2.2.5 Elastic Scattering

To complete the picture, elastic scattering should be explained. In elastic scattering no exchange of photon energy takes place. As is shown in Figure 7, the incident photon merely deflects from its original path and scatters with a different direction when the interaction occurs. Since there is no energy deposited to the detector material in terms of measurement principles, elastic scattering can be considered as non-influential. This type of interaction usually happens at low energies and the probability of its occurrence is proportional to the square of the atomic number and inversely proportional to the incident photon energy.

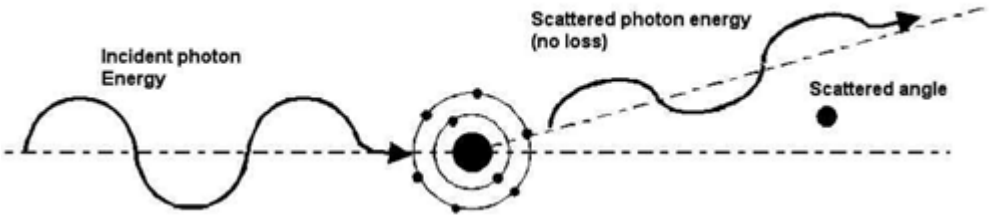

Figure 7. Elastic Scattering [25].

2.3 Radiation Detectors

2.3.1 Ionization Chambers

Ionization chambers can be considered as one of the oldest and simplest of all gas filled detectors. The simple principle they depend on can be explained as follows: when a charged particle passes through a gas, the gas molecules are ionized and excited along the track of the particle. The ion pairs (positive ion and free electron) which are created along the path can be collected as electronic signals. The number of ion pairs that can be created, depends on the energy of the passing particle and also on the ionization energy of the gas molecules. By applying an electric field to the gas, ions and electrons will tend to move away from their original points and a net drift velocity will occur. Since electrons have lower masses than ions, their mobility is greater. The drift velocity is defined in Equation 2.20:

$$v = \frac{\mu E}{p} \tag{2.20}$$

where, v is drift velocity, μ is mobility, E is electric field and p is gas pressure [4].

2.3.2 Proportional Counters

Another type of the gas filled detectors is proportional counters. They depend on a method called gas multiplication which is used to amplify the charge created by the ion pairs inside the gas. The process of gas multiplication is formed by applying high voltage and increasing the electric field. Since the mobility of electrons are greater they gain more acceleration as a result of the applied field. At some point, their kinetic energy reaches a level enough to ionize the gas molecules. As a result, each free electron coming from an ion pair will create more free electrons in a form called Townsend avalanche. Because of this avalanche mechanism, proportional counters are more sensitive to the composition of trace impurities inside the gas [4].

2.3.3 Geiger-Mueller Counters

Like ionization chambers and proportional counters, these detectors are also gas filled and based on ionization. The avalanche mechanism is also used in Geiger-Mueller detectors but there is a self-limiting process that terminates the chain reaction after certain point of collective effects has been reached. Because of this self-limiting process, all Geiger-Mueller counters return the same amplitude of pulses, regardless of ion pair numbers created. As a consequence, they are not suitable for spectroscopic radiation analysis but still effective at radiation detection [4].

2.3.4 Scintillation Detectors

Scintillation process is still widely used for radiation detection and spectroscopy. Inorganic alkali halide crystals, especially sodium iodide; and organic based liquids and plastics can be used as scintillators. Usually, the inorganics are better at light output but, with some exceptions, they are slow in response time. On the other hand, organic scintillators are faster but their light output is lower. Whether organic or inorganic, the ideal scintillation material should have the following properties: first of all, it should be able to convert the kinetic energy of the incoming particle into a detectable light. This conversion should be linear, meaning that the light output should be proportional to the deposited energy. Second, for a good light collection, the material should be transparent in the region of wavelength that corresponds its own emission. Third, to generate fast signal pulses, the decay time of the induced luminescence should be short [4].

Photomultiplier tubes, as a complementary device for scintillation process, play a crucial role in converting the weak light output of a scintillation pulse into usable electric signal without adding a great amount of noise. Basically, a photocathode inside the photomultiplier converts the incoming photons into low energy electrons. As a result, more reliable electric signals can be produced.

However, the main concern of this study is about a semiconductor-based radiation detector. For this purpose, a special semiconductor crystal called CdZnTe is being used. Therefore, the rest of this chapter contains information on semiconductor-

based radiation detectors in general and this specific CZT material and some of its properties.

2.3.5 Semiconductor Detectors

As opposed to gas filled detectors, semiconductor detectors offer better energy resolution. Since solids have greater densities than gases, it is possible for solid materials to create larger number of charge carriers corresponding to incident radiation event. The intrinsic charge carriers are electron-hole pairs. Like the gas filled detectors, the simple principle is to apply electric field and direct the charge carriers towards appropriate collection mechanisms as electric signals. Silicon and germanium are the traditional elements that are commonly used for this type of detectors [4]. But lately, CdZnTe crystals were taken the lead on this matter.

For a given radiation energy, the signal that can be collected from the electron-hole pairs will fluctuate around a mean value *N*, which can be defined by Equation 2.21:

$$N = \frac{E}{\epsilon} \tag{2.21}$$

where, E is the energy that carried with incident radiation and absorbed by the detector, ϵ is the mean energy required to create an electron-hole pair. The variance in N can be found by Equation 2.22 by including the Fano factor F [15].

$$\langle \Delta N^2 \rangle = FN = F\frac{E}{\epsilon} \tag{2.22}$$

If all the incoming energy is transferred into the creation of electron-hole pairs then N will be fixed and there will be no variance, hence the Fano factor will be zero. The main reason that Fano factor was introduced is the observed statistical fluctuation in

the number of electron-hole pairs which shows a discrepancy from the pure Poisson statistics [4].

2.3.5.1 Mechanisms of Charge Transport and Charge Collection

Charge transportation is an important parameter for semiconductor radiation detectors. In order to understand the mechanism of charge transport, mean drift length (λ_e, λ_h) is essential. For semiconductors, drift length is decided by the electron-hole mobility-lifetimes and by the applied electric field. Equation 2.23 and Equation 2.24 depict the mathematical expressions for electron and hole mean drift lengths respectively.

$$\lambda_e = (\mu\tau)_e \boldsymbol{E} \tag{2.23}$$

$$\lambda_h = (\mu\tau)_h \boldsymbol{E} \tag{2.24}$$

where, $\boldsymbol{E}$ is the electric field inside the detector material and $\mu\tau$ is the mobility-lifetime product. For an efficient charge collection inside the detector, the mean drift length should be comparable to the thickness of the detector, greater if possible. In order to get very large mean drift length, sometimes a few thousand volts may be required to apply to the device at hand [15]. For CdZnTe, by taking the value given in Table 2.1 for $(\mu\tau)_e = 10^{-3}$ cm^2/V and considering $\boldsymbol{E} \approx 1000$ V/cm, it can be predicted that for electrons, mean drift length can be a centimeter in length. But for holes, with the same electric field the mean drift length will be two orders of magnitude lower, since $(\mu\tau)_h = 10^{-5}$ cm^2/V [5].

Using drift length one can reach drift velocities of the electrons and holes by taking lifetime to the other side of the equality. Equation 2.25 and Equation 2.26 give drift velocities of charge carriers.

$$v_e = \mu_e \boldsymbol{E} \tag{2.25}$$

$$v_h = \mu_h \boldsymbol{E} \tag{2.26}$$

Electric field can also be found by taking the gradient of scalar potential inside the detector, as is shown in Equation 2.27.

$$\boldsymbol{E} = -\nabla V \tag{2.27}$$

When there is no field inside the detector, the average displacement of a charge carrier will be zero because of the random motions. However, the presence of an electric field accelerates the charge carriers into a direction determined by the field and a net average drift velocity will occur [15].

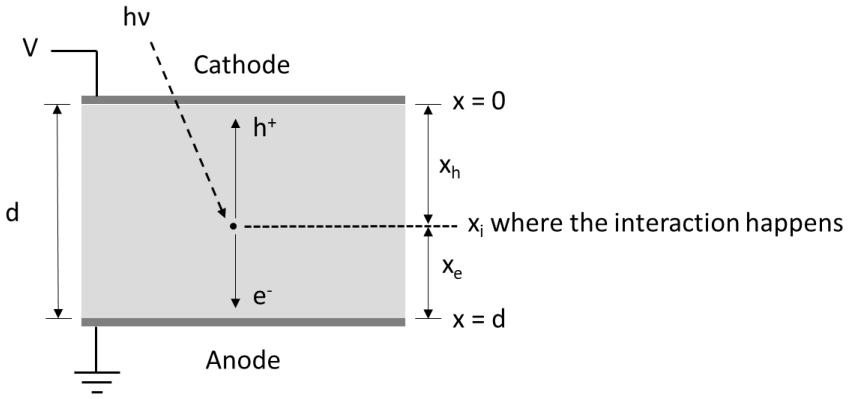

Figure 8. Illustration of charge carrier movements in a planar geometry detector, after a radiation interaction happened.

Figure 8, in a very simplified way, depicts the movement of electron-hole pairs after a radiation interaction. Usually, after a radiation interaction, too many electron-hole pairs are created inside the detector. The presence of electric field will help to separate electron-hole pairs and electrons will move to the anode while holes will move to the cathode. Assuming a time of *t* has passed after the interaction, the position of the electron and hole can be determined with the help of Equation 2.28 and Equation 2.29.

$$x_e(t) = x_i + tv_e \tag{2.28}$$

$$x_h(t) = x_i - tv_h \tag{2.29}$$

In conclusion, the simple working principle of a semiconductor radiation detector can be described briefly as the following: A photoelectron (or sometimes a Compton electron) inside the detector is created by the incoming radiation. Depending the pair creation energy, a number of electron-hole pairs will be created. Due to the effect of electric field, these pairs are separated and each carrier can be collected from the convenient electrode as electric signals [18].

2.3.7 CdZnTe as a Radiation Detector

Previously discussed interaction mechanisms which are triggered by highly energetic gamma ray and X-ray radiations, generate drastic changes inside the detector material. As mentioned before, these changes can be physical, chemical or even nuclear. In terms of detector physics, the creation of electron-hole pairs can be considered as the decisive one among these changes. Major parameters, like energy resolution and detection efficiency, are influenced by the variations in electron-hole pairs inside the detector, by the rate they are produced and by the rate they are collected.

Table 1 compares physical properties of CdZnTe with other semiconductors. At first sight, two properties depicted on this table strike attention. First, CdZnTe has the third highest resistivity value among the semiconductors shown. There is one order of difference between the resistivity of CdTe and resistivity of CdZnTe which is due to the addition of zinc (Zn) into the melt. High resistivity is good for preventing the leakage currents and allows the detectors to work at high voltages. Second, the mobility-lifetime products ($\mu\tau$) corresponding to CdZnTe are relatively low compared to silicon (Si) or germanium (Ge) which might appear as a drawback since good mobility-lifetime product is desirable for high charge collection efficiency [26]. However, manufacturing electron sensitive detectors could be a solution [5] for this drawback since the electron mobility is far better than hole mobility for CZT. In addition, three properties of CdZnTe which are responsible

from the growing interest for this material since the nineties [27], [28], can outrun this disadvantage. These properties are the relatively high density, relatively high atomic number and the wide bandgap. When compared to traditional semiconductors like silicon and germanium, the differences can be clearly seen in this regard at Table 1 [5]. Specifically, the wide bandgap of CZT is responsible for the favorable room temperature operation. Moreover, high atomic number and high density are responsible for the high detection efficiency. As stated before, addition of the zinc also helps to increase the bandgap [5].

Table 1. Physical properties of common semiconductors at 25°C temperature.

Material	Si	Ge	GaAs	CdTe	$Cd_{0.9}Zn_{0.1}Te$	HgI_2	TlBr
Crystal structure	Cubic	Cubic	Cubic (ZB)	Cubic (ZB)	Cubic (ZB)	Tetragonal	Cubic (CsCl)
Growth method*	C	C	CVD	THM	HPB, THM	VAM	BM
Atomic number	14	32	31, 33	48, 52	48, 30, 52	80, 53	81, 35
Density (g/cm^3)	2.33	5.33	5.32	6.20	5.78	6.4	7.56
Band gap (eV)	1.12	0.67	1.43	1.44	1.57	2.13	2.68
Pair creation energy (eV)	3.62	2.96	4.2	4.43	4.6	4.2	6.5
Resistivity (Ω cm)	10^4	50	10^7	10^9	10^{10}	10^{13}	10^{12}
$\mu_e\tau_e$ (cm^2/V)	> 1	> 1	10^{-5}	10^{-3}	10^{-3} - 10^{-2}	10^{-4}	10^{-5}
$\mu_h\tau_h$ (cm^2/V)	~ 1	> 1	10^{-6}	10^{-4}	10^{-5}	10^{-5}	10^{-6}

* The more common growth methods: C = Czochralski, CVD = chemical vapor deposition, THM = traveler heater method, BM = Bridgman method, HPB = high-pressure Bridgman and VAM = vertical ampoule method

2.4 Properties of CdZnTe Crystals

2.4.1 Crystal Structure

The crystal structure of CdZnTe is called zinc blende (or sphalarite, a word coming from Greek “sphaleros” = treacherous [29]) and can be defined as two interpenetrating face centered cubic (fcc) sub-lattices. While Cd/Zn nuclei occupy one sub-lattice, Te nuclei occupy the other and they offset one another by a quarter of a unit cell body diagonal, that is along the (111) direction [10], [16]. Figure 9 shows a simple view of zinc blende structure and each tellurium atom is surrounded by four zinc or cadmium atoms [30].

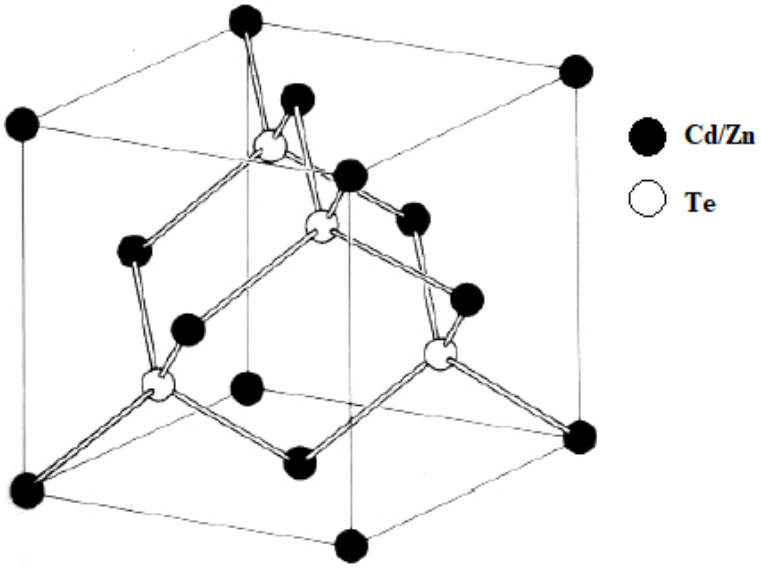

Figure 9. Zinc blende structure of Cd/Zn and Te compounds.

Zinc blende structure can also be described as a Bravais lattice having two point basis shown in Equation 2.30 and Equation 2.31 ($\sigma = (x, y, z)$ where x, y, z are orthogonal unit vectors) [16].

$$\sigma_1 = (0, 0, 0) \tag{2.30}$$

$$\sigma_2 = \left(\frac{1}{4}a,\ \frac{1}{4}a,\ \frac{1}{4}a\right) \tag{2.31}$$

$Cd_{1-x}Zn_xTe$ can be considered as a CdTe compound where Cd atoms are interchanged with Zn atoms with a "x" fraction of Cd atoms. Since there is a difference in lattice constants of ZnTe and CdTe, interchanging atoms cause a difference in the average unit cell dimension of CdZnTe. A simple approximation known as Vegard's law can express a relation between the alloy composition and lattice constant. Equation 2.32 presents this relation where a_1 and a_2 are lattice constants of CdTe and ZnTe respectively.

$$a(x) = a_1(1-x) + a_2 x \tag{2.32}$$

Since lattice constants of CdTe and ZnTe are specified as 6.4810 Å and 6.1037 Å respectively [31]. The lattice constant of $Cd_{1-x}Zn_xTe$ can be approximately found as 6.4433 Å (for x = 0.1) as shown in Equation 2.33.

$$a(x = 0.1) = 6.481(1-0.1) + 6.1037(0.1) = 6.4433\ \text{Å} \tag{2.33}$$

Addition of zinc (Zn) to the structure of CdTe crystal decreases the lattice constant and widens the bandgap. This is primarily caused by smaller atomic radii of zinc compared with cadmium. Moreover, the higher binding energy of ZnTe as opposed to CdTe, strengthens the lattice and causes a higher shear modulus, which is 1.83×10^{10} Pa for CdTe and 2.86×10^{10} Pa for ZnTe [32]. Addition of zinc also lowers the dislocation densities and sub-grain boundaries, which was verified experimentally [33].

2.4.2 Electronic Properties

It is known that CdTe and ZnTe are direct bandgap semiconductors, meaning that the momenta of electrons and holes are same in both the valence band and in conduction band. As a result, an electron can emit a photon directly [34]. Room temperature bandgaps of CdTe and ZnTe are ~1.55 eV and ~2.2 eV, respectively. Figure 10 shows the band structure of CdTe and the structure for ZnTe is similar. The band structure of $Cd_{1-x}Zn_xTe$ is quite a difficult problem because of the simple assumption that the band theory of solids is based on, that is periodicity. Due to the local composition fluctuations, periodicity is hard to find in ternary semiconductors or alloys like CZT [16].

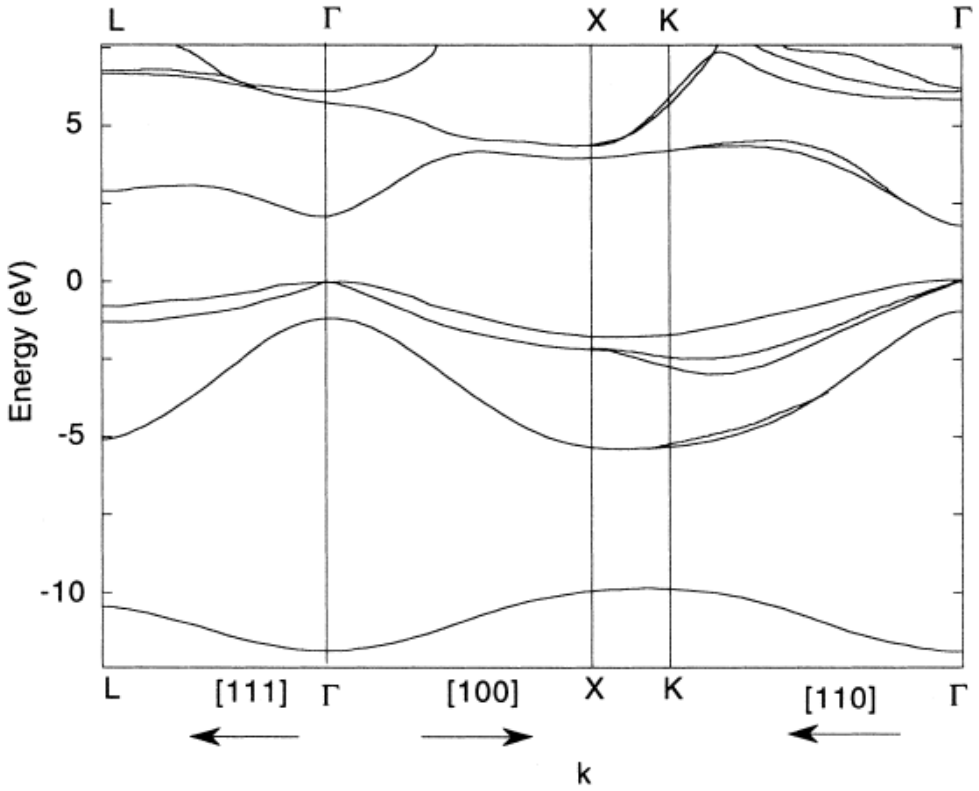

Figure 10. Band structure of CdTe depending on pseudopotential calculations [16].

Resistivity: The inverse of conductivity is known as resistivity and can be defined by Equation 2.34.

$$\rho = \frac{1}{\sigma} = \frac{1}{q(n\mu_n + p\mu_p)} \tag{2.34}$$

where ρ and σ are resistivity and conductivity respectively; q is electron charge, n is concentration of electrons, p is concentration of holes, μ_n is mobility of electrons and μ_p is mobility of holes.

For a semiconductor to be used as a radiation detector, it is important to have low concentration of free charge carriers. The reason for this is the fact that, free charge carriers produce a background current which interrupts any photocurrent arising

from a radiation interaction. This background current is called dark current and it causes noise that deteriorates the spectral resolution of the detector. If strong enough, it completely disrupts the radiation signal and prevents measurement [6].

Equation 2.34 also implies that high resistivity can have an impact on reducing the free charge carrier concentration. In a steady state condition, the free charge carriers will be in an equilibrium concentration, due to thermal excitation. This causes an inherent conductivity inside the semiconductor. By cooling the material, this concentration of charge carriers can be reduced. As a result, by cooling, the resistivity of a semiconductor can be increased. But cooling the material is expensive and also impractical in terms of device design. To sum up, cryogenic cooling of the semiconductor material or widening the bandgap can increase resistivity and in return decrease the concentration of free charge carriers. Since CdZnTe is a wide bandgap semiconductor it already has a high resistivity and does not require any cryogenic cooling to operate at room temperature. The reason behind its high bandgap is the addition of zinc into the cadmium-tellurium (CdTe) compound. The relation between the zinc concentration and the bandgap can be defined empirically and Equation 2.35 expresses this relation [31].

$$E_g(x) = 1.510 + 0.606x + 0.139x^2 \text{ eV} \tag{2.35}$$

With zinc concentration of 10% (x = 0.1), Equation 2.35 gives the bandgap energy as 1.572 eV, shown in Equation 2.36:

$$E_g(0.1) = 1.510 + 0.606(0.1) + 0.139(0.1)^2 \cong 1.572 \text{ eV} \tag{2.36}$$

High resistivity is necessary for a proper functioning of a semiconductor-based radiation detector but boosting it with the help of increased zinc concentration may

also have a drawback. When the bandgap increases, the energy required to create an electron-hole pair also increases. As a result, the number of carriers resulting from a radiation interaction inside the semiconductor decreases and the statistical noise related with the number of carriers will increase. Resulting with a deterioration of spectral resolution [6].

2.5 Metal-Semiconductor Contacts in CdZnTe Detectors

In order to use a semiconductor as a radiation detector, it has to be covered with metal contacts. There are different contact designs such as pixelated or strip designs. Even planar electrode designs can be used. Regardless of the electrode design, the simple working principle is the same, which is to apply electric field and collect charges generated by the ionizing process. In this study, usually pixelated metal contacts were used for the I-V measurement and resistivity calculation efforts. In addition, the preferred element of metal used for contacts was chosen to be gold (Au).

Because of the complicated nature that metal-semiconductor interfaces, it is not always easy to predict the behavior of any metal contact attached to a CZT crystal. There are several factors which play a role in the electronic response of a metal-semiconductor junction. One of these factors is the type of the contact metal and its work function. Another one is the type of semiconductor, its surface conditions and bulk properties. The method of contact deposition can also be listed. Lastly, the presence of any interfacial layers like oxides or contamination.

To explain the general behavior of any metal-semiconductor interface, complicated models have been developed [35]. Unfortunately, these models do not always result with exact compliance of the model and the actual application because of the many factors that play a role in the process, some of which enlisted above. In this section, basic physics concepts underlying the metal-semiconductor interfaces will be presented.

Ideally, when metal contacts are deposited on a semiconductor they will form either a rectifying or Ohmic contact. It appears that, in the case of a rectifying contact with

a semiconductor of n-type, the electrons will transfer from the semiconductor to the metal. With a p-type semiconductor, holes will transfer from the semiconductor to the metal. This transfer of charge carriers from semiconductor to the metal will continue until an equilibrium has reached, that is when the Fermi levels of both sides of the contact are equal. As expected, when charge carriers are transferred from the semiconductor to the metal it creates a depletion region on the surface level of the semiconductor.

On the other hand, in the case of an Ohmic contact, electrons will transfer from the metal to the n-type semiconductor and holes will transfer from the metal to the p-type semiconductor. Like in the rectifying contacts, this transfer will last until the Fermi levels of both sides of the contacts are equal and an equilibrium has been reached. Unlike the rectifying contacts, there appears no depleted region in the semiconductor surface.

Besides the type of the semiconductor (n-type or p-type), what determines whether the contact will be rectifying or Ohmic is the work functions of the metal (Φ_m) and semiconductor (Φ_s). The contact will be rectifying if the metal work function is smaller than the semiconductor work function ($\Phi_m < \Phi_s$) and the semiconductor is p-type. It will be Ohmic if the semiconductor is n-type. When the opposite is true, that is if the metal work function is greater than semiconductor work function ($\Phi_m > \Phi_s$), then the contact will be Ohmic on p-type and rectifying on n-type semiconductor. This correspondence can be more clearly seen in Table 2, where three metals (gold, platinum and indium) have been chosen for comparison with CdZnTe as the semiconductor. The reasoning behind tabulating these three elements is in fact that, for CZT detectors, gold (Au) and platinum (Pt) are the most used metals when fabricating MSM (Metal-Semiconductor-Metal) structures [5], and indium (In) with a suitable work function for comparison. Indium contacts are also possible for CZT detectors [36].

Table 2. Response of the metal-semiconductor contacts with some metals and CZT.

Metal \ Semiconductor (CdZnTe)		n – type	p – type
$\Phi_m > \Phi_s$	Au	**Rectifying** (Schottky)	**Ohmic**
	Pt	**Rectifying** (Schottky)	**Ohmic**
$\Phi_m < \Phi_s$	In	**Ohmic**	**Rectifying** (Schottky)

When a Metal-Semiconductor-Metal system is assembled together, interesting electronic responses will occur. No matter the nature of the response, Ohmic or rectifying, there will be a Schottky barrier affecting the movements of electrons and holes at the MSM junction, impeding the charge transfer from metal to semiconductor. This barrier is a voltage independent one and its effective height can be decreased by doping. In addition, there exist a barrier which can be called as a collection barrier [6], impeding the charge transfer from semiconductor to metal. This barrier can be removed by applying an appropriate bias voltage to the metal contact. Positive bias to remove the collection barrier for electrons and negative bias to remove the collection barrier for holes. Figure 11 shows this Schottky barrier in all four possible responses [37].

What will happen when bias is applied to the metal contacts of an MSM system? Below is a detailed description of this mechanism. Both cases of work functions ($\Phi_m < \Phi_s$ and $\Phi_m > \Phi_s$) will be explained. However, the focus will be on the second case which is more relevant for our study in which gold is used as contact material and the work function of gold is slightly greater than the work function of a CZT material ($\Phi_{m(Gold)} \approx 5.4$ eV $> \Phi_{s(CZT)} \approx 5.1$ [38], [39]). This is especially the case where $Cd_{1-x}Zn_xTe$ (x = 0.1), with high resistivity ($\rho > 10^9$ Ω cm), has its Fermi level

pinned at the half of the bandgap ($E_f = E_g / 2 = 1.57 / 2$ eV) or close to midgap [40]. Therefore, for a CZT crystal it is not always clear whether it is n-type or p-type.

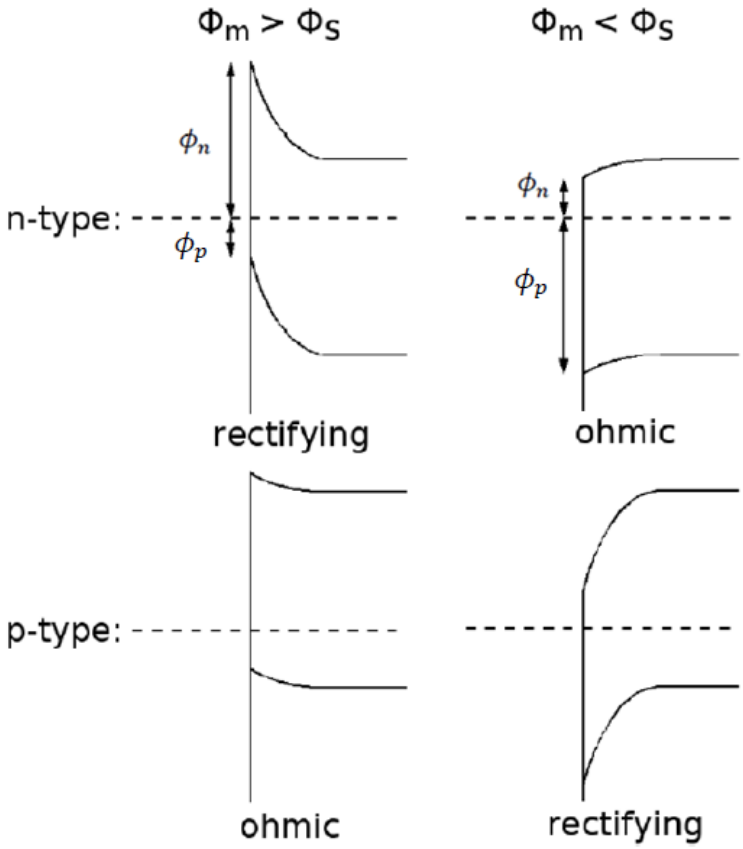

Figure 11. Schottky barriers existing in n- and p-type Metal-Semiconductor contacts.

When a metal-semiconductor-metal contact is formed, the immediate appearance of band diagrams can be drawn as in Figure 12.a and Figure 12.b [41]. Fermi levels are not equalized yet since the thermodynamic equilibrium is not reached. With time the system will move into a situation where a thermodynamic equilibrium is achieved, Fermi levels of metal and semiconductor will be equalized and contact barriers will begin to be effective in charge transfers between the metal-semiconductor-metal surfaces.

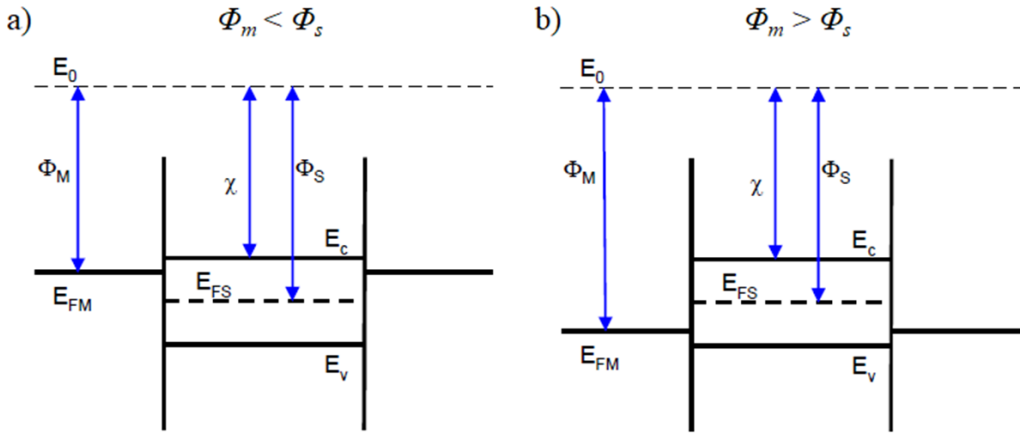

Figure 12. Band diagrams of an MSM contact where two cases are shown.

To be more specific about the notation used, "E_{FM}" is Fermi level of metal, "E_{FS}" is the Fermi level of semiconductor, "E_C" is the energy of the conduction band, "E_V" is the energy of the valence band, "E_0" is the energy of the vacuum. Also, "χ" is the semiconductor electron affinity, "Φ_m" is the metal work function, "Φ_s" is the semiconductor work function. In addition to these, contact potentials are denoted with "ϕ_n" and "ϕ_p" for electrons and holes respectively. Table 3 gives these quantities in an ordered fashion.

Table 3. Notation used in explaining MSM contacts.

E_{FM}	Fermi level of metal
E_{FS}	Fermi level of semiconductor
E_C	Energy of conduction band
E_V	Energy of valence band
E_0	Energy of vacuum
χ	Semiconductor electron affinity
Φ_m	Metal work function
Φ_s	Semiconductor work function
ϕ_n	Contact potential for electrons
ϕ_p	Contact potential for holes

When the thermal equilibrium is reached, the situation described in Figure 12 turns into a different picture where Fermi levels of both metal and semiconductor are equalized and contact potentials are formed. It is shown in Figure 13.a and Figure 13.b.

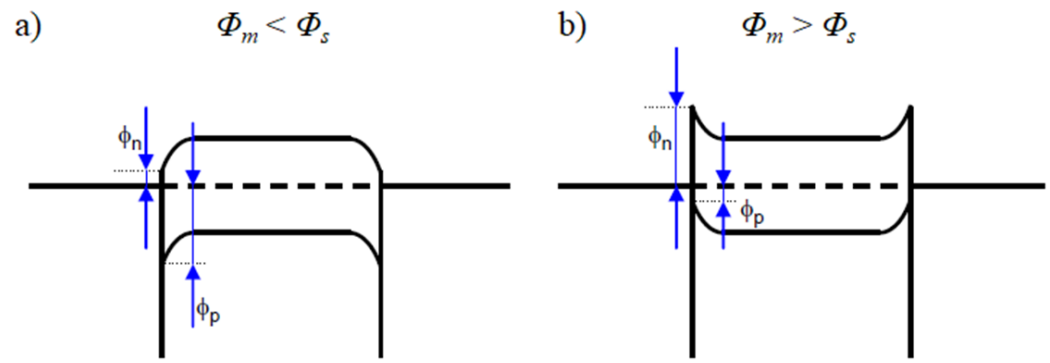

Figure 13. Band diagrams of a MSM structure after equilibrium has reached [41].

According to the notation given, for the $\Phi_m > \Phi_s$ case, contact potentials can be found by the following equations, Equation 2.37 and Equation 2.38:

$$\phi_n = \Phi_m - \chi \tag{2.37}$$

$$\phi_p = \chi + (E_c - E_v) - \Phi_m \tag{2.38}$$

The nature of the MSM system changes with the application of bias to the contacts. This change is most evident in the Fermi levels, where the contact with positive bias will have a lower Fermi level as opposed to the other contact with negative bias. There is also a difference between a high bias condition and low bias condition. These differences are illustrated on Figure 14, Figure 15, Figure 16 and Figure 17 for both cases of low and high bias. On these figures, the left-hand side contact is

depicted as cathode and the right-hand side contact is depicted as anode. To supplement the diagrams, it should be emphasized that on Figure 15 and Figure 17, blue points represent photoelectrons while red points represent photo holes, both of which emerge as a result of radiation interaction happening inside the semiconductor, which was depicted as a photo event with a green dot and arrow.

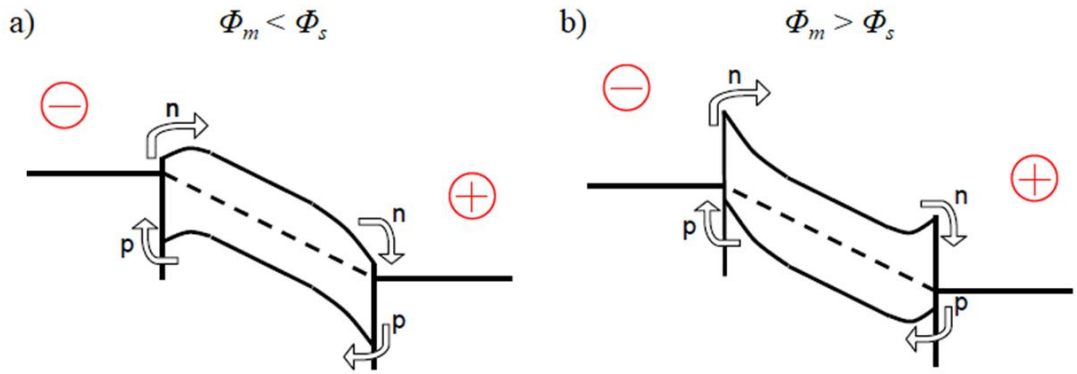

Figure 14. Band diagram of a MSM system when a low bias is applied [41].

For the $\Phi_m < \Phi_s$ case, as can be seen on Figure 14.a, the barrier formed at the cathode side limits the electron dark current entering from metal to the semiconductor. In a similar way, the hole dark current is limited at the anode side by a reverse biased Schottky barrier. On the other hand, Figure 14.b depicts the case of $\Phi_m < \Phi_s$ and here the electron dark current is limited because of the reverse biased Schottky barrier formed at the cathode side and the barrier formed at the anode limits the hole dark current. What decides the type of the dark current (electron or hole) is the relative height of these barriers formed at the opposite ends of the MSM system. When a photo event is included into this picture, Figure 15 can be referenced to understand the working of the system.

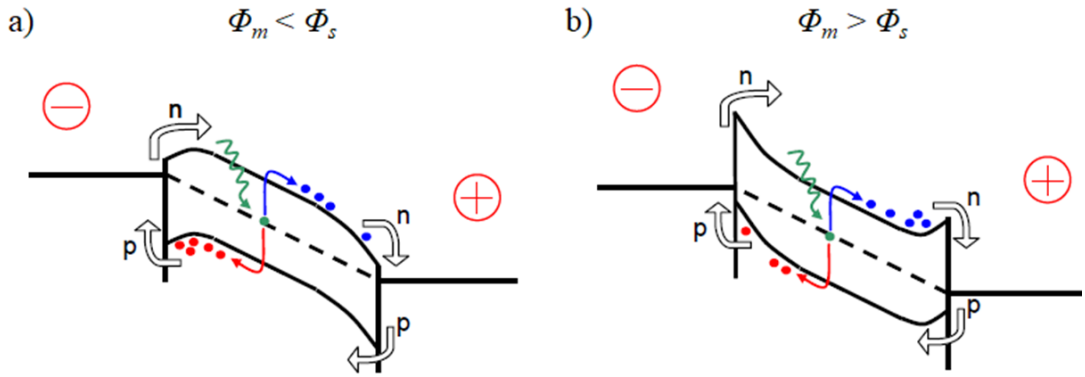

Figure 15. Band diagram of a MSM system showing the movements of photoelectrons and photo holes when a low bias is applied [41].

There exist numerous consequences one can draw from the inquiry illustrated on Figure 15. For the $\Phi_m < \Phi_s$ case (Figure 15.a), at the cathode holes will experience a voltage dependent barrier in order to transfer from the semiconductor to metal. On the opposite side, at the anode, electrons can be easily collected by the metal contact since they do not have to overcome a barrier. For the $\Phi_m > \Phi_s$ case (Figure 15.b), which is more relevant for this study, electrons at the anode will experience a barrier and may not be collected efficiently while the holes at cathode will not experience a barrier in front of them and can easily be collected. However, the barrier that impedes the electron flow at the anode will shorten with increased bias and this is one of the reasons that CZT devices usually work at high voltages to improve the detector performance. As it is shown in Figure 16 and also in Figure 17, some changes will occur and eventually cause the total depletion of the whole thickness of the semiconductor.

For the $\Phi_m < \Phi_s$ case (Figure 16.a), while there is a contact potential for electrons entering the semiconductor from metal at the cathode part, there is no barrier for the electrons collected from anode where electrons can move almost freely from semiconductor to metal. It can be said that, in this case, anode behaves as an Ohmic contact. Holes on the other hand, can be easily collected from the cathode without a barrier and will experience a voltage independent barrier while entering from metal to semiconductor at the anode.

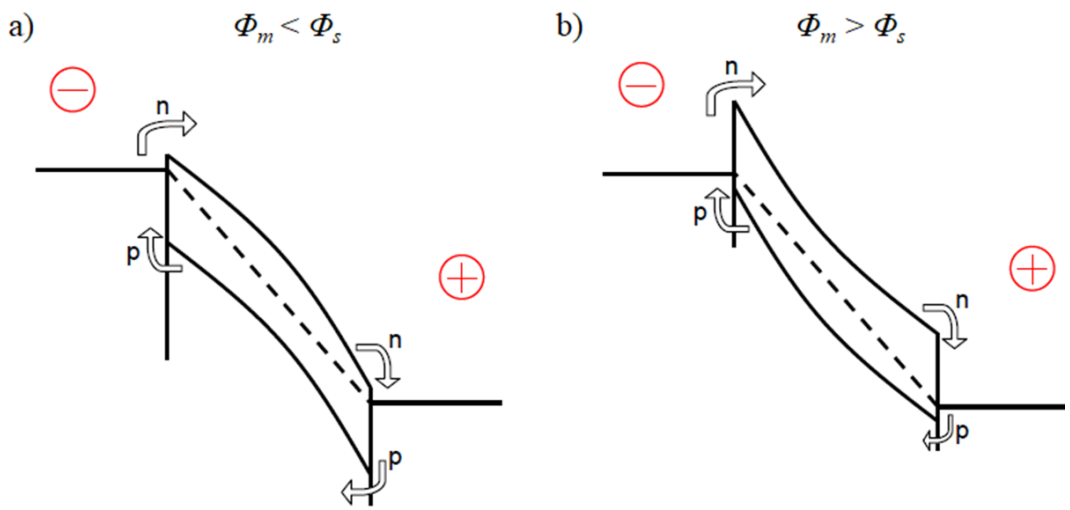

Figure 16. Band diagram of a MSM system when low bias is applied [41].

The more relevant $\Phi_m > \Phi_s$ case (Figure 16.b), can be analyzed where electrons have to overcome a voltage independent barrier ϕ_n while entering semiconductor from left, that is from cathode side. On the other hand, electrons exiting the semiconductor from the anode side, do not see any barrier in front of them. Thus, one can say that in this picture, anode behaves like an Ohmic contact and cathode behaves like reverse biased Schottky contact for electrons. On the contrary, holes can be freely collected from cathode since they do not face a barrier. While at the anode, holes do face a voltage independent barrier and as a result, entering semiconductor from metal side is difficult for them. Hence, it can be concluded that, anode behaves like a reverse biased Schottky contact and cathode behaves like an Ohmic contact for holes.

Interestingly, the limiting mechanism of dark current for the electrodes (anode and cathode) is equivalent. Both types of dark currents are limited by reverse biased Schottky contacts, dark electrons at cathode, dark holes at anode. It was mentioned that the type of the dark current is decided by the relative heights of these contact barriers. It can be emphasized that for a small work function metal ($\Phi_m < \Phi_s$) the dark current will be dominated by electrons entering from cathode and for a higher work function metal ($\Phi_m > \Phi_s$) the dark current will be dominated by holes entering from anode.

A similar analysis can be made for photoelectrons and photo holes generated inside the semiconductor by a photo event, as is shown in Figure 17.a and Figure 17.b.

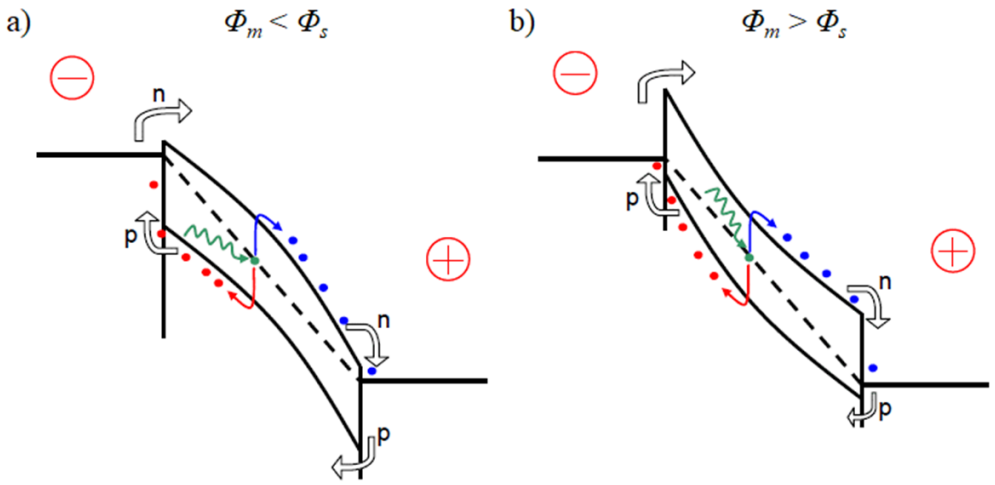

Figure 17. Band diagram of a MSM system showing the movements of photoelectrons and photo holes when high bias is applied [41].

At high bias, the photoelectrons and photo holes do not experience any barrier at the electrodes and both of them can easily be collected if there are no trapping issues involved.

To summarize, first it must be emphasized that as the applied bias to the contacts increases the collection efficiency of photoelectrons from anode also increases since the barrier experienced by these electrons at anode decreases. The anode becomes an Ohmic contact and detector efficiency increases. Related with high bias, photo holes can also be collected from cathode without experiencing an impeding barrier, therefore cathode also becomes an Ohmic contact. Secondly, both electron and hole dark currents are limited by a voltage independent Schottky barrier at cathode and anode respectively. Lastly, it should be kept in mind that the analysis presented here assumes an ideal MSM structure, but in reality, there are other factors like the surface state before any contact deposition, the level of contamination and the presence of any oxide layers between the metal contact and semiconductor surface. All these may affect the formation of contact barrier and its height.

2.6 Growth of CdZnTe Crystals

There exist several growth methods used in bulk CdZnTe crystal production. Among these, the conventional Bridgman, Vertical Gradient Freeze (VGF) and Travelling Heater Method (THM) can be listed [42], [43]. The Bridgman method is actually realized when Bridgman first wrote his paper on techniques of crystal growth and can be considered as the pioneering method [44]. In years, Bridgman method was diversified and new techniques were developed. These are, Horizontal and Vertical Bridgman, High Pressure Bridgman and Low Pressure Bridgman techniques [45]. Recently, Travelling Heater Method, is becoming more and more popular and promises larger single grain crystals with higher yields [46], [47]. METU CGL crystal growth system can be briefly defined as a multi zone Vertical Gradient Freeze furnace, which is fully operational. Temperature modeling studies on METU CGL system were conducted before this thesis study [7], [8], [48].

In order to produce fine quality single crystal CdZnTe ingots, optimization of growth parameters such as source material preparation, growth rate, cooling rate and thermal profiling are crucial. To achieve the highest control over these parameters, a VGF furnace system with 30 software regulated heating zones that are active over the thermal environment during the growth process was designed and produced by a US company called Mellen [8].

The specific ingots that were grown in CGL and used in this study were named as MT13 and MT20. Figure 18 and Figure 19 show pictures of these ingots respectively.

Among these ingots, MT13 is grown with 10% zinc concentration and no indium was doped. On the other hand, MT20 is doped with 10 ppm indium (In) during the growth process and same amount of zinc percentage was used as in MT13. The aim for the doping process was to investigate and control the electronic properties of CdZnTe material.

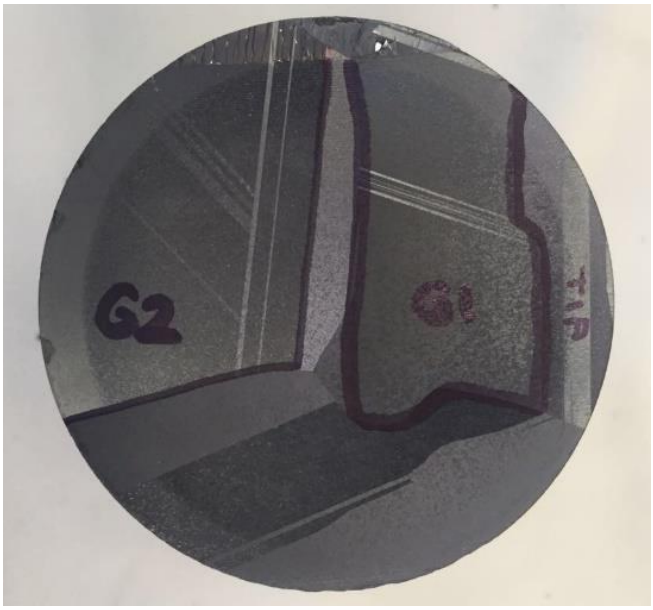

Figure 18. MT13 ingot view from top, grain boundaries and twin formations are visible.

Figure 19. MT20 ingot view from top with a ruler for size comparison.

Although it is reported that indium has an improving effect over the CZT material's electronic properties, especially increased resistivity [49], [50], details of this process are not disclosed in many of the studies and need to be understood for our future studies. However, considering the fact that one growth cycle and sample preparation usually takes more than a month time an extensive investigation of indium doping is time consuming and very costly. For this reason, only MT13 and MT20 samples have been studied in this work. Current-voltage plots of the samples were obtained to extract resistivity values for the samples produced. Corresponding results will be presented in Chapter 4.

CHAPTER 3

EXPERIMENTAL PROCEDURES

This chapter deals with several experimental techniques used in METU CGL for fabricating a CZT detector from the bulk of crystal. These techniques or fabrication steps can be summarized in a flowchart as seen on Figure 20. Some of these steps are indispensable like lapping or polishing and some of them can be ignored like chemical polishing. Figure 20 depicts the general fabrication overview applied to the detectors used in this study. The last process defines the characterization methods applied to the finished detector crystal.

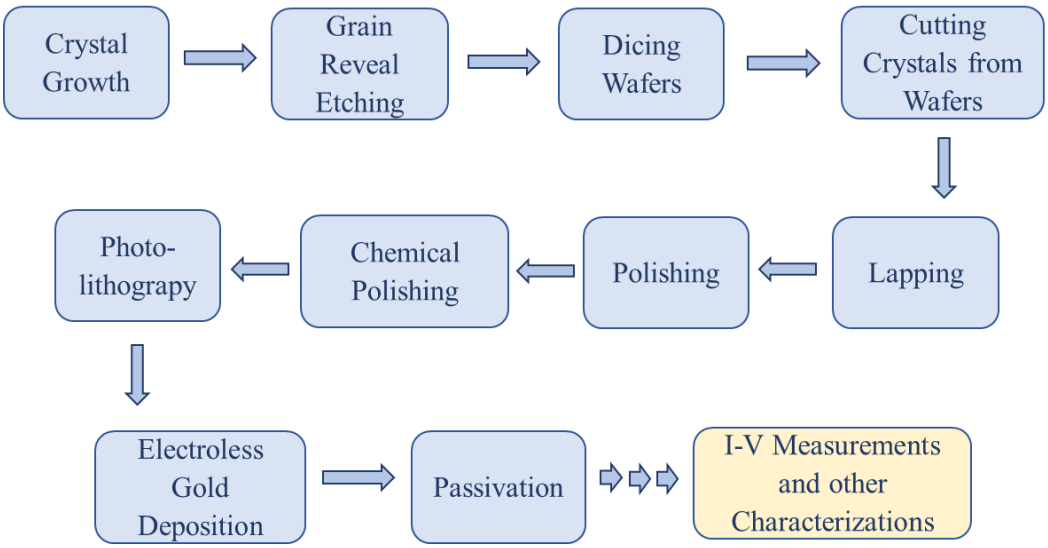

Figure 20. Flowchart of the fabrication process for CZT detectors at CGL.

Although not depicted, there are extensive cleaning processes between some steps shown in Figure 20.

Crystals used in this study were grown in Crystal Growth Laboratory located at METU Physics Department. The details about their growth processes were already given in previous chapter. There was also a commercial crystal that has been reprocessed for comparison purposes.

Grain reveal etching will not be explained here in detail since the process was already discussed in previous thesis studies conducted in METU CGL [7], [9], [10]. Briefly, after the growth process the ingot is extracted from the ampoule in which the grain boundaries and other growth specific formations like twins over the ingot are usually hard to be seen by naked eye. To increase the visibility, first a coarse grinding with a sand paper is applied. Then a more thorough chemical etching is applied. There are several etching types named as Inoue, Nakagawa and Everson. Since the etchants are dependent on the crystal orientation [7] in this study the suitable etching method was usually chosen as Saucedo etching for grain revealing. After the grain reveal etching, single crystal grains can be easily identified and more precise cutting procedures can be applied in order to obtain desired orientation and dimensions.

3.1 Dicing and Cutting

In order to dice the ingot and extract the detector crystals from the wafers, a Logitech Ltd model AWS1 wire saw machine is used. The diameter of the diamond covered wire is approximately 300 μm. In order to prevent crystal damage, a lubricant made from mono ethylene glycol is utilized during the cutting process. Figure 21, Figure 22 and Figure 23 show images related to a standard dicing and cutting procedure.

By using a mounting apparatus and carbon blocks for support, crystals are fixed with the help of a special temperature sensitive wax.

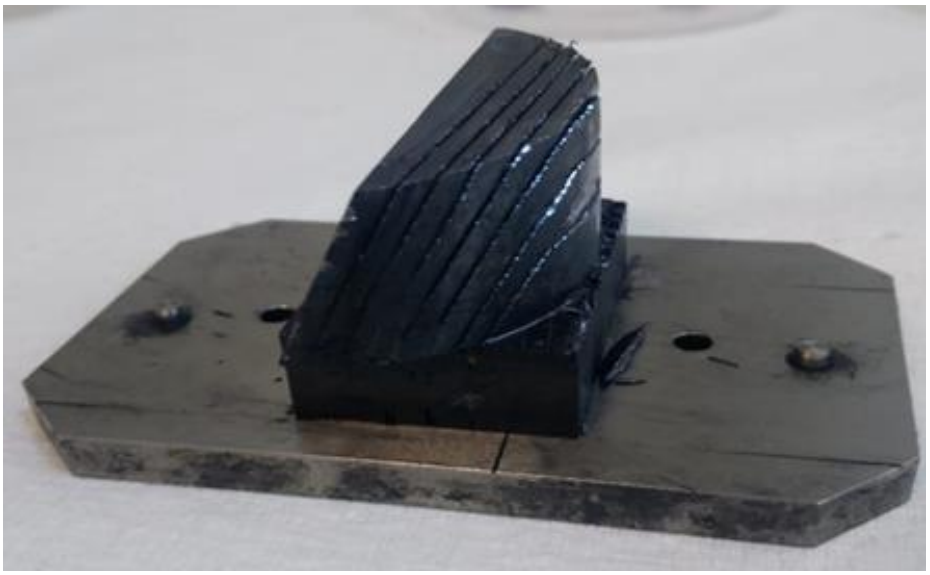

Figure 21. A crystal piece from an ingot being diced.

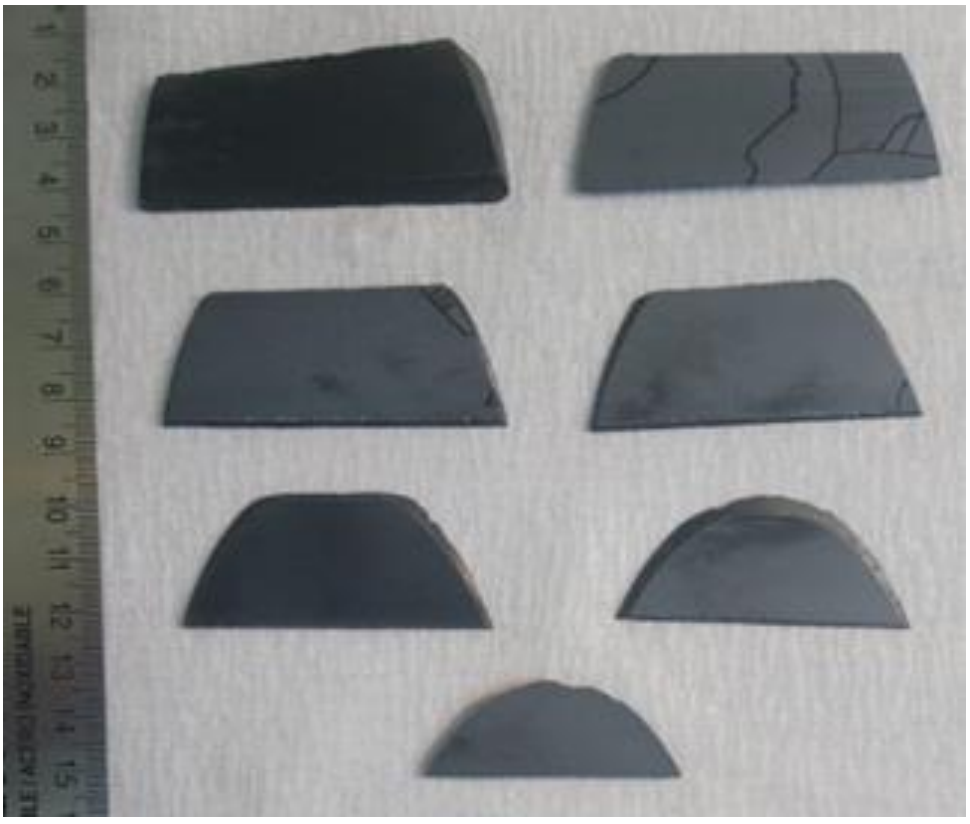

Figure 22. Sliced wafers from previous figure.

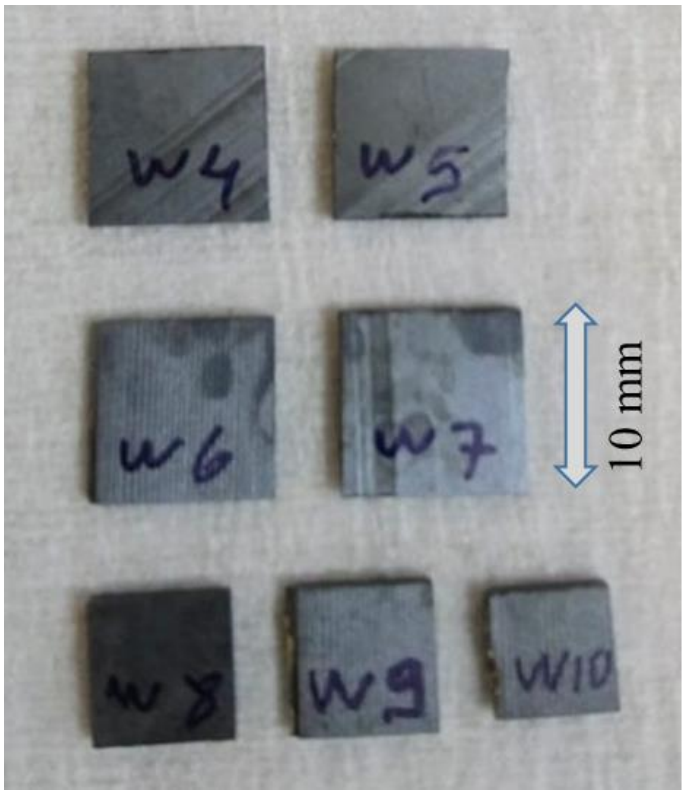

Figure 23. Slices were being cut in rectangular shapes for lapping and polishing.

3.2 Lapping and Polishing

Once cutting of the crystals is finished they are brought in clean room for lapping and polishing procedures. Both operations are done with a Logitech Ltd machine designed for this purpose, model name PM5 Precision Lapping & Polishing System. After dicing and cutting, the surface of the crystals is usually damaged and rugged, therefore, not suitable for any type of sensitive procedure such as pixel patterning or contact deposition. Although the working principles are the same for lapping and polishing, different sub-plates are used with combination of particular alumina (aluminum oxide) powders. Concentration level and size of the abrasive slurry containing alumina powders with plate rotation speed and applied pressure over the crystal sample are essential parameters affecting the quality of lapping and polishing procedures [10].

In the case of lapping, a glass covered metal plate is used with 15 µm, 9 µm and 3 µm calcined aluminum oxide powders (Al_2O_3), supplied by Logitech Ltd. On the

other hand, for polishing, a polishing cloth covered metal plate is used instead of a glass one in combination with 1 μm and 0.3 μm ultra-fine calcined aluminum oxide powders, supplied by Logitech Ltd. As the size grade of aluminum oxide powders decreases the level of surface damages also decreases [10].

The alumina powder slurries were prepared with deionized water at a 7.5% level of concentration and 15% level of concentration for lapping and polishing respectively.

The samples are glued on one side of a specially produced glass carrier plates with the help of temperature sensitive wax and then mounted into a jig which has a vacuum mechanism to safely hold the sample over the rotating metal plates. Figure 24 shows the glass carrier plate over which a sample is glued. For lapping, the glass covered plate is rotated at 20 rpm. For polishing, the polishing cloth covered plate is rotated at 40 rpm. The jig load is usually a changing parameter and it depends on the thickness of the crystal samples. Lapping and polishing processes continue until the crystal surfaces gain a mirror like appearance, free from scratches and defects that can be seen by naked eye. Usually, it took 5 to 10 minutes of lapping time to have desired surface appearance. Same is true for polishing. But it is always possible to spend more time in order to reach the desired result of surface appearance if there are unwanted cleavages or defects.

After polishing is finished, a cleaning process is applied to the samples. This process includes an ultrasonic cleaner. Polished samples are removed from glass plates and with the help of tweezers they are submerged first into acetone, then isopropanol and then deionized water, usually for 5 minutes each. These solutions are kept inside the water tank of the ultrasonic cleaner which is heated approximately up to 30 degrees centigrade. If needed the process can be repeated. The aim is to get rid of any wax and alumina powder residue.

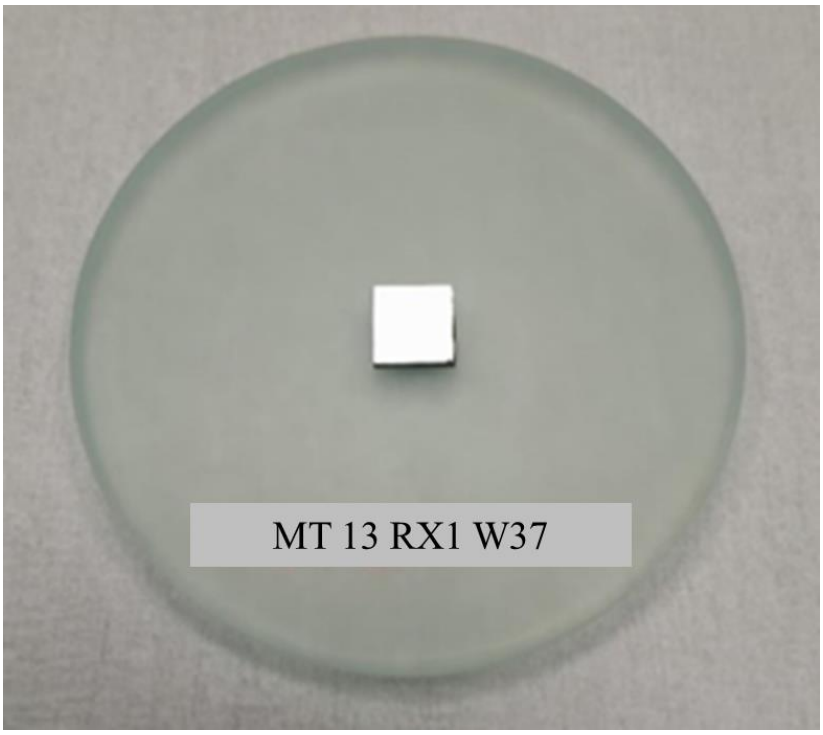

Figure 24. Glass carrier plate and a sample waxed on it.

3.3 Chemical Polishing

Chemical polishing can sometimes be called as chemo-mechanical polishing or chemical etching in the literature. The purpose of this process is to abolish any near surface damage that may be caused by mechanical lapping or mechanical polishing [51]. For this end, a bromine solution is prepared by mixing bromine with methanol. There are several studies in literature inspecting the optimum bromine concentration and treatment time for etching the surface of CdZnTe crystals [52]–[55].

Bromine tends to react more with cadmium as opposed to tellurium. The reason for that can be found in standard potentials (ΔE^0) of two reactions. The standard potential difference of a bromine-cadmium reaction is greater than a bromine-tellurium reaction. Therefore, when CdZnTe is treated with a Bromine-Methanol solution, a tellurium rich surface on the crystal appears [52], [56], [57]. Equation 3.1 and Equation 3.2 show the chemical formulation of two reactions [6].

$$2Br_2 + Te_{surface} \rightarrow 4Br^- + Te^{4+} \qquad \Delta E^0 = +0.50\,V \qquad (3.1)$$

$$Br_2 + Cd_{surface} \rightarrow 2Br^- + Cd^{2+} \qquad \Delta E^0 = +1.47\,V \qquad (3.2)$$

In this study, a preliminary research has also been conducted to determine the optimum concentration level of Bromine-Methanol solution. For this purpose, eight samples shown in Figure 25 from the MT13 ingot have been prepared and after lapping and polishing procedures they are treated with 1% Bromine-Methanol solution for different time intervals (30, 60, 90, 120 and 150 seconds).

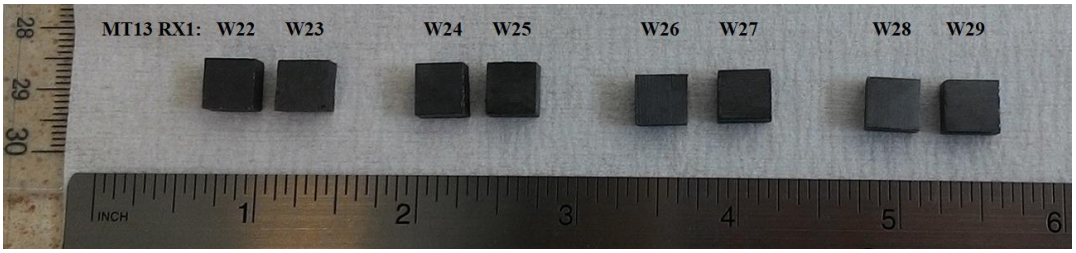

Figure 25. Eight samples from MT13 growth used for chemical etching optimization.

The samples were analyzed with X-ray photoelectron spectroscopy (XPS) and with other characterization methods like SEM and AFM. According to the results of this preliminary analysis [58], it was decided to treat the crystals with 1% Bromine-Methanol solution for 90 seconds, which appeared as an optimum time duration for etching CdZnTe crystals, as is shown in Figure 26. This figure represents the ratio of tellurium to the sum of cadmium and zinc in the crystal (Te/[Cd+Zn]) compared to the Bromine-Methanol etching time. In a stoichiometric crystal this ratio should be 1 but in the crystal that is examined it is 0.84 at the beginning (value of bulk bar in Figure 26) and changes with the etching duration.

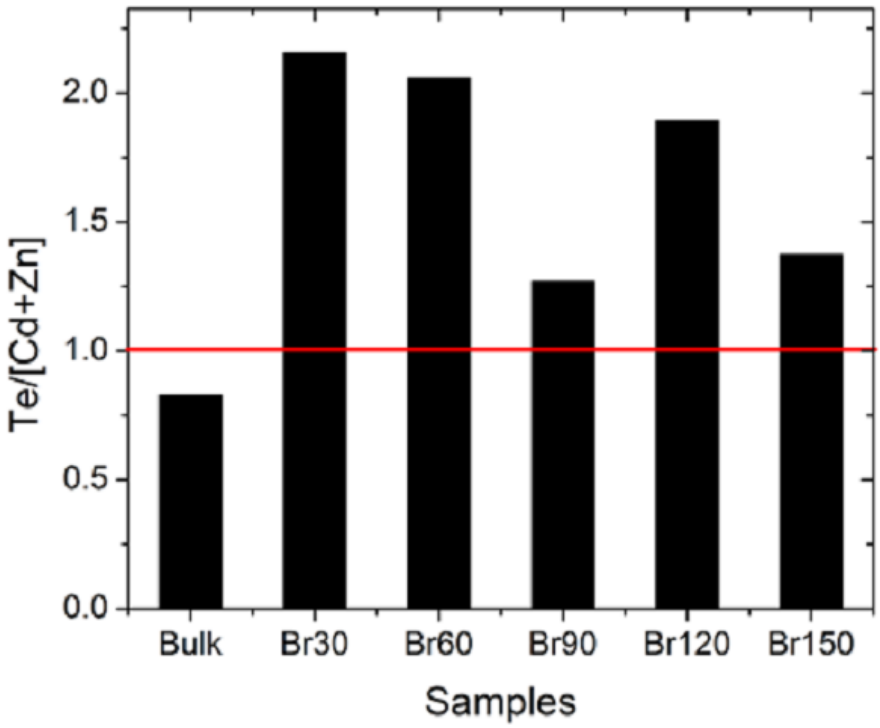

Figure 26. Te/[Cd+Zn] ratio depending on the etching duration [58].

Tellurium enrichment at the surface of the crystal is found to be clear for 30, 60 and 120 seconds of etching. The ratio of tellurium to cadmium + zinc is closest to 1 at 90 seconds of Bromine-Methanol etching, as given in Figure 26.

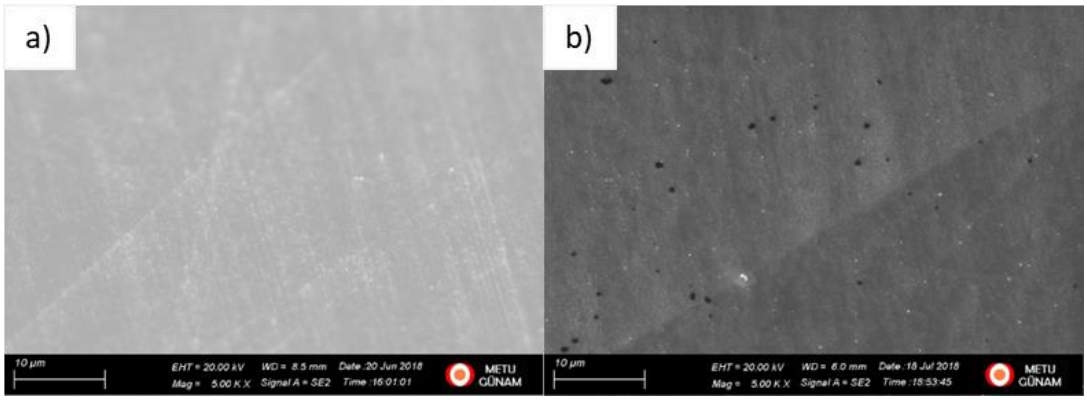

Figure 27. Sample MT13-RX1-W24 before (a) and after (b) etching.

Bromine-Methanol etching is done by dipping the samples into the solution with the help of tweezers and after it is finished, the samples were rinsed with methanol and immediately processed with photolithography application. On Figure 27, the difference between an etched surface (Figure 27.a) and non-etched surface (Figure 27.b) can be seen. White, shiny dots in Figure 27.b are alumina residue due to insufficient cleaning. The black dots on the other hand, are considered as tellurium inclusions which have origins in the morphological instabilities at the growth phase [42]. But the scratches dominating the polished surface before etching (Figure 27.a) are clearly diminished after etching.

3.4 Photolithography

This method can be defined as the process of electrode patterning on the surface of the detector crystal. The contact area where the electrodes are deposited can be patterned by the application of different photomasks and use of specific photoresists. Photomask is a plate that contains opaque regions where light cannot pass through and transparent regions where light can pass. These regions correspond to the desired contact pattern. Photoresists on the other hand are light sensitive chemicals and have two general types. When exposed to light, positive photoresists get weaker and after the development phase those regions exposed to light are removed. This is due to a solubility inhibitor agent inside the photoresist and it decomposes under light [6]. Negative photoresists on the other hand, get stronger when exposed to light and are insoluble when developed. The reason is that a photosensitive agent inside the photoresist initiates a cross linking polymer when exposed to light [59]. The general process of photolithography is shown in Figure 28.

In photoresist applications usually, UV light is used. However, other types of photolithography methods like X-ray photolithography is also available, especially in integrated circuit industry [61]. In this study, an UV light source (Ushio 1000W UV discharge lamp and OAI constant intensity controller as a lamp power supply) with a mask aligner (OAI model 500 mask aligner) were used for photolithography application.

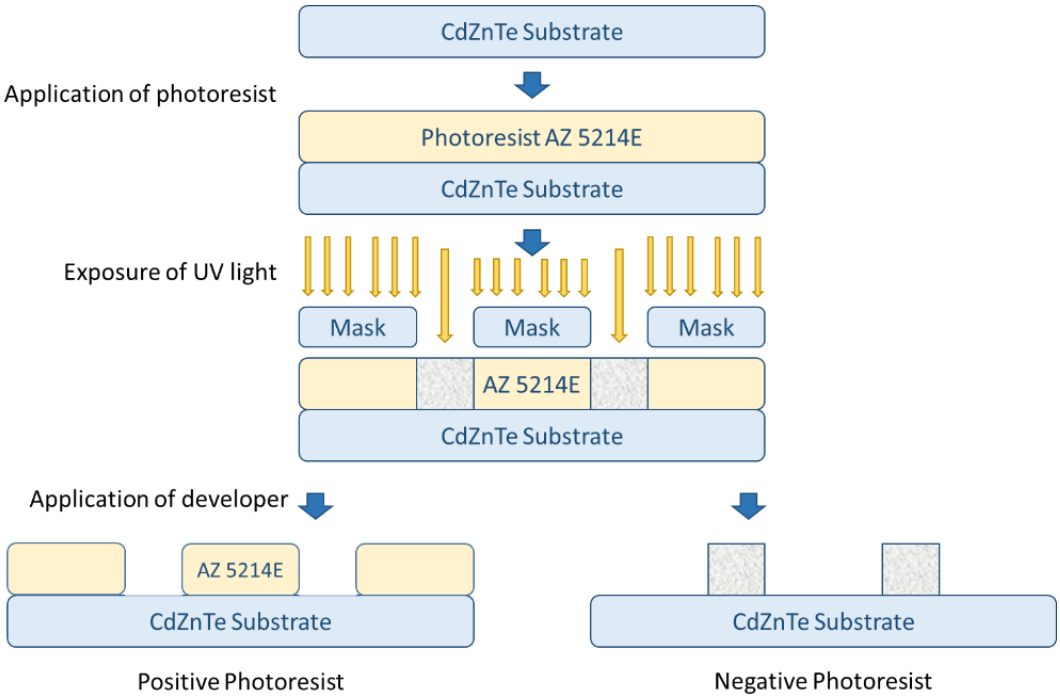

Figure 28. The general procedure of a photolithography application [60].

The photomask used was a dark field mask, designed in CGL and produced in METU - MEMS (Micro-Electro-Mechanical Systems Research and Application Center). Figure 29 shows the most used pixel pattern applied in this study and Figure 30 shows the dimensions of the pattern.

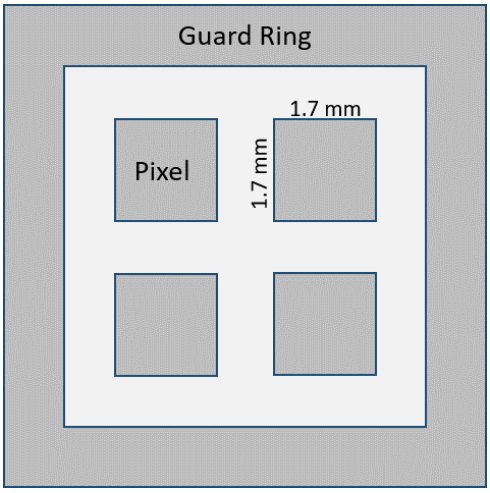

Figure 29. Pixel pattern that is mostly applied in photolithography in this study.

The guard ring and pixel areas in Figure 30 corresponds to the contact areas where gold is deposited. Pixel area is important for resistivity calculations.

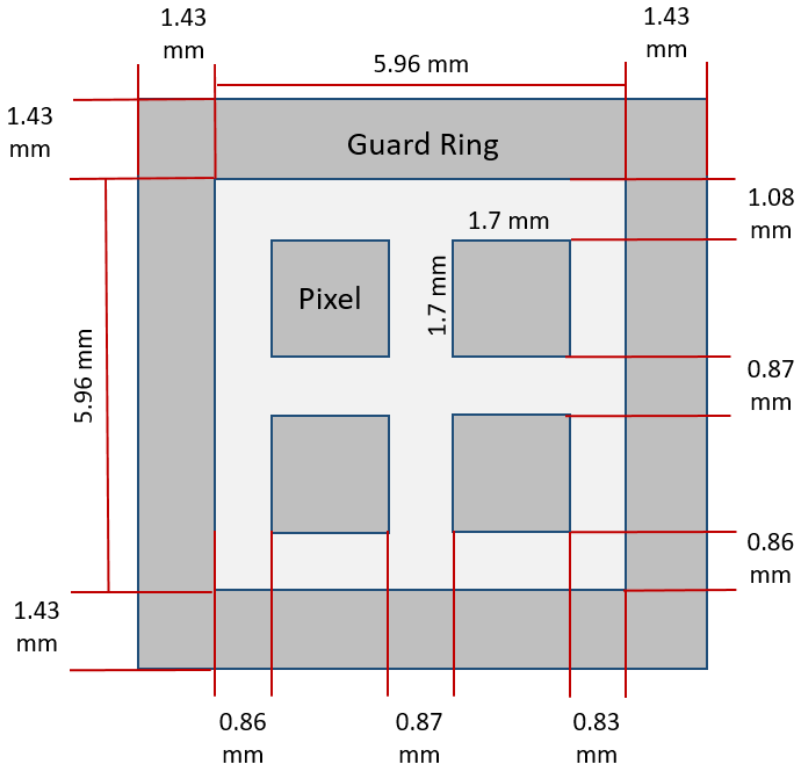

Figure 30. Dimensional data of the pixel pattern shown in previous figure.

After an investigation and application trials with various negative and positive photoresists, AZ 5214E was chosen. This is a positive photoresist with image reversal capability, meaning that it can also be used as a negative photoresist after applying a specific recipe. It is composed of a novolak resin and naphthoquinone diazide as photoactive compound [62]. The method used here can be considered as a combination of a positive photoresist and a dark field mask. In this method the photolithography is applied to the CdZnTe substrate before any contact deposition and immediately after Bromine-Methanol etching. The opaque regions of the mask correspond to the inter pixel areas of the pattern and the transparent regions correspond to pixels and the guard ring. So, when exposed to light those parts of the CdZnTe substrate under the opaque regions will be insoluble and those parts under the transparent regions will be soluble in the development stage. In this way, the

inter pixel areas will be protected from contact deposition and only the pixel regions will be open for deposition. Figure 31 shows a CdZnTe crystal after the photolithography procedure is finished. For the development stage, AZ 351B was used as a developer agent [59].

Figure 31. Crystal named MT13-RX1-W39 after photolithography is finished.

On Figure 31, dark gray areas are the inter pixel areas that are protected by the photoresist and light gray areas are the guard ring and pixels where metal is deposited. When developing is also finished the samples are cleaned by only deionized water. Since the application of alcohol or acetone can be detrimental for the photoresist material over the crystal.

3.5 Electroless Contact Deposition and Passivation

After photolithography, final stages in detector crystal fabrication are electroless gold deposition and passivation. Although there are other methods of contact deposition, such as thermal evaporation and sputtering, electroless deposition was chosen as the contact deposition method for this study. The reason behind this choice was that electroless deposition, as opposed to other techniques, is time efficient and results with better contacts [11], [12], [63]. The contacts made with electroless deposition are creating chemical bonds between the semiconductor and the metal with more strength. In addition, this method minimizes the oxide formation that appears between the metal-semiconductor interface [12], [64]. Since electroless plating is done with solutions involving spontaneous reactions, without

the use of any electrical power supply it is the easiest way of contact deposition and it can also be reproduced very easily [65].

The solution needed for electroless gold deposition is a gold chloride solution ($AuCl_3$) and it was prepared at CGL. First, a solution called “aqua regia” was prepared. The name comes from Latin, meaning “king’s water” or “royal water”. The chemical name is nitric acid hydrochloride. It has a strong ability to dissolve gold and can be very harmful to human health. The details about aqua regia and chemical processes of gold with it can be found in various sources [66]–[68]. In CGL, a pure gold piece about 1 grams of weight was dipped into aqua regia to form a gold chloride solution. Figure 32 shows the chloroauric acid solution used in CGL.

Figure 32. Electroless deposition in action for samples named as MT13-RX1-W34 and MT13-RX1-W35.

An important study on the contact characterization of CdZnTe radiation detectors has found that, electroless gold deposition gives best results at lower temperatures in terms of leakage current [6]. Therefore, when electroless deposition was applied the temperature of the solution was decreased around 0°C by surrounding the container with ice cubes for at least 30 minutes. Figure 33 shows the high voltage and low voltage IV measurements respectively, from the study mentioned above [6]. The figure depicts that at lower temperatures the leakage current decreases substantially.

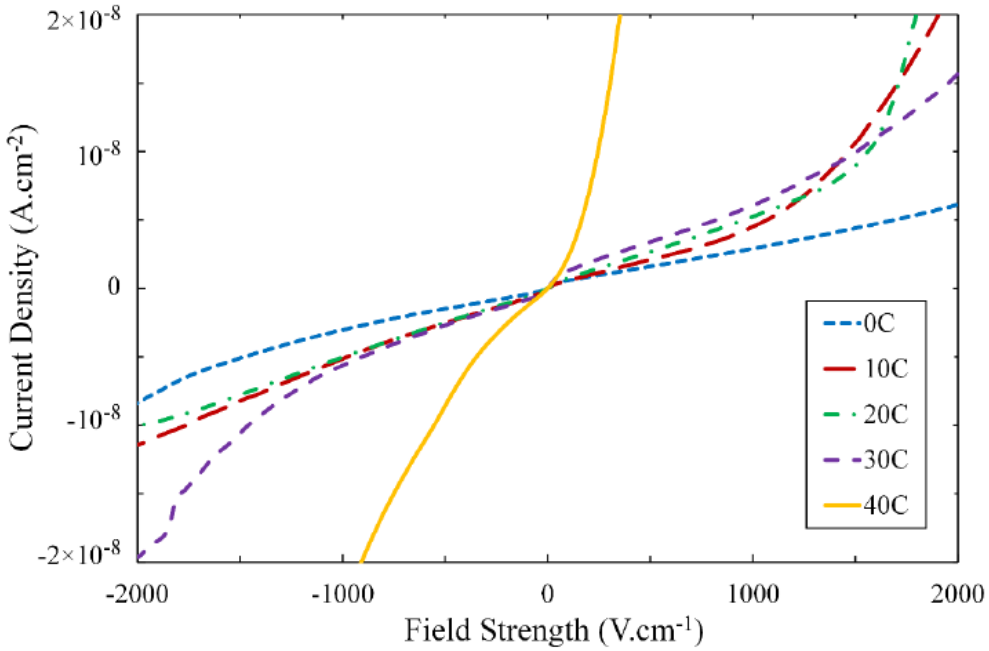

Figure 33. High voltage IV plots for 0-40°C electroless gold deposition [6].

The time of deposition is also important for the quality of the gold contacts. Equation 3.8 and Equation 3.9 [13] show what happens when a CdZnTe crystal is dipped into the aqueous solution of $AuCl_4^-$. According to these equations gold (Au) reacts with cadmium (Cd) more as opposed to tellurium (Te) since the difference of standard potentials is in favor of cadmium. The reaction of gold with zinc (Zn) can be neglected because of the low concentration of zinc in a $Cd_{0.9}Zn_{0.1}Te$ crystal. Preference of cadmium over tellurium causes a rejection of cadmium ions (Cd^{2+}) and formation of tellurium in the solution. However, with a longer deposition time less cadmium remains at the surface. Hence, the amount of deposited gold decreases and causes a tellurium rich surface, ready to react with oxidant ions and form a layer of tellurium oxide (TeO_2) [11]. It was concluded that short intervals of deposition time will be enough for the scope of this thesis study. But this feature is open to study for optimization.

$$2AuCL_4^- + 3Cd_{surface} \rightarrow 2Au_{surface} + 8Cl^- + 3Cd^{2+}$$
$$\Delta E^0 = +1.40\,V \quad (3.8)$$

$$4AuCL_4^- + 3Te_{surface} \rightarrow 4Au_{surface} + 16Cl^- + 3Te^{4+}$$
$$\Delta E^0 = +0.43\,V \quad (3.9)$$

Figure 34 shows two samples, one with deposition time of 3 hours and another with deposition time of 3 minutes.

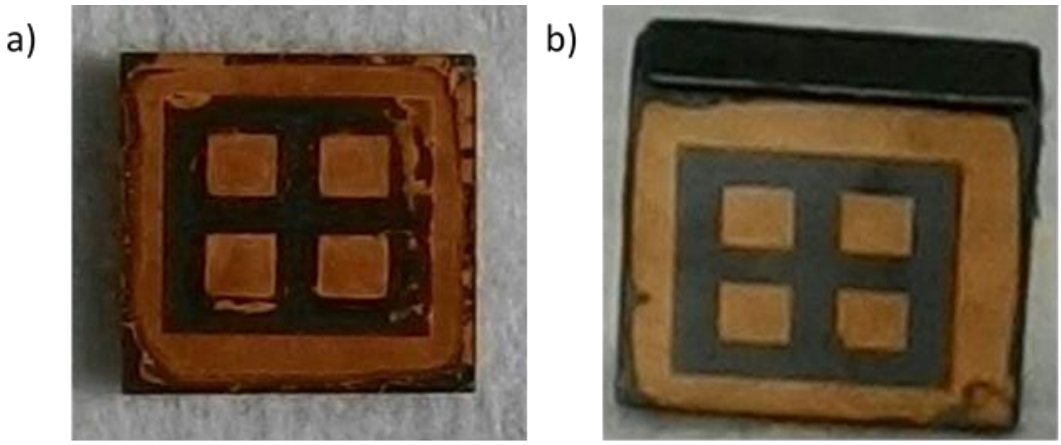

Figure 34. a) MT13-RX1-W35 deposition time 3 hours, b) MT13-RX1-W38 deposition time 3 minutes.

After the deposition procedure, samples are rinsed with deionized water for a short period of time like 10 seconds and then passivation is applied to the samples. For this end, 30% of hydrogen peroxide (H_2O_2) solution is prepared and samples are dipped into it for 3 minutes. The aim of the passivation is to limit the leakage currents to be active on detector surface [16].

3.6 Structural and Surface Characterization Methods

In order to understand the structural and surface conditions of the samples that are produced, several analysis methods were used. The following pages contain brief explanations of these methods.

3.6.1 Structural Analysis with XRD

X-ray diffraction (XRD) is a useful technique to analyze the structure of the crystals. It is based on measuring the transmission of monochromatic X-rays through the sample. As a result, a diffraction pattern is formed by constructive and destructive interference of X-rays with a wavelength which is comparable to the atomic distances. With the help of Bragg's Law, the diffraction pattern can be defined by the atomic spacing d of the sample material and also by the wavelength λ and angle θ of the X-rays [6]. Equation 3.10 and Figure 35 give the schematic and definition of Bragg's law respectively, where n is an integer number defining the diffraction spot.

$$2dsin\theta = n\lambda \tag{3.10}$$

By XRD analysis, one can determine the orientation of the sample crystals. The preferred orientation for CdZnTe crystals during the growth is usually <111> [69]. One reason for that is the superiority of <111> direction against other orientations at the growth phase and as a result having higher yields of crystal [70]. Moreover, detectors fabricated on <111> surfaces exhibit relatively good performance although there are also studies indicating no influential differences between the <111> and <115> orientations [71]. For these reasons, crystals with surface orientation <111> have been used throughout this study.

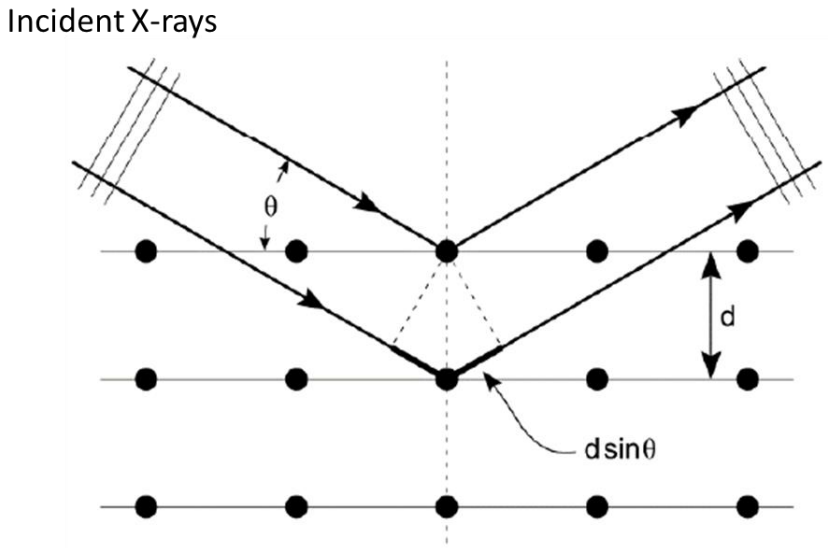

Figure 35. Schematic of Bragg's law [6].

3.6.2 Surface Analysis by AFM and SEM

The aim of the Atomic Force Microscopy (AFM) is to analyze the surface topography of the crystal samples. AFM technique is based on the force between the sample surface and the tip that scans the surface. During the scanning, local forces occur between the tip and sample surface, in the form of either attraction or repulsion. These forces cause a deflection in the cantilever which is attached to a rigid substrate that can be held fixed. The basic idea is to catch this level of deflection, with the help of a laser beam, and turn it into an electric signal that can be presented as topographic images. In this process, a small change in the cantilever deflection may produce a large deflection in the reflected spot position. When this happens, the angle of the reflected laser beam changes and the spot hits on a different part (usually called quadrants) of a photodetector. Figure 36 shows the simple mechanism of an atomic force microscopy. The deflection signal is calculated from the feedback of the signals coming from four quadrants [72]. The AFM system used in this study was NanoMagnetics Instruments Ambient AFM.

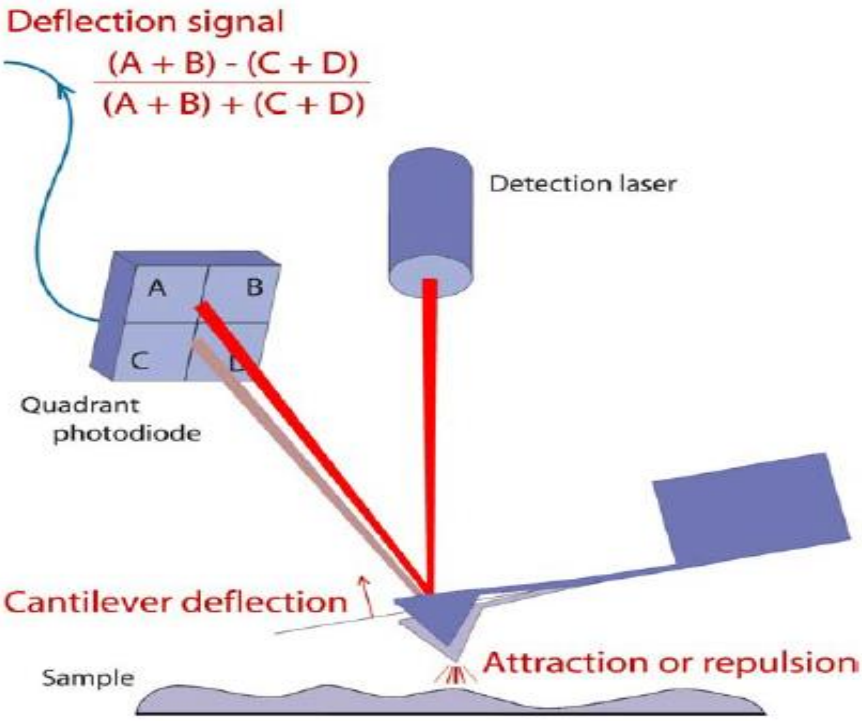

Figure 36. Simple working mechanism of an AFM device [72].

Scanning Electron Microscopy (SEM) has been used to monitor the surface morphology of the CdZnTe crystal and the Au electrode. SEM systems are powerful and well-known systems used for imaging and chemical composition analysis (with EDS) purposes. A short description of a SEM equipment can be as follows: with the help of an electron gun, electrons are accelerated and gain high kinetic energies. When these incident electrons hit the solid sample, they dissipate and loose energy in the form of various signals. These signals can be secondary electrons, backscattered electrons, diffracted backscattered electrons, photons in the form of characteristic X-rays, Auger electrons and heat. To produce images from the samples, secondary electrons (for morphology and topography) and backscattered electrons (for illustrating contrasts in composition) are used [73].

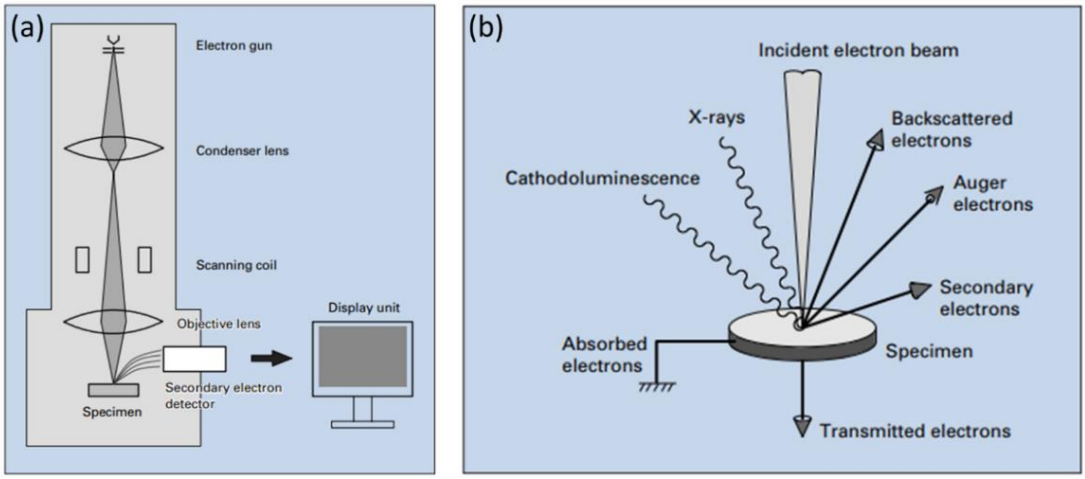

Figure 37. Simple working mechanism of a SEM system [74].

Figure 37 shows the simple mechanism of a Scanning Electron Microscopy device: at Figure 37.a) the general schematic of a SEM system is showed with electron gun, condenser lens, scanning coil and objective lens; at Figure 37.b) various types of electrons that appear when incident beam interacts with specimen have been illustrated.

3.7 Current-Voltage Measurements Setup

A fundamental method to determine the electronic response of a semiconductor detector is to measure the current flow passing through the detector as a function of applied voltage. This is called current-voltage measurement and it is primarily done for resistivity calculations and leakage current specification. For resistivity, usually low voltage regime is used. The linear fit of the I-V plot around zero voltage [14] helps to find the slope of the curve and the inverse of this slope gives the resistance value of the detector sample at hand. From Ohm's law, the resistivity ρ of the sample is then found with the relation shown in Equation 3.11 [75].

$$\rho = R\frac{A}{L} \tag{3.11}$$

Here, $R = dV/dI$ and A is the contact area of the pixel in [cm^2], L is the thickness of the sample in [cm] and R is the resistance in [Ohm] coming from the linear I-V plot. For current-voltage measurements a simple measurement method is used which is given in Figure 38.

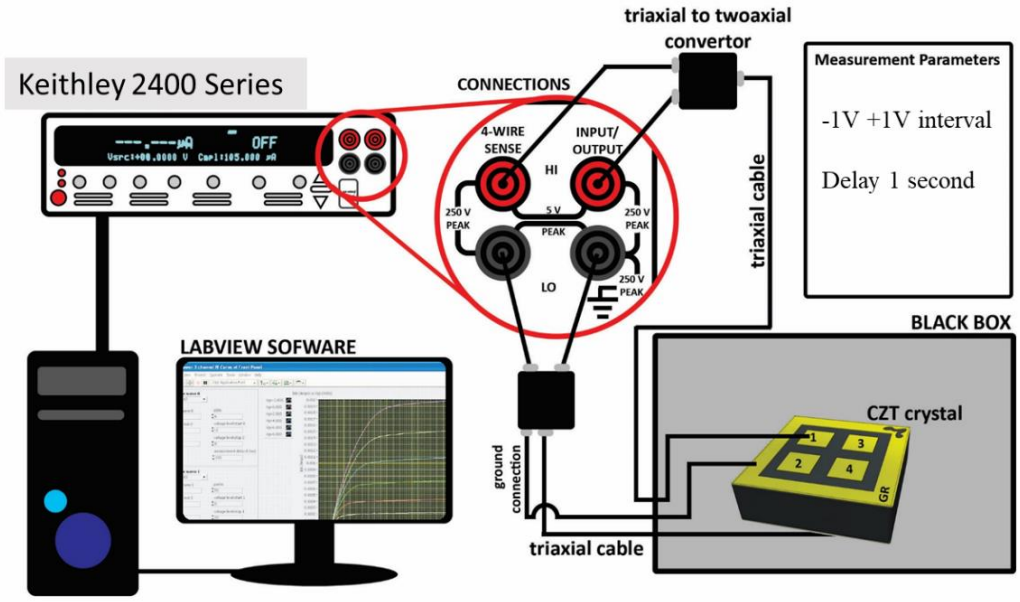

Figure 38. I-V setup used for current-voltage measurement.

As a source measurement unit, Keithley 2400 series measurement device was used. To make connection between the probes and the measurement device, triaxial cables were utilized. During I-V measurements, samples were placed inside a metal box in which no light is permitted to enter in order to fully realize the dark room conditions. One second of delay time was applied between each reading of the current value and the voltage range was between -1V and +1V. One tip of the probe is wired to the cathode side while the other probe is wired to the pixel that is under inspection. A third probe which does not have a triaxial cable was also wired to the guard ring section of the samples. During the measurement 3 pixels remain untouched by the any probe and cannot be grounded.

CHAPTER 4

RESULTS AND DISCUSSION

4.1 Structural Characterization: Results of the XRD Measurements

In Figure 39, a typical XRD spectrum taken from the sample which was used during this study is presented as a fine representative of <111> orientation of CdZnTe crystals. It clearly shows that the sample has the desired orientation.

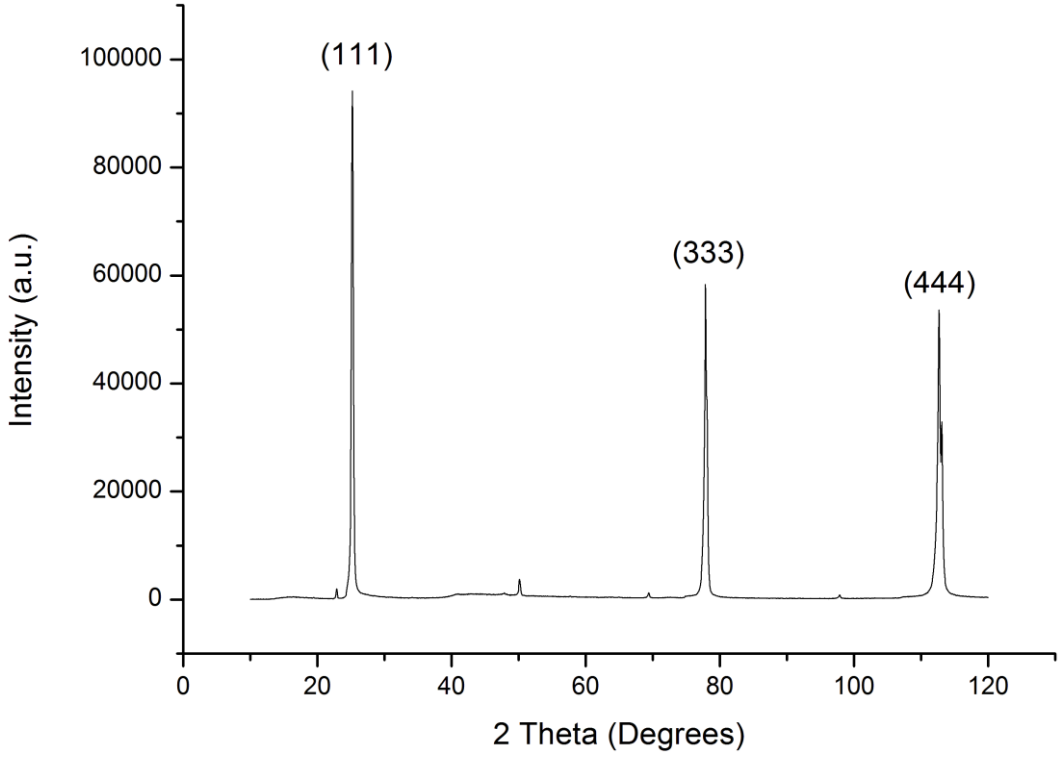

Figure 39. XRD measurement of MT18 RX1 W1.

The XRD results belonging to samples from different ingots (MT13, MT20 and commercial) are presented in Figure 40, Figure 41 and Figure 42 respectively. Note

that the sample from MT13 exhibits clear and strong peaks from the <111> plane while other samples have generated noisy signal (MT20 and commercial). The size of the samples (thickness and surface dimensions) plays a critical role here. Usually, thinner samples with greater surface area give better XRD plots. In primary XRD measurements (Figure 41 and Figure 42), MT20 and the commercial sample suffered from some noise. Their intensity values are also low compared with XRD plots of MT13. Same samples were analyzed with another XRD device, in order to be sure about the orientation. These second measurement plots were presented in Figure 43 and Figure 44 for MT20 and commercial samples. They show that these samples are clearly have <111> orientation. Depending on the zinc concentration, some shifts from ideal XRD characteristics of CdZnTe crystals were observed in all of the samples. But the peak values in XRD measurements were clear and it was possible to determine the orientations of the crystals.

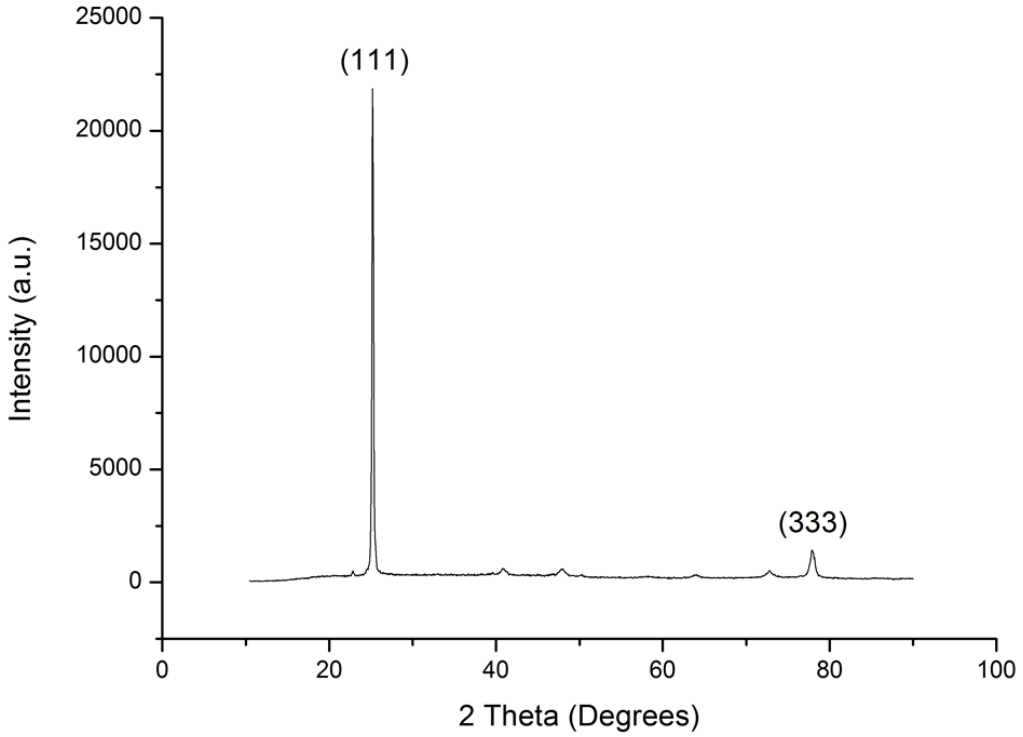

Figure 40. XRD measurement of MT13 RX2 W6.

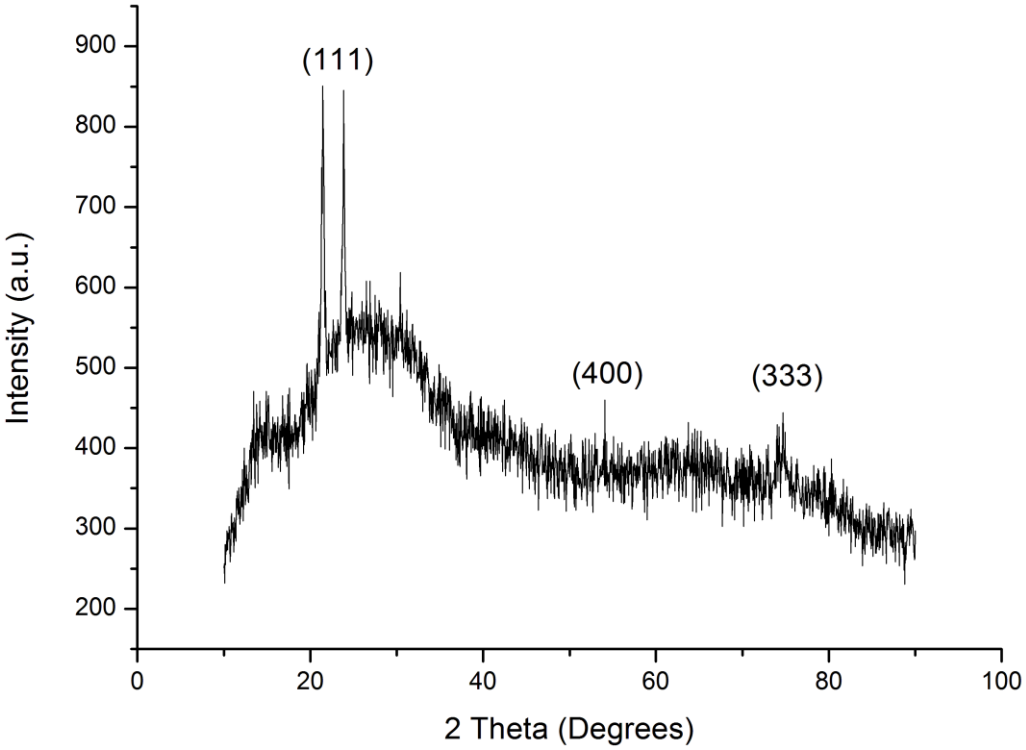

Figure 41. XRD measurement of MT20 RY1 W1.

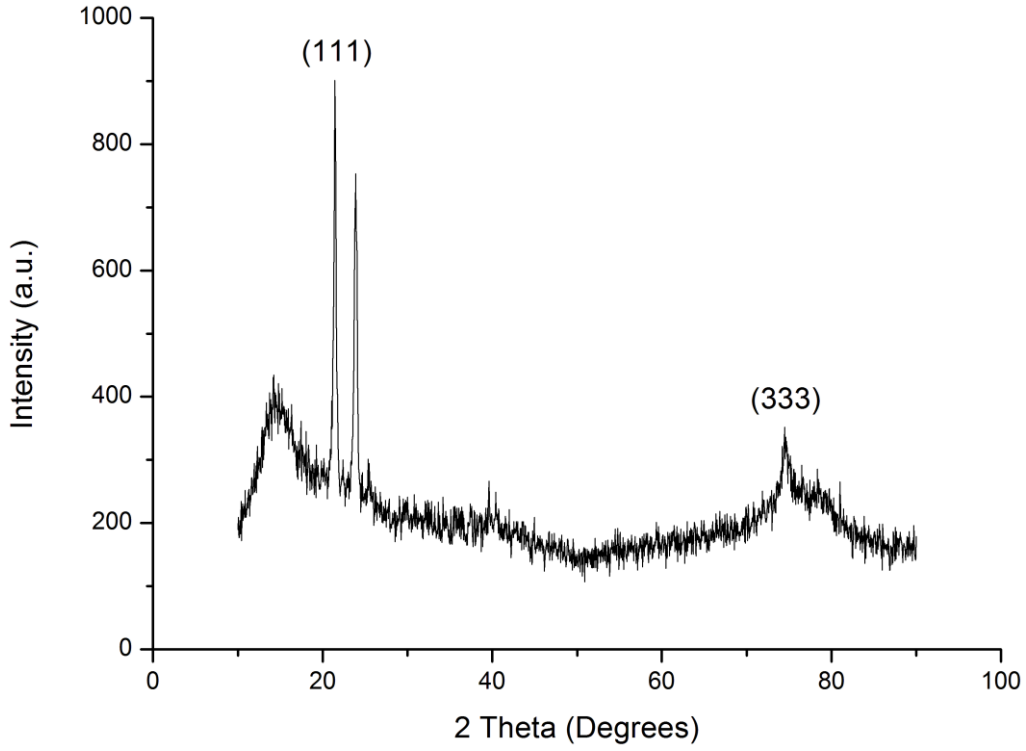

Figure 42. XRD measurement of commercial sample.

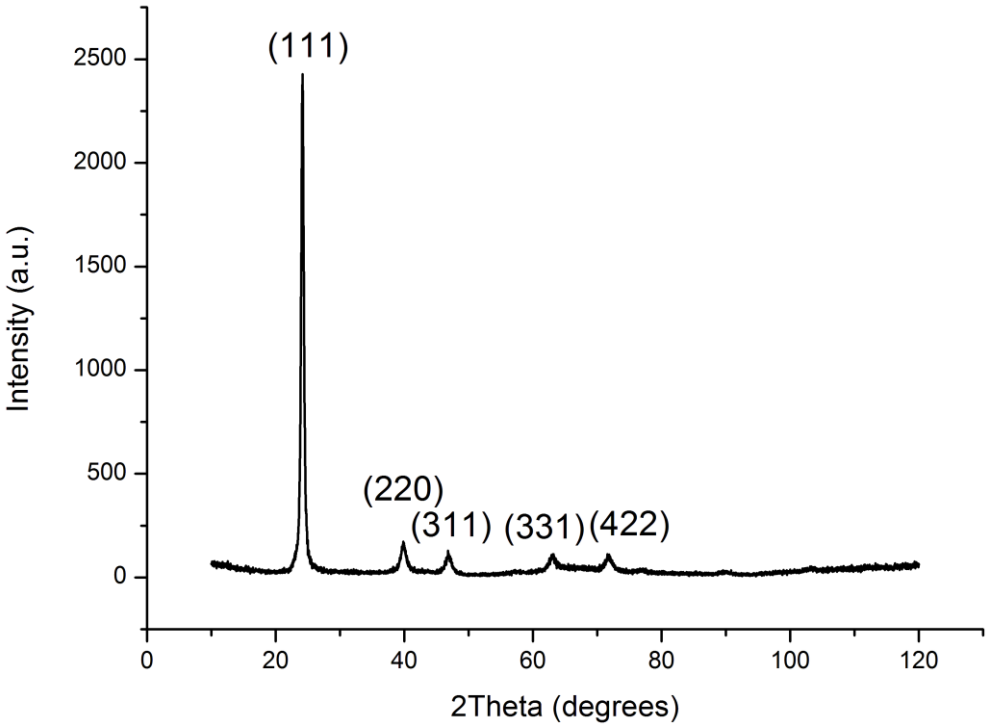

Figure 43. Second XRD measurement of MT20 RY1 W1 sample.

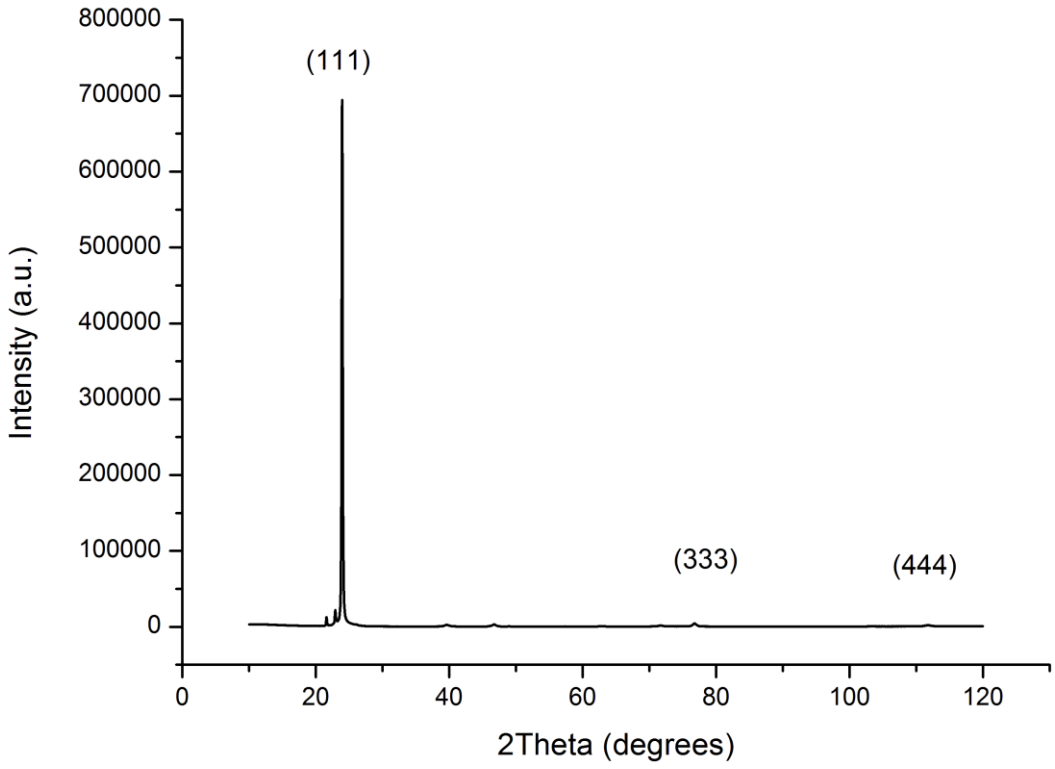

Figure 44. Second XRD measurement of the commercial sample.

4.2 Surface Characterization: Results of the AFM and SEM Measurements

The gold contacts that were deposited on sample crystals were analyzed with atomic force microscopy. Figure 45 shows the AFM image of one of the sample's contact area which is gold deposited with electroless gold deposition method. The lines on the figure with numbers are the positions where surface profiles were measured and average surface thickness variation was calculated between the gold contact and bare surface of CZT. It has been found that the thickness of the gold contact is around 120 nm as can be seen on Figure 46. It is known that, this value is a saturation limit for electroless gold contacts on CdZnTe [11].

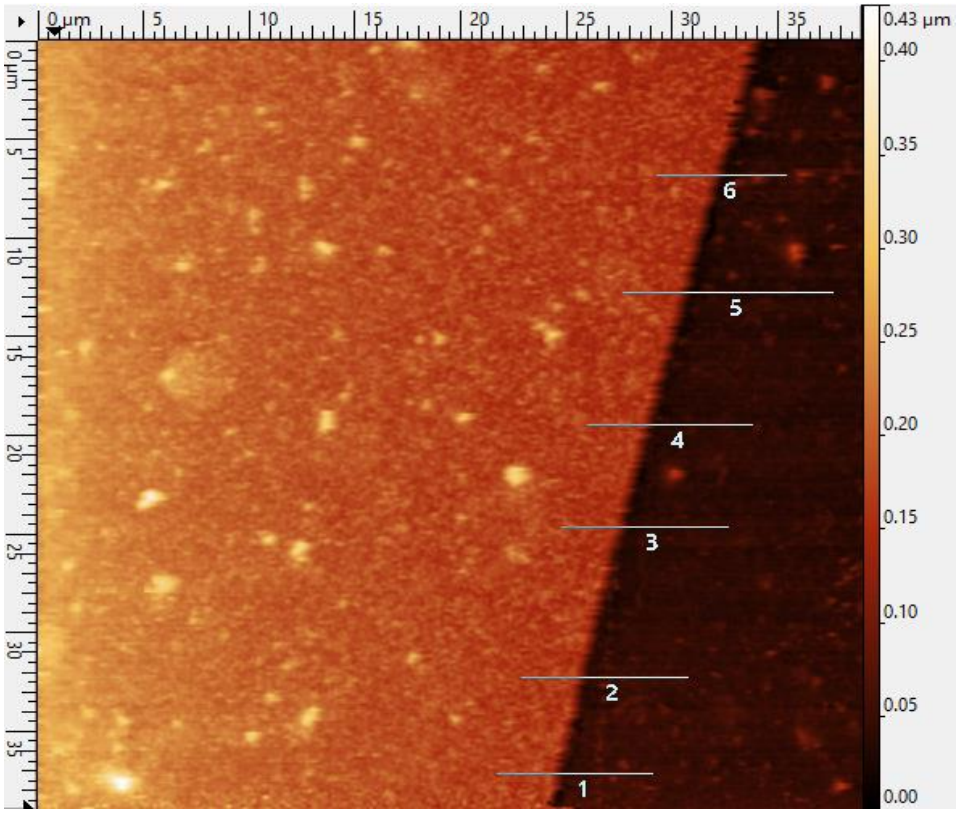

Figure 45. Positions of the profiles from where the average thickness was calculated. Shiny area is the gold contact deposited and the dark area is CZT surface.

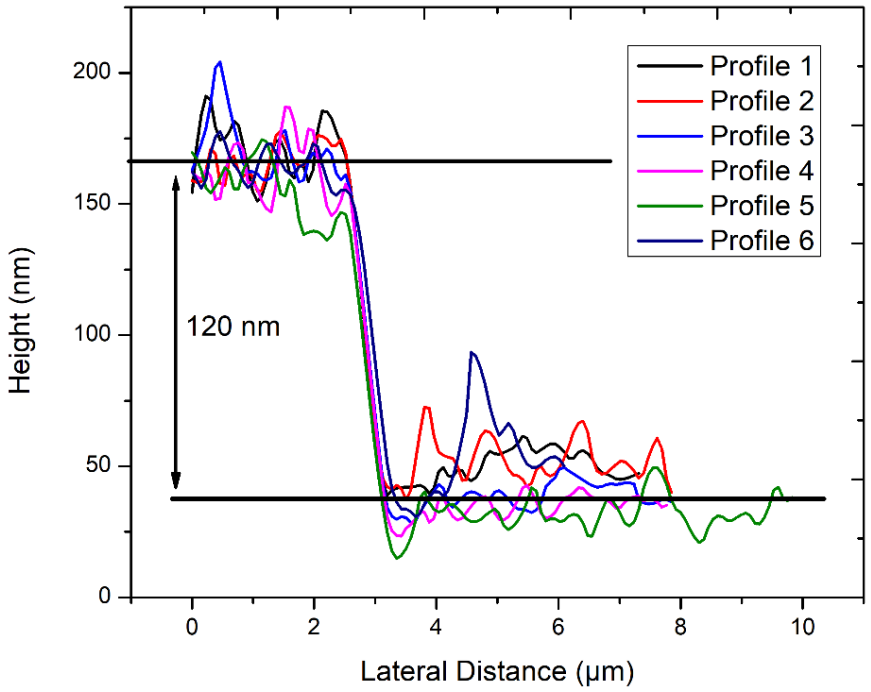

Figure 46. Average thickness of the gold contact on CdZnTe sample crystal.

Figure 47 and Figure 48 show SEM images of a sample with gold (Au) contact which is partly detached from the surface. It is quite surprising that the thickness of the gold layer has reached 964 nm which is well above the saturation limit reported in literature [11]. This aspect of the metal deposition by electroless technique needs to be investigated for a clarification.

The detachment of the metal shown in Figure 48 is a problem that other studies have also experienced, especially with platinum electrodes [11]. This adhesion problem is believed to result from bad surface condition and can be overcome by a proper surface preparation and cleaning process.

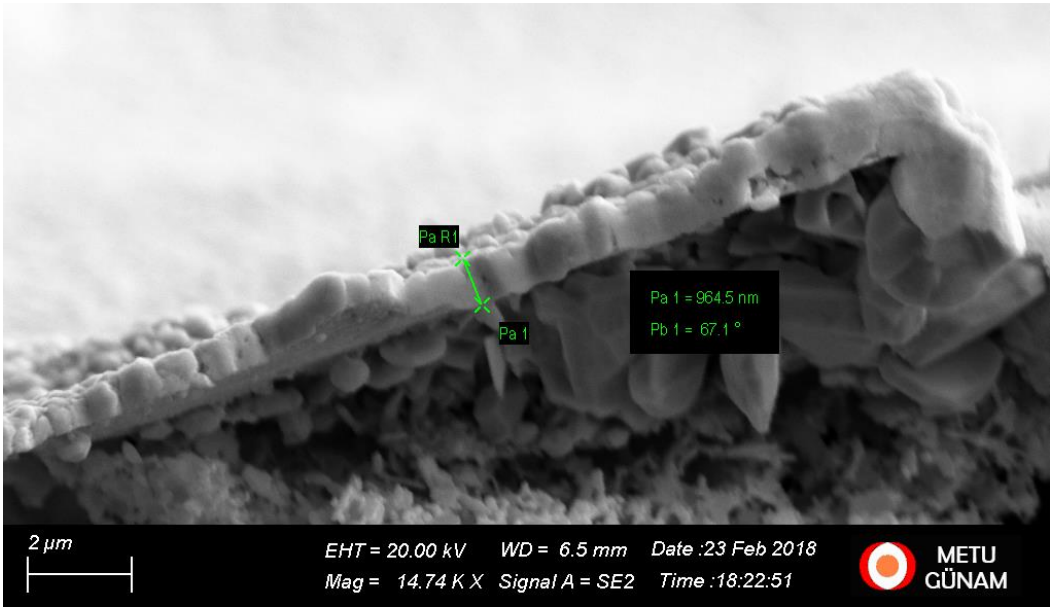

Figure 47. SEM image of a gold contact with thickness of 964.5 nm.

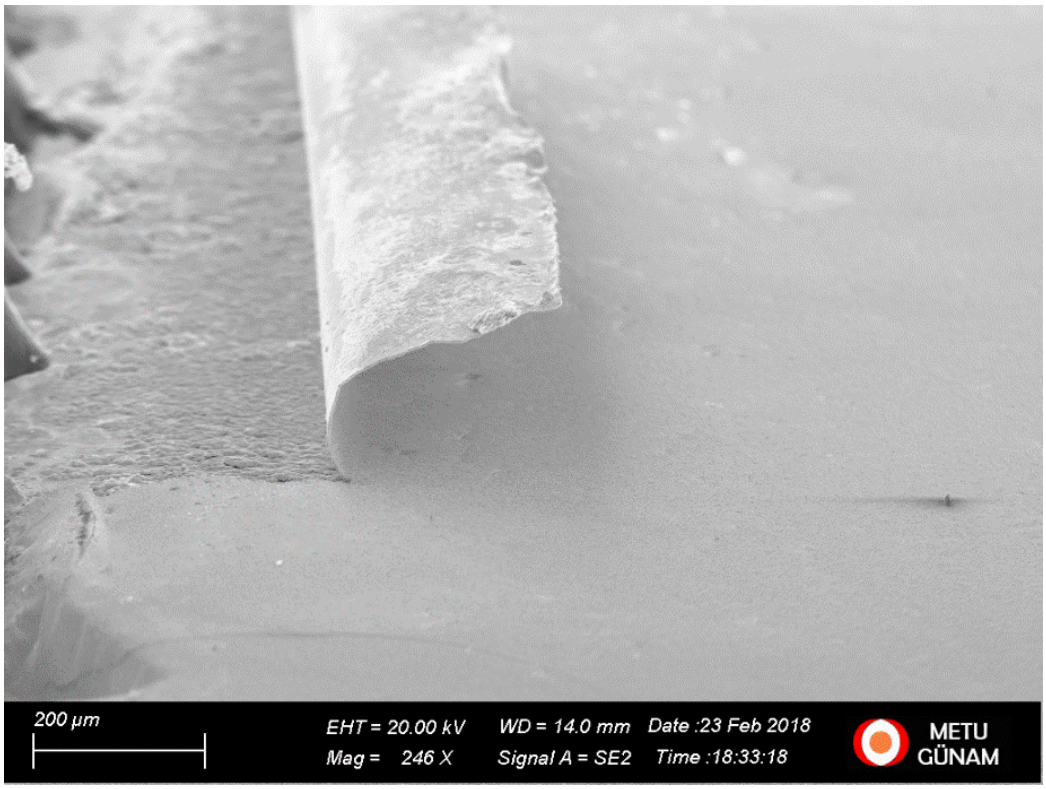

Figure 48. SEM image of a gold contact on the sample MT13 RX1 W35 fabricated. Part of a layer curled away from the CZT.

4.3 Compositional Characterization: Results of the EDS and SIMS Analyses

In addition to SEM and AFM analyses, to understand the compositional structure, EDS (Energy Dispersive X-Ray Spectroscopy) and SIMS (Secondary Ion Mass Spectroscopy) investigations were also conducted. The aim of these was to characterize the indium (In) composition in the MT20 ingot. EDS analysis was a preliminary account whether the ingot contains indium. To make certain of the indium distribution, SIMS analysis was conducted which is a more sensitive surface analysis technique. In both cases, it was found that the MT20 ingot has indium inside it. The commercial sample was also investigated with both analysis techniques. The results are presented in the following pages.

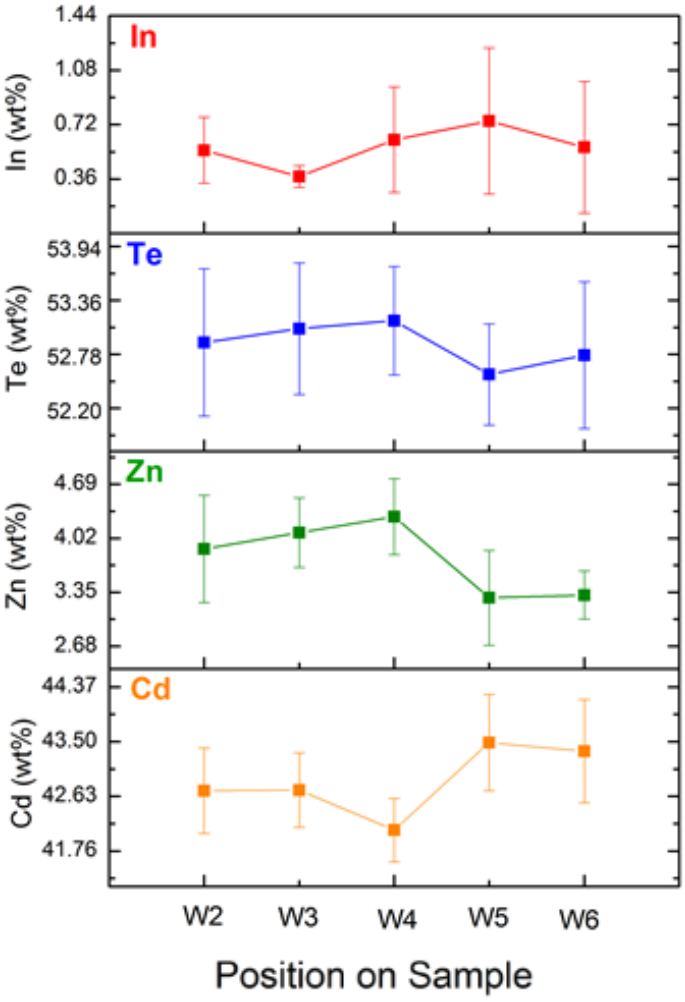

Figure 49. EDS analysis of MT20 ingot.

Figure 49 shows the EDS analysis of the MT20 ingot as a whole. The positions W2, W3, W4, W5 and W6 correspond to the different parts of the ingot along the growth axis. By looking to the weight percentages, it can be said that the whole ingot contains indium element with different amounts changing between 0.72% to 0.36% in weight.

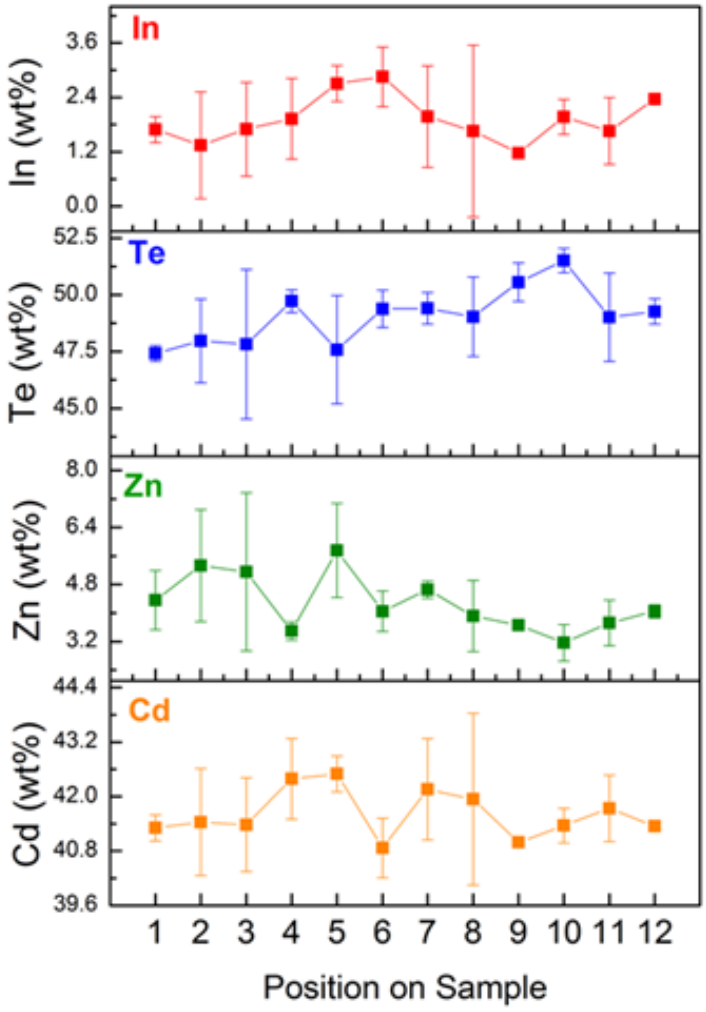

Figure 50. EDS analysis of the commercial sample.

Figure 50 on the other hand is an EDS analysis conducted for the commercial sample. This sample was a 20 mm x 20 mm sample in surface dimensions and the position values on the figure correspond to different points on this surface area.

In addition to EDS analysis, Secondary Ion Mass Spectroscopy (SIMS) was also applied for compositional analysis. In this method, the samples were not just analyzed from the surface as in the case of EDS. Indium can be searched from the layers deeper than the surface. Because of this, the results of SIMS data are more reliable than EDS data, in terms of compositional analysis of indium inside the ingot. Results are shown in the following figures.

In Figure 51, the composition of three main elements constituting MT20 ingot is shown. In Figure 52, the indium composition in the same ingot is presented. And in Figure 53, the comparison of indium concentration between the MT20 ingot and the commercial sample is depicted. It is valuable to mention that the concentration of indium is one order below in the commercial sample than the MT20 ingot. Finally, in Figure 54, the comparison of MT20 and commercial sample is given in terms of main constituent elements, which are cadmium, zinc and telluride.

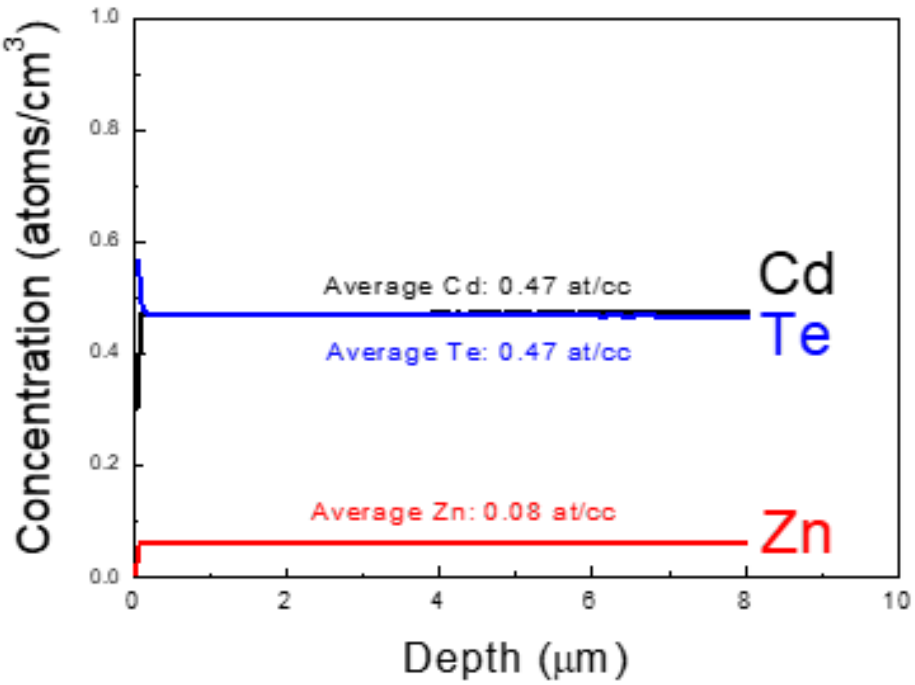

Figure 51. SIMS data of MT20 ingot.

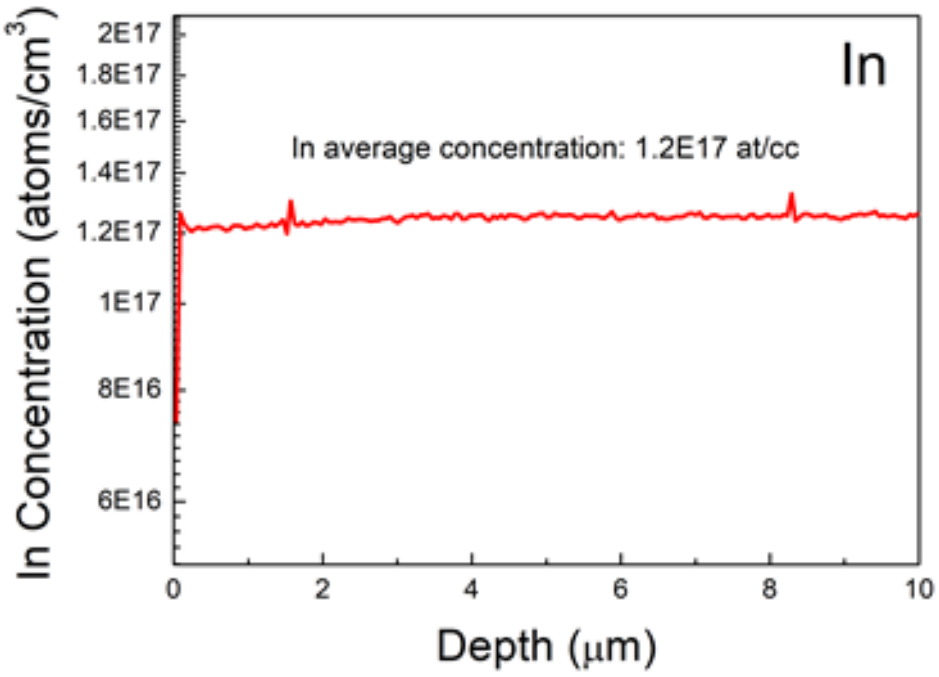

Figure 52. Indium composition in MT20 ingot.

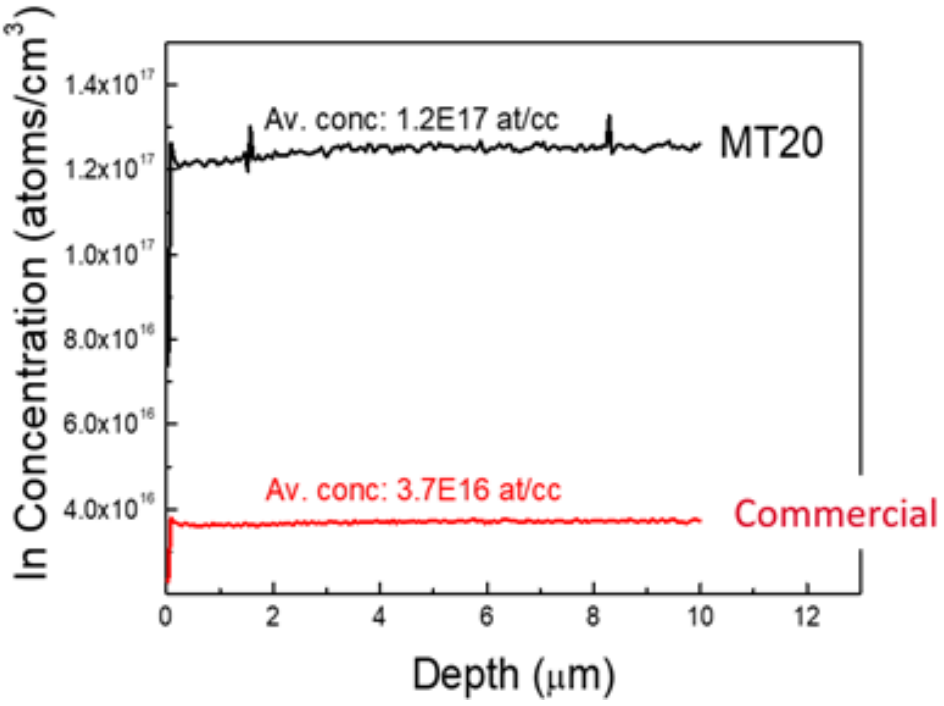

Figure 53. Comparison of indium composition between MT20 and the commercial sample.

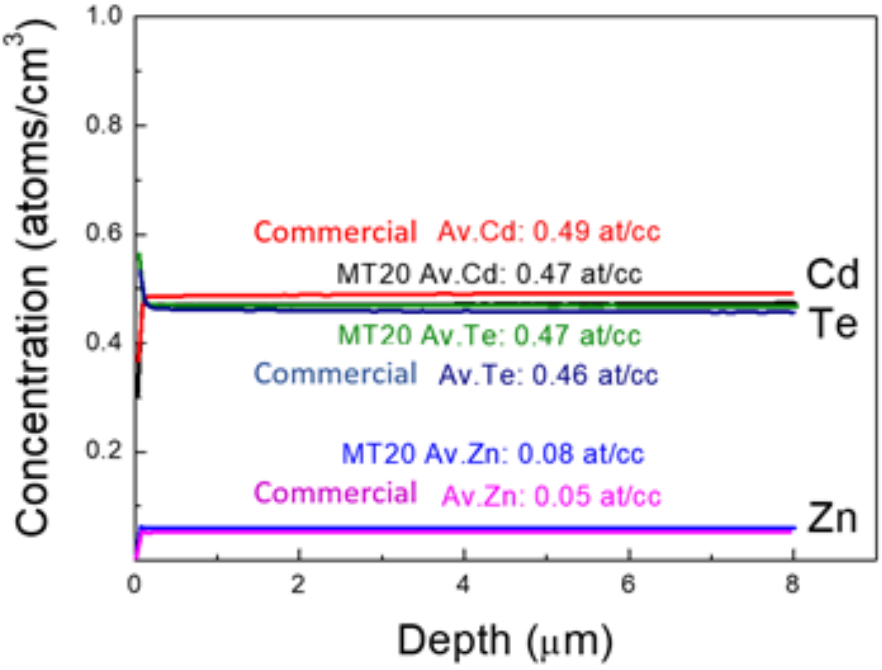

Figure 54. Comparison of MT20 and commercial sample in terms of main constituent elements.

4.4 Electronic Characterization: Results of the I-V Measurements

As mentioned previously, current-voltage (I-V) measurements are crucial when exploring the electronic properties of CdZnTe crystals. With mobility-lifetime product, resistivity of the crystal, which is calculated from the slope of I-V curve at around V = 0 [14], is one of the key parameters in determining the electronic response of the detector. In this section, results of current voltage measurements done throughout this study and resistivity values extracted from them are presented. The dimensional properties of the crystal samples used in I-V measurements are given in Table 4.

Table 4. Dimensional properties of the crystal samples used in I-V measurements.

Sample Name	Width (mm)	Length (mm)	Thickness (μm)
MT13 RX1 W37	8.73	8.67	3141.1
MT13 RX2 W6	7.34	9.03	1798.2
MT20 RY1 W1	10.25	9.73	1817.5
Commercial 2.2.2	9.24	9.05	2068.0

4.4.1 Current Voltage Measurements of MT13

Most of the crystal samples fabricated in this study were cut out from the ingot named as MT13. It should be mentioned that this is an undoped ingot. In this growth, 6N materials were used as ingredients and the zinc concentration was 10%. The crystals were usually from the parts of the ingot that are close to the heel region, that is the last to freeze parts. It is known that the zinc distribution along the ingot is not uniform and some studies found that it decreases from the center to the periphery [50], [76]. The crystals from MT13 were close to the end of the ingot and were neither on the periphery nor on the center. This may explain the low resistivity values encountered with the samples from this growth. Since there is a strong correlation between the zinc distribution and resistivity, especially the outer parts of the ingots exhibit highest resistivity [76], [77].

One of the relatively early samples from MT13 gave resistivity in the order of 10^4 Ω cm. Figure 55 shows the I-V plot of this sample and the calculated resistivity. Here the resistivity is calculated from the linear fit which is taken around V = 0, giving resistivity value of 3.4 x 10^4 Ω cm. In Figure 55, this area of the fitting is emphasized with the red rectangular shape.

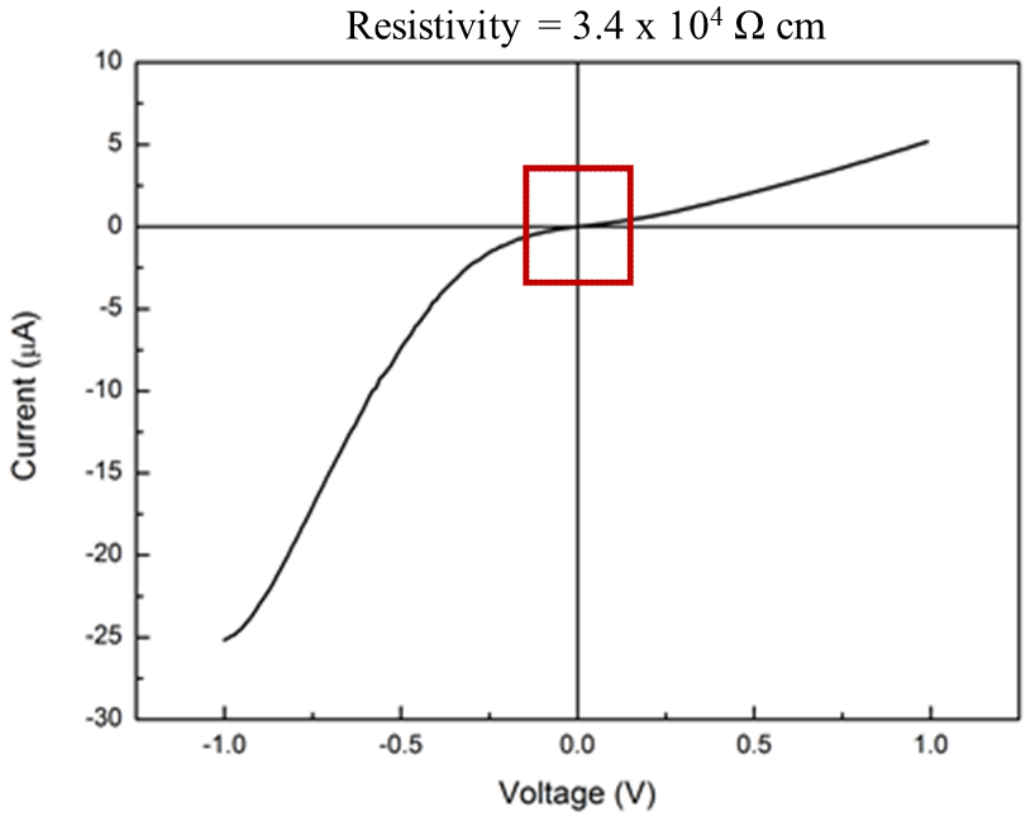

Figure 55. I-V plot and resistivity of sample MT13 RX1 W37.

The other sample, closer to the tip of the ingot, gave similar results. Figure 56 shows the representative I-V plot for this group of samples from MT13. The RX2 wafer is closer to the middle of the ingot and the resistivity shows no sign of drastic change. The highest resistivity value obtained for this group did not exceed the order of 10^4 Ω cm. The acceptable resistivity values for a radiation detector have not been reached for the samples from MT13 growth. Since this ingot was not doped during the growth process, it is not expected to show very high resistivity because of cadmium (Cd) vacancies boosting the conductivity of the crystal.

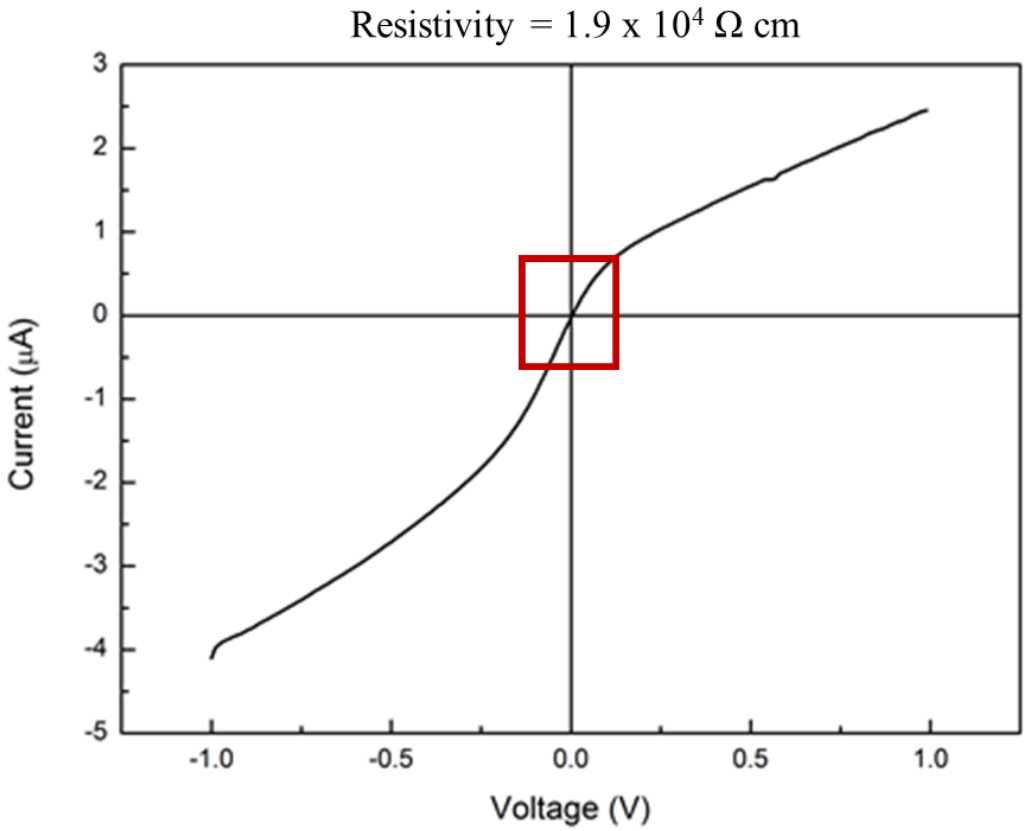

Figure 56. I-V plot and resistivity of sample MT13 RX2 W6.

An interesting observation about the calculations for this group of samples was the uniformity of the I-V measurements between the “guard ring grounded” case and “guard ring not grounded” case. For both type of measurements having the same resistivity results implies that the guard ring used in the design of the contacts is ineffective. But this is not an absolute statement since the number of probes were not enough to ground all the three pixels that are not measured during the data acquisition. One possible explanation for this observation might be the effect called “focusing field / defocusing field” [78]. For a CZT device to function as expected, it is important to have a desired electric field distribution inside the crystal. Having charges driven into wrong electrodes is an undesired effect causing charge losses. In CZT detectors having large aspect ratios (>1), like MT13 samples, variations in the electric field distribution can be present and non-uniform accumulation of space charge becomes possible. In a CZT sample which has a thickness less than 5 mm,

electric field lines tend to bend away from the side surfaces [78]. This is called as focusing effect by some researchers and it is usually expected when the potential on the side surfaces decreases slower than in the bulk. The opposite case is called defocusing effect. Figure 57 depicts illustrations of both.

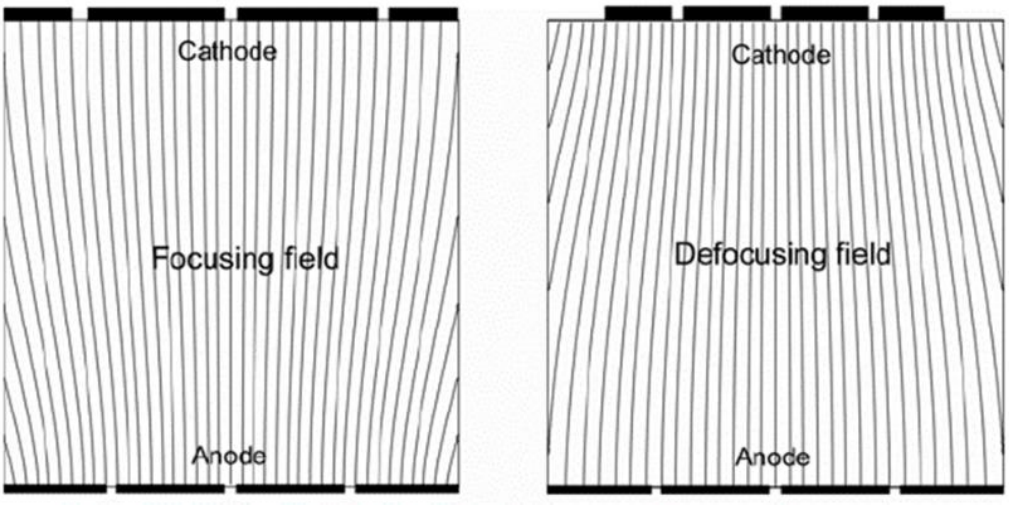

Figure 57. a) Focusing field, b) Defocusing field [78].

Another possible explanation can be found in Bolotnikov *et. al.* (2002). There it is found that grid structures surrounding each pixel yield better measurements in terms of leakage currents, hence better results in terms of uniform resistivity. The pixel design used in MT13 samples does not contain a grid like guard ring around each pixel but a general surrounding guard ring design was applied. In addition, the oxide layer that is inevitably formed in the interface region between the CZT surface and contact layer, affects the I-V characteristics considerably [79].

4.4.2 Current Voltage Measurements of MT20

The sample MT20 was doped during the growth by adding 10 ppm of indium with 7N purity level to the initial material loaded into crucible. Zinc concentration was again kept as 10% in weight. According to the studies reported in literature, indium doping increases resistivity and decreases leakage current considerably. The increase in the resistivity can be up to three orders of magnitude [79], [80]. It is a known fact

that by pinning the Fermi level near midgap, the resistivity of CdZnTe can be controlled by intrinsic and extrinsic dopants [16]. Due to the high partial pressure of the cadmium as opposed to tellurium, some of the cadmium atoms can escape from the bulk during the growth process of CdZnTe crystal, generating Cd vacancies ($[V_{Cd}]^{2-}$) in the as-grown crystal. It was confirmed that these Cd vacancies are shallow acceptors being responsible for the low resistivity of CdZnTe crystals [80]. When indium is doped into the crystal, indium atoms recombine with Cd vacancies present in the crystal lattice of CdZnTe. This recombination produces ionized donors of indium as shown in Equation 4.3 [49].

$$In + [V_{Cd}]^{2-} \leftrightarrow [In_{Cd}]^{+} + 3e^{-} \tag{4.3}$$

After indium doping, not all indium atoms go in for the Cd vacancy compensation. Some indium atoms remain as indium interstitials in the crystal lattice [49], [50].

A photo of the sample from MT20 ingot which is used for I-V measurements is shown in Figure 58. It is seen that there are different electrodes (pixels) having different areas. Among them, three small pixels were chosen to carry out I-V measurements.

The pixel areas in this design are 800 x 800 μm^2. I-V curves obtained from 3 different pixels are shown in Figure 59 and in Table 5 some of the resistivity values calculated from the I-V curves for three small pixels is given. Other measurements also gave similar resistivity values, except those conducted under light. The lowest resistivity value obtained in these measurements was 4.9 x 10^7 Ω cm.

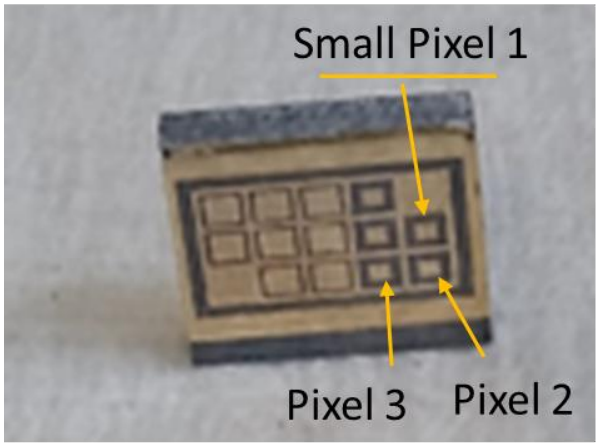

Figure 58. Pixel view of the sample MT20 RY1 W1.

There is an offset in the I-V plots shown in Figure 59. The curves should be passing through the origin but instead they shift to positive current values for zero voltage. The reason for this phenomenon is not clear. To understand it, further investigations are required.

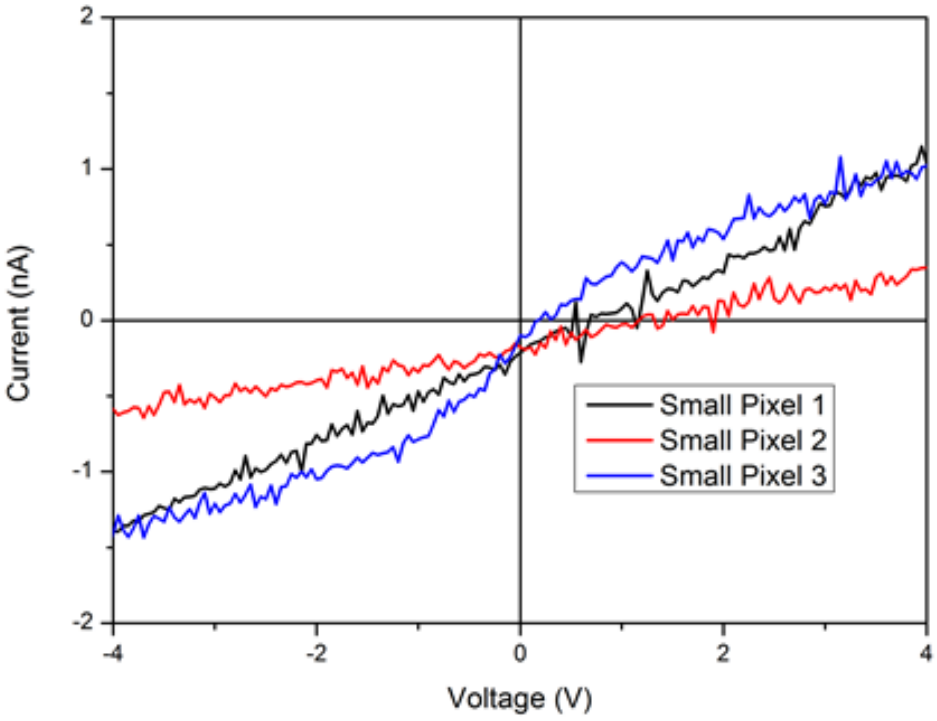

Figure 59. I-V plots of three small pixels from MT20 RY1 W1 sample.

Table 5. Resistivity values from MT20 RY1 W1.

Resistivity\Pixel Description	Small Pixel 1	Small Pixel 2	Small Pixel 3
Resistivity **(Ω cm)**	2.3×10^8	3.0×10^8	4.9×10^7

As can be seen from Table 5, different pixels give different resistivity values. The measurements were done while guard ring is grounded with one probe and each time one pixel is touched by the other probe and current through this one pixel touched by the probe and the cathode was tried to be measured. During this measurement, other three pixels are in the floating condition, since it was not possible to ground them with appropriate probes. It is believed that with more probes to ground the other floating pixels will give more accurate and more uniform resistivity values. The discussion given about focusing and defocusing fields inside the detector may also shed light on the variations observed in the resistivity values. The dimensions of MT20 RY1 W1 sample are rectangular and because of this, its aspect ratio is not better than MT13 samples, but worse. As a result, the electric field inside the sample is non-uniform and variations in resistivity measurements can be observed. Another possible explanation is the fact that the CZT detector, with metal contacts on two surfaces, resembles MSM (Metal-Semiconductor-Metal) structure with two back to back Schottky barriers on it. When biased, due to the ionization of deep levels, such a system can create space charge formations between anode and cathode sides. This phenomenon modifies the electric field distributions inside the detector and may cause significant variations locally [78]. But the most possible explanation for the different resistivity values can be the fact that the defects like tellurium inclusions and cadmium vacancies inside the crystals are not uniformly distributed. This causes non-uniform distribution of trapping centers and resulting with the non-uniform distribution of electric field inside the detector crystal. The noise in the I-V curves are due to the low current levels at nano amperes scale. It is believed that better cables and probes will decrease the noise and give smoother graphs.

4.4.3 Current Voltage Measurements of the Commercial Sample

The growth parameters of the commercial sample which was analyzed in this study were not known. Many research groups receive crystals from commercial vendors and conduct their own studies on them. For comparison, the same fabrication procedures were applied to these crystals. Figure 60 shows the commercial sample that is used.

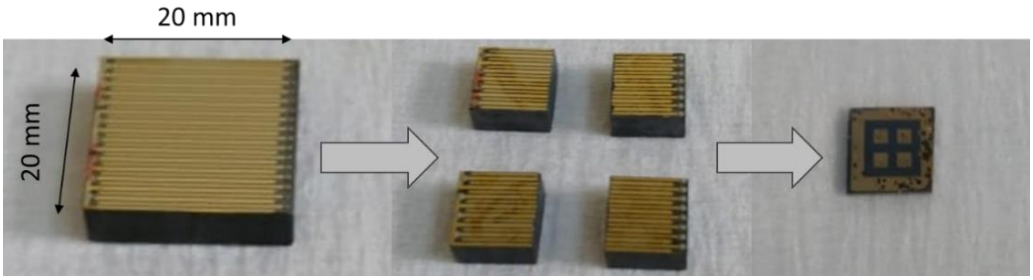

Figure 60. Commercial sample that has been cut into 4 equal pieces and the final product produced out of it.

In Figure 61 and Figure 62, the resistivity values are found to be in the order of 10^7 Ω cm for the commercial samples. It is clear that this value is below the expected values which are reported to be 10^8-10^{10} Ω cm range. The I-V curves are showing extremely well linearity indicating a good Ohmic contact with the electrodes fabricated in CGL. The reason for this improvement is not known. Considering the fact that we know very little about the details of this crystal, a further discussion about the electrical results is not useful. However, we have shown that the crystal grown at METU-CGL has outperformed the commercial sample in terms of the resistivity value. This is a very promising and encouraging progress in our research activities on the development of CdZnTe based radiation detectors.

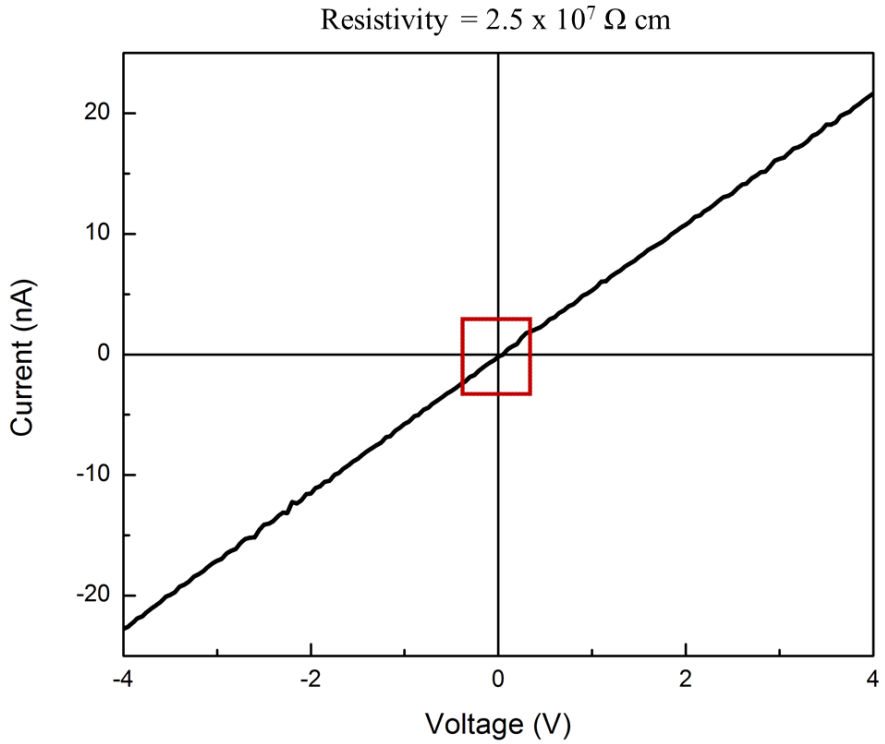

Figure 61. I-V plot of commercial sample 2.2.2 pixel 1.

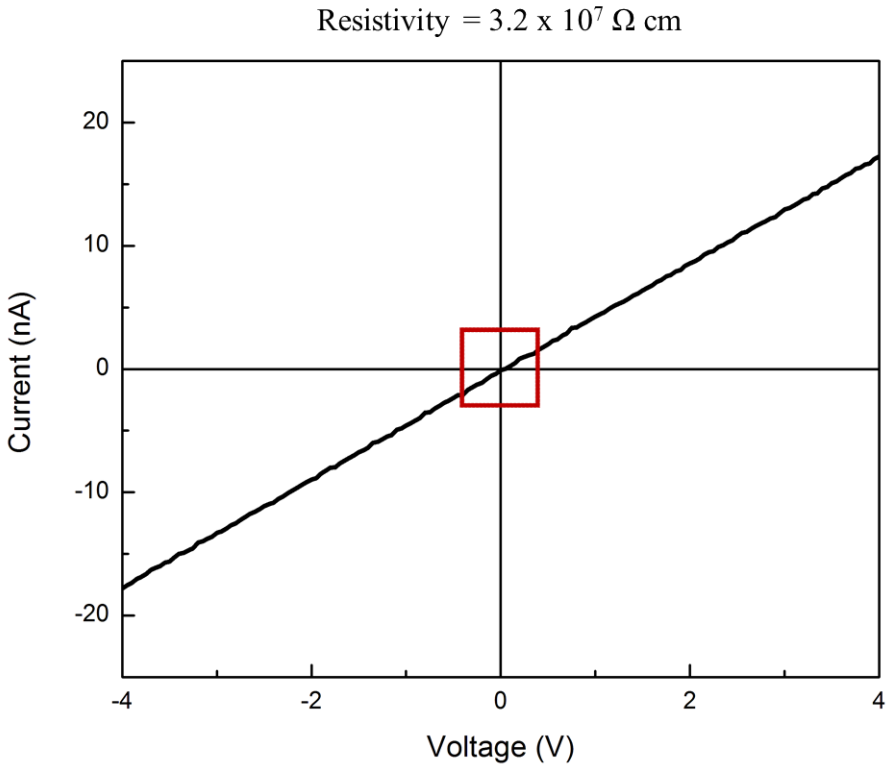

Figure 62. I-V plot of commercial sample 2.2.2 pixel 3.

CHAPTER 5

CONCLUSIONS

The goal of this thesis study was to develop CdZnTe radiation detector structure based on the crystals grown in METU Crystal Growth Laboratory (METU-CGL). This is the first study at METU in this direction. Previously, CdZnTe crystals have been grown at CGL by using Vertical Gradient Freeze technique for some other applications. Making a detector from this crystal is challenging due to the difficulties in controlling electronic properties of the crystal bulk as well as the interface between metal and the CdZnTe crystal. This study can be divided into four phases:

1. Crystal growth with and without doping.
2. Crystal mining from the ingot, cutting, lapping, polishing the crystal pieces for detector fabrication.
3. Surface preparation and metal contact formation.
4. I-V measurements and determination of resistivity values.

The process of crystal growth has already been optimized in the earlier studies. Ingots with very high single crystal grains can be grown at METU-CGL. The ingot named as MT13 was one of the good examples that has been grown previously. In this work, doping with indium has been achieved for the first time in CGL. Controlling the electrical resistivity of the samples with doping is crucial for a successful detector fabrication. We have shown that the resistivity of the crystal can be increased by four orders of magnitude with indium doping.

In the second step, single crystal grains were identified and extracted by a careful cutting process. Here, the yield should be maximized in order to get as many samples as possible from one ingot. The samples having different sizes were then lapped and polished to obtain a flat surface for the metal electrode deposition.

Following the polishing step, the crystal surface was etched with Bromine-Methanol solution and prepared for the metal deposition. From the literature it was understood that electroless deposition has better adhesion and better electrical contact to the crystal. Therefore, we employed electroless plating technique in all samples we analyzed in this study. In addition, electroless plating process for Au electrode formation has been developed and applied successfully for the first time in CGL. Metallization process has been further improved by optimizing the experimental conditions such as deposition temperature and time interval between process steps for minimizing the surface oxidation. All these process steps developed for the sample preparation have contributed to the accumulation of valuable knowledge and practical experience for the development of CdZnTe detectors in CGL. In this way, we have been able to improve the quality of metal contacts and the resistivity measurements.

In the final stage of this study, we measured I-V curves of the samples and calculated the resistivity from the slope of these I-V curves. Samples prepared from the undoped ingot (MT13) exhibited resistivity values in the range of 10^3-10^4 Ω cm, which is very low for a detector application. It is known that Cd vacancies in the crystal lattice result in higher conductivity. In order to increase the resistivity value, it should be doped with a dopant (typically indium) that can fill the Cd vacancies and thus increase the resistivity of it. Indium doping was then performed in the ingot named as MT20. Indium element with an amount of 10 ppm was added to the initial material before the growth. The amount to be added was decided from the limited amount of data published by other groups. Results were remarkably good. Resistivity values up to 3 x 10^8 Ω cm was obtained. These values are quite acceptable for detector fabrication. In order to evaluate the performance of our samples, we compared it with a sample manufactured by a well-known commercial

company. Metal electrodes with the same geometry were fabricated on this commercial sample by following exactly the same process steps. The resistivity of this sample was measured to be 3.2 x 10^7 Ω cm which is one order of magnitude lower than the resistivity value we obtained in our samples. This result is showing the successful fabrication and doping of CdZnTe crystal at METU-CGL.

However, the electrical performance of a CdZnTe crystal cannot be measured by

resistivity only. One needs to know the mobility-lifetime product which is directly related to the defect concentration in the bulk of the crystal. It is also necessary to perform I-V measurements at very high voltage values (up to 1000 V). Unfortunately, because of some device limitations, mobility-lifetime product and high voltage measurements were not done.

For future work, there are numerous things that can be conducted. Improving the method of contact deposition by optimizing the rate of deposition is crucial. In addition, to strengthen the contacts, trying other metals like nickel besides gold, can be done at the deposition level. Optimizing the bromine methanol etching process by investigating the etch rates of different concentration levels and time intervals will also contribute to the final goal of fabricating a radiation detector. In addition, the immediate thing to do next will be to measure mobility-lifetime products and perform high voltage I-V measurements.

REFERENCES

[1] T. Takahashi and S. Watanabe, "Recent progress in CdTe and CdZnTe detectors," *IEEE Trans. Nucl. Sci.*, vol. 48, no. 4 I, pp. 950–959, 2001.

[2] G. S. Camarda, A. E. Bolotnikov, Y. Cui, A. Hossain, K. T. Kohman, and R. B. James, "CdZnTe room-temperature semiconductor gamma-ray detector for national-security applications," *2007 IEEE Long Isl. Syst. Appl. Technol. Conf. LISAT*, pp. 107–114, 2007.

[3] K. Iniewski, "CZT detector technology for medical imaging," *J. Instrum.*, vol. 9, no. 11, 2014.

[4] G. F. Knoll, *Radiation Detection and Measurement*, 4th ed. Chichester United Kingdom: John Wiley and Sons Ltd, 2010.

[5] S. Del Sordo, L. Abbene, E. Caroli, P. Ubertini, A. M. Mancini, and A. Zappettini, "Progress in the Development of CdTe and CdZnTe Semiconductor Radiation Detectors for Astrophysical and Medical Applications," *Sensors*, no. 9, pp. 3491–3526, 2009.

[6] S. J. Bell, "Characterisation of Gold Contacts on CdZnTe Radiation Detectors," Surrey University, 2015.

[7] H. Y. Ergunt, "Bulk Growth and Characterization of Cadmium Zinc Telluride Crystals for Mercury Cadmium Telluride Infrared Detector Applications," Middle East Technical University, 2012.

[8] Ö. B. Balbaşı, "Vertical Gradient Freeze Growth and Temperature Modelling of Cadmium Zinc Telluride Crystals," Middle East Technical University, 2015.

[9] Ç. Doğru, "Investigation of Extended Defects in Cadmium Zinc Telluride Crystals Grown by Vertical Gradient Freeze (VGF) Technique," Middle East Technical University, 2015.

[10] M. P. Kabukcuoğlu, "Nanoscale Surface Finishing Studies and Characterizations of Cadmium Zinc Telluride Crystals," Middle East Technical University, 2016.

[11] Q. Zheng *et al.*, "Electroless deposition of Au, Pt, or Ru metallic layers on CdZnTe," *Thin Solid Films*, vol. 525, pp. 56–63, 2012.

[12] S. J. Bell *et al.*, “Performance comparison of small-pixel CdZnTe radiation detectors with gold contacts formed by sputter and electroless deposition,” *J. Instrum.*, vol. 12, no. 6, 2017.

[13] S. J. Bell *et al.*, “Comparison of the surfaces and interfaces formed for sputter and electroless deposited gold contacts on CdZnTe,” *Appl. Surf. Sci.*, vol. 427, pp. 1257–1270, 2018.

[14] Y. Q. Zhang and L. Fu, “Relationship between Deep Donors and Current-Voltage Properties in Au/CdZnTe/Au Device,” *Mater. Sci. Forum*, vol. 922, pp. 40–44, 2018.

[15] G. Lutz, *Semiconductor Radiation Detectors Device Physics*, 1st ed. Springer, 1999.

[16] T. E. Schlesinger *et al.*, “Cadmium zinc telluride and its use as a nuclear radiation detector material,” *Mater. Sci. Eng. R Reports*, vol. 32, no. 4–5, pp. 103–189, 2001.

[17] A. Beiser, *Concepts of Modern Physics*, 6th ed. McGraw Hill, 2003.

[18] I. Kuvvetli, “Development of CdZnTe detector systems for space applications,” Technical University of Denmark, 2003.

[19] S. N. Ahmed, *Physics and Engineering of Radiation Detection*. 2007.

[20] D. Griffiths, *Introduction to Elementary Particles*. Weinheim: Wiley-VCH, 2008.

[21] M. Uo, T. Wada, and T. Sugiyama, “Applications of X-ray fluorescence analysis (XRF) to dental and medical specimens,” *Jpn. Dent. Sci. Rev.*, vol. 51, no. 1, pp. 2–9, 2015.

[22] C. Szeles, “CdZnTe and CdTe materials for X-ray and gamma ray radiation detector applications,” *Phys. Status Solidi Basic Res.*, vol. 241, no. 3, pp. 783–790, 2004.

[23] G. Zavattini *et al.*, “Linearity discontinuities in xe-filled x-ray microstrip detectors,” *Nucl. Instruments Methods Phys. Res. Sect. A Accel. Spectrometers, Detect. Assoc. Equip.*, vol. 401, no. 2–3, pp. 206–216, 1997.

[24] R. Evans, *The Atomic Nucleus*. New Delhi: McGraw-Hill, 1955.

[25] “Student Radiographer, Interactions of X-ray Photons with Matter.” [Online]. Available: https://studentradiographer.com/?p=420. [Accessed: 15-Dec-2018].

[26] H. Y. Cho, J. H. Lee, Y. K. Kwon, J. Y. Moon, and C. S. Lee, “Measurement of the drift mobilities and the mobility-lifetime products of charge carriers in a CdZnTe crystal by using a transient pulse technique,” *J. Instrum.*, vol. 6, no. 1, 2011.

[27] T. Schlesinger and R. B. James, *Semiconductors for Room Temperature Nuclear Detector Applications*. Elsevier, 1995.

[28] J. E. Toney *et al.*, “Cadmium Zinc Telluride Charged Particle Nuclear Detectors,” 1997.

[29] “Sphalarite, mindat.org.” [Online]. Available: https://www.mindat.org/min-3727.html. [Accessed: 19-Dec-2018].

[30] R. Triboulet and P. Siffer, *CdTe and Related Compounds; Physics, Defects, Hetero-and Nano-structures, Crystal Growth, Surfaces and Applications*, 1st ed. Elsevier Science, 2009.

[31] P. Capper, *Properties of Narrow Gap Cadmium Based Compunds*. London, 1994.

[32] J. Crocco, “Crystal Growth & Technology , Device Fabrication , and Material Properties of Cd(Zn)Te for Radiation Detector Applications,” 2012.

[33] K. Guergouri, R. Triboulet, A. Tromson-Carli, and Y. Marfaing, “Solution Hardening and Dislocation Density Reduction in CdTe Crystals,” *J. Cryst. Growth*, vol. 86, pp. 61–65, 1988.

[34] Longxia Li *et al.*, “New Progress in Large-Size CZT (Zn=10%) Single Crystal Growth Using MVB Technique For Room Temperature Radiation Detectors,” *IEEE Symp. Conf. Rec. Nucl. Sci. 2004.*, vol. 4, no. C, pp. 2320–2323, 2004.

[35] R. T. Tung, “Recent advances in Schottky barrier concepts,” *Mater. Sci. Eng. R Reports*, vol. 35, no. 1–3, pp. 1–138, 2001.

[36] Y. Nemirovsky, A. Ruzin, G. Asa, Y. Gorelik, and L. Li, “Study of contacts to CdZnTe radiation detectors,” *J. Electron. Mater.*, vol. 26, no. 6, pp. 756–764, 1997.

[37] D. Pearman, “Electrical Characterisation and Modelling of Schottky Barrier Metal Source/drain MOSFETs,” 2007.

[38] D. R. Lide, *CRC Handbook of Chemistry and Physics*, 90th ed. Boca Raton: CRC Press, 2010.

[39] L. Li *et al.*, “Preparation of indium tin oxide contact to n-CdZnTe gamma-ray detector,” *Appl. Phys. Lett.*, vol. 112, no. 11, 2018.

[40] D. J. Olego, J. P. Faurie, S. Sivananthan, and P. M. Raccah, “Optoelectronic properties of Cd1-xZnxTe films grown by molecular beam epitaxy on GaAs substrates,” *Appl. Phys. Lett.*, vol. 47, no. 11, pp. 1172–1174, 1985.

[41] H. Chen, S. A. Awadalla, P. Marthandam, K. Iniewski, P. H. Lu, and G. Bindley, “CZT device with improved sensitivity for medical imaging and homeland security applications,” vol. 744902, no. September 2009, p. 744902, 2009.

[42] Q. Zheng, “Preparation and Development of CdTe and CdZnTe Detectors for Gamma Ray Radiation Applications PhD Dissertation,” Universidad Autonoma de Madrid, 2012.

[43] A. Zappettini *et al.*, “Growth and characterization of CZT crystals by the vertical bridgman method for X-ray detector applications,” *IEEE Trans. Nucl. Sci.*, vol. 58, no. 5 PART 2, pp. 2352–2356, 2011.

[44] P. W. Bridgman, “Certain Physical Properties of Single Crystals of Tungsten, Antimony, Bismuth, Tellurium, Cadmium, Zinc, and Tin,” *Proc. Am. Acad. Arts Sci.*, no. 60, p. 303, 1925.

[45] M. Schieber *et al.*, “Comparison of cadmium zinc telluride crystals grown by horizontal and vertical Bridgman and from the vapor phase,” *J. Cryst. Growth*, vol. 231, no. 1–2, pp. 235–241, 2001.

[46] U. N. Roy, A. Burger, and R. B. James, “Growth of CdZnTe crystals by the traveling heater method,” *J. Cryst. Growth*, vol. 379, pp. 57–62, 2013.

[47] B. Zhou *et al.*, “Growth and Characterization of Detector-Grade Cd0.9Zn0.1Te Crystals by the Traveling Heater Method with the Accelerated Crucible Rotation Technique,” *J. Electron. Mater.*, vol. 47, no. 2, pp. 1125–1130, 2018.

[48] Ö. B. Balbasi *et al.*, “CdZnTe bulk crystal growth and temperature modeling studies at METU-CGL,” *Hard X-Ray, Gamma-Ray, Neutron Detect. Phys. XX*, no. September, p. 29, 2018.

[49] Q. Li *et al.*, “Optical and electrical properties of indium-doped Cd0.9Zn0.1Te crystal,” *J. Cryst. Growth*, vol. 295, no. 2, pp. 124–128, 2006.

[50] G. Yang, W. Jie, Q. Li, T. Wang, G. Li, and H. Hua, “Effects of in doping on the properties of CdZnTe single crystals,” *J. Cryst. Growth*, vol. 283, no. 3–4, pp. 431–437, 2005.

[51] S. H. Park, Y. K. Kim, and H. S. Kim, “Influence of Surface Treatment of CdZnTe for.PDF,” pp. 1399–1401, 2005.

[52] S. Babar, P. J. Sellin, J. F. Watts, and M. A. Baker, “An XPS Study of Bromine in Methanol Etching and Hydrogen Peroxide Passivation Treatments for Cadmium Zinc Telluride Radiation Detectors S . Babar , P . J . Sellin , J . F . Watts , M . A . Baker Faculty of Engineering and Physical Sciences , University of,” 2013.

[53] M. E. Özsan *et al.*, “Chemical etching and surface oxidation studies of cadmium zinc telluride radiation detectors,” *Surf. Interface Anal.*, vol. 42, no. 6–7, pp. 795–798, 2010.

[54] Q. Zheng *et al.*, “Influence of surface preparation on CdZnTe nuclear radiation detectors,” *Appl. Surf. Sci.*, vol. 257, no. 20, pp. 8742–8746, 2011.

[55] H. Bensalah *et al.*, “The effect of etching time on the CdZnTe surface,” *Appl. Surf. Sci.*, vol. 257, no. 10, pp. 4633–4636, 2011.

[56] M. A. George *et al.*, “Study of electroless Au film deposition on ZnCdTe crystal surfaces,” *J. Appl. Phys.*, vol. 77, no. 7, pp. 3134–3137, 1995.

[57] I. M. Dharmadasa, “Recent developments and progress on electrical contacts to CdTe, CdS and ZnSe with special reference to barrier contacts to CdTe,” *Prog. Cryst. Growth Charact. Mater.*, vol. 36, no. 4, pp. 249–290, 1998.

[58] M. Ünal, D. Bender, Ö. B. Balbasi, M. P. Kabukcuoglu, Y. Ergunt, and R. Turan, “Optimization of chemical polishing by bromine-alcohol for detector-grade CdZnTe crystals and its effects on contacts Access Date: 13.11.2018,” 2018.

[59] “AZ 5214 E Image Reversal Photoresist Product Data Sheet” .

[60] “Photoresist of Photolithography.” [Online]. Available: http://www.wikizeroo.net/index.php?q=aHR0cHM6Ly9lbi53aWtpcGVkaWEub3JnL3dpa2kvUGhvdG9yZXNpc3Q. [Accessed: 12-Dec-2018].

[61] M. J. Madou, *Fundamentals of Microfabrication and Nanotechnology: Manufacturing Techniques for Microfabrication and Nanotechnology*. 2011.

[62] “AZ 5214 E Photoresist Technical Data Sheet” .

[63] Q. Zheng *et al.*, “Investigation of generation of defects due to metallization on CdZnTe detectors,” *J. Phys. D. Appl. Phys.*, vol. 45, no. 17, 2012.

[64] M. Roumié *et al.*, “Ion beam analysis of CdTe nuclear detector contact grown by electroless process,” *Nucl. Instruments Methods Phys. Res. Sect. B Beam Interact. with Mater. Atoms*, vol. 240, no. 1–2, pp. 386–390, 2005.

[65] M. Roumié *et al.*, "Depth profiling and stoichiometry of constituents in platinum electroless contacts on CdTe(111) under different pH values," *Thin Solid Films*, vol. 515, no. 20–21, pp. 7843–7846, 2007.

[66] "Aqua Regia Definition and Preparation, Science Notes," 2018. [Online]. Available: https://sciencenotes.org/aqua-regia-definition-and-preparation/. [Accessed: 13-Dec-2018].

[67] "What is Aqua Regia? How Does It Dissolve Gold? Science ABC," 2018. [Online]. Available: https://www.scienceabc.com/pure-sciences/aqua-regia-formula-recipe-structure-dissolve-gold-platinum.html. [Accessed: 13-Dec-2018].

[68] "Open Chemistry Database, Chloroauric Acid Tetrahydrate." [Online]. Available: https://pubchem.ncbi.nlm.nih.gov/compound/28133#section=Top Access. [Accessed: 13-Dec-2018].

[69] J. MacKenzie, F. J. Kumar, and H. Chen, "Advancements in THM-Grown CdZnTe for use as substrates for HgCdTe," *J. Electron. Mater.*, vol. 42, no. 11, pp. 3129–3132, 2013.

[70] T. Asahi, O. Oda, Y. Taniguchi, and A. Koyama, "Growth and characterization of 100 mm diameter CdZnTe single crystals by the vertical gradient freezing method," *J. Cryst. Growth*, vol. 161, no. 1–4, pp. 20–27, 1996.

[71] L. Zhang *et al.*, "Effects of Different Orientation on CdZnTe Detectors," 2006, vol. 62780909, no. 86022, pp. 1–3.

[72] JPK Instruments AG, "The NanoWizard AFM Handbook." Berlin, p. 40, 2005.

[73] "Geochemical Instrumentation and Analysis, Scanning Electron Microscopy." [Online]. Available: https://serc.carleton.edu/research_education/geochemsheets/techniques/SEM.html. [Accessed: 25-Dec-2018].

[74] Jeol Ltd, "Scanning Electron Microscope A to Z." Tokyo.

[75] R. M. Krishna, "Crystal Growth, Characterization and Fabrication of CDZNTE-Based Nuclear Detectors," 2013.

[76] V. Komar *et al.*, "Characterization of CdZnTe crystals grown by HPB method," *Nucl. Instruments Methods Phys. Res. Sect. A Accel. Spectrometers, Detect. Assoc. Equip.*, vol. 458, no. 1–2, pp. 113–122, 2001.

[77] V. Babentsov, J. Franc, A. Fauler, M. Fiederle, and R. B. James, “Distribution of zinc, resistivity, and photosensitivity in a vertical Bridgman grown Cd1-xZnxTe ingot,” *J. Cryst. Growth*, vol. 310, no. 15, pp. 3482–3487, 2008.

[78] A. E. Bolotnikov *et al.*, “Internal electric-field-lines distribution in CdZnTe detectors measured using X-ray mapping,” *IEEE Trans. Nucl. Sci.*, vol. 56, no. 3, pp. 791–794, 2009.

[79] A. E. Bolotnikov, C. M. H. Chen, W. R. Cook, F. A. Harrison, I. Kuvvetli, and S. M. Schindler, “Effects of bulk and surface conductivity on the performance of CdZnTe pixel detectors,” *IEEE Trans. Nucl. Sci.*, vol. 49 I, no. 4, pp. 1941–1949, 2002.

[80] M. Fiederle, A. Fauler, J. Konrath, V. Babentsov, J. Franc, and R. B. James, “Comparison of undoped and doped high resistivity CdTe and (Cd,Zn)Te detector crystals,” *IEEE Trans. Nucl. Sci.*, vol. 51, no. 4 I, pp. 1864–1868, 2004.